Helsinki University of Technology Doctoral Theses in Materials and Earth Sciences
Espoo 2010 TKK-ME-DIS-10

THERMALLY INDUCED ULTRA HIGH CYCLE FATIGUE OF COPPER ALLOYS OF THE HIGH GRADIENT ACCELERATING STRUCTURES

Doctoral Thesis

Samuli Heikkinen

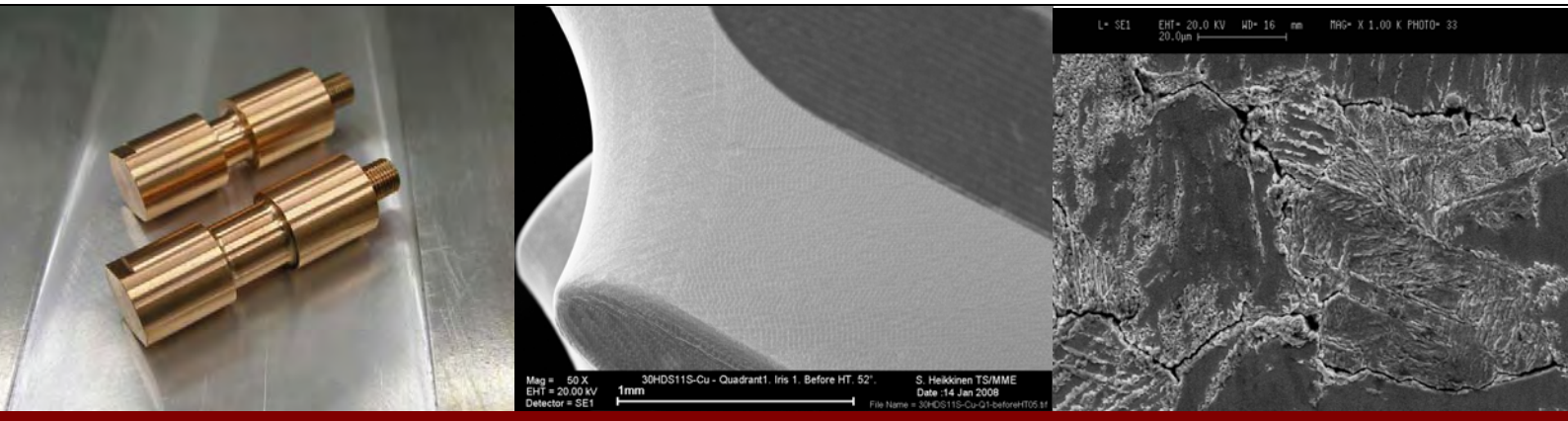

Aalto University
School of Science
and Technology

Helsinki University of Technology Doctoral Theses in Materials and Earth Sciences
Espoo 2010 TKK-ME-DIS-10

THERMALLY INDUCED ULTRA HIGH CYCLE FATIGUE OF COPPER ALLOYS OF THE HIGH GRADIENT ACCELERATING STRUCTURES

Doctoral Thesis

Samuli Heikkinen

Dissertation for the degree of Doctor of Science in Technology to be presented with due permission of the Faculty of Chemistry and Materials Sciences for public examination and debate in Auditorium V1 at Aalto University School of Science and Technology (Espoo, Finland) on the 5th of November, 2010, at 14.

Aalto University
School of Science and Technology
Faculty of Chemistry and Materials Sciences
Department of Materials Science and Engineering

Aalto-yliopisto
Teknillinen korkeakoulu
Kemian ja materiaalitieteiden tiedekunta
Materiaalitekniikan laitos

Distribution:
Aalto University
School of Science and Technology
Faculty of Chemistry and Materials Sciences
Department of Materials Science and Engineering
P.O.Box 16200
FIN-00076 Aalto
FINLAND
URL: (http://materials.tkk.fi)
Tel. +358-(0)9-47001
E-mail: Samuli.Heikkinen@f4e.europa.eu

ISBN 978-952-60-3345-7 (print)
ISBN 978-952-60-3346-4 (electronic)
ISSN 1795-0074 (print)
URL: http://lib.tkk.fi/Diss/

Picaset Oy
Helsinki 2010

Aalto University

ABSTRACT OF DOCTORAL DISSERTATION	AALTO UNIVERSITY SCHOOL OF SCIENCE AND TECHNOLOGY P.O. BOX 11000, FI-00076 AALTO http://www.aalto.fi

Author Samuli Tapio Heikkinen

Name of the dissertation

Thermally Induced Ultra High Cycle Fatigue of Copper Alloys of the High Gradient Accelerating Structures

Manuscript submitted 22.4.2008	Manuscript revised 23.11.2010
Date of the defence 5.11.2010	
☒ Monograph	☐ Article dissertation (summary + original articles)
Faculty	Faculty of Chemistry and Materials Sciences
Department	Department of Materials Science and Engineering
Field of research	Fatigue of materials
Opponent(s)	Prof. Petr Lukáš
Supervisor	Prof. Simo-Pekka Hannula
Instructor	Dr. Walter Wünsch

Abstract

In order to keep the overall length of the compact linear collider (CLIC), currently being studied at the European Organization for Nuclear Research (CERN), within reasonable limits, i.e. less than 50 km, an accelerating gradient above 100 MV/m is required. This imposes considerable demands on the materials of the accelerating structures. The internal surfaces of these core components of a linear accelerator are exposed to pulsed radio frequency (RF) currents resulting in cyclic thermal stresses expected to cause surface damage by fatigue. The designed lifetime of CLIC is 20 years, which results in a number of thermal stress cycles of the order of $2.33 \cdot 10^{10}$.

Since no fatigue data existed in the literature for CLIC parameter space, a set of three complementary experiments were initiated: ultra high cycle mechanical fatigue by ultrasound, low cycle fatigue by pulsed laser irradiation and low cycle thermal fatigue by high power microwaves, each test representing a subset of the original problem. High conductivity copper alloys in different temper states and several techniques to improve their fatigue life were investigated.

The results obtained by the three techniques are presented and the relations between them are determined. The RF fatigue experiments had conditions similar to the CLIC application, but the achievable number of cycles was limited. The data obtained by RF is extrapolated with the ultrasonic fatigue experiments which show a similar relative merit for the candidate alloys. Based on the results, a precipitation hardened copper zirconium alloy and an aluminum oxide dispersion strengthened copper alloy fulfill the CLIC requirements, the former being slightly better in terms of fatigue, but more sensitive to the temper state.

The ultra-high cycle ultrasound data showed surface roughening, which appeared at stress amplitudes lower than the fatigue strength. Different crack growth rates were observed between the precipitation strengthened and the dispersion hardened copper alloys. Compressive mean stresses were studied at ultra high number of cycles regime and they were not found to have an effect on fatigue performance under mechanical loading. Surface damage, due to RF induced fatigue, was observed to be anisotropic.

Keywords	ultra high cycle fatigue, high gradient, pulsed surface heating, fatigue of copper alloys		
ISBN (printed)	978-952-60-3345-7	ISSN (printed)	1795-0074
ISBN (pdf)	978-952-60-3346-4	ISSN (pdf)	
Language	English	Number of pages	104
Publisher	Department of Materials Science and Engineering		
Print distribution	Department of Materials Science and Engineering		
☒ The dissertation can be read at http://lib.tkk.fi/Diss/			

Aalto-yliopisto

VÄITÖSKIRJAN TIIVISTELMÄ	AALTO-YLIOPISTO TEKNILLINEN KORKEAKOULU PL 11000, 00076 AALTO http://www.aalto.fi

Tekijä Samuli Tapio Heikkinen

Väitöskirjan nimi

Thermally Induced Ultra High Cycle Fatigue of Copper Alloys in the High Gradient Accelerating Structures

Käsikirjoituksen päivämäärä 22.4.2008	Korjatun käsikirjoituksen päivämäärä 23.11.2010
Väitöstilaisuuden ajankohta 5.11.2010	
☒ Monografia	☐ Yhdistelmäväitöskirja (yhteenveto + erillisartikkelit)

Tiedekunta	Kemian ja materiaalitieteiden tiedekunta
Laitos	Materiaalitekniikan laitos
Tutkimusala	Materiaalien väsyminen
Vastaväittäjä(t)	Prof. Petr Lukáš
Työn valvoja	Prof. Simo-Pekka Hannula
Työn ohjaaja	FT Walter Wünsch

Tiivistelmä

Euroopan hiukkasfysiikan tutkimuslaitoksessa (CERN) kehitteillä olevan tulevaisuuden lineaarihiukkastörmäyttimen (CLIC) kokonaispituuden pitäminen alle 50 km mittaisena vaatii yli 100 MV/m kiihdyttävää gradienttia. Tämä asettaa huomattavia vaatimuksia kiihdytinelementtien materiaaleille, jotka ovat lineaaritörmäyttimen tärkein komponentti. Hiukkasia kiihdyttää pulssimainen radiotaajuusvirta (RF), joka aiheuttaa jaksollisia termisiä jännityksiä kiihdytinelementtien sisäpinnoille. Tämä jaksollinen kuormitus johtaa todennäköisesti materiaalin väsymiseen ja pintavaurioon. CLICin suunniteltu käyttöikä on 20 vuotta, jonka aikana termisten jännitysten kuormanvaihtoluku on yhteensä $2.33 \cdot 10^{10}$.

Kokeelliset tutkimukset aloitettiin, koska kirjallisuudessa ei ole CLICin parametrejä vastaavaa tietoa materiaalien väsymisestä. Suoritetut väsytyskokeet tehtiin ultraäänivärähtelijällä, pulssimaisella laserilla ja radiotaajuuslaitteistolla. Laitteistoilla tutkittiin hapettomia kupariseoksia eri tiloissa ja eri tavoin käsiteltyinä.

Kolmella koelaitteistolla saavutetut tulokset on esitetty yhdessä ja niiden yhteensopivuus on määritelty. RF koelaitteiston olosuhteet vastasivat CLIC sovellusta, mutta sillä ei päästy vaadittuihin kuormanvaihtolukuihin. RF tulokset on ekstrapoloitu ultraäänikoetulosten avulla, missä kuormanvaihtoluku on oikea ja eri materiaalit käyttäytyivät samankaltaisesti. Testitulosten perusteella erkautuslujitettu zirkoniumkupari ja alumiinioksidi dispersiolujitettu kupari soveltuvat parhaiten kiihdytinelementtien materiaaleiksi. Ensiksimainittu on niukasti parempi väsymisominaisuuksiensa puolesta, mutta menettää osan lujuuttaan korkeissa lämpötiloissa. Jälkimmäinen on vähemmän herkkä korkeille lämpötiloille.

Tulokset ultraäänilaitteistolla osoittivat ilmiön, jossa koekappaleiden pinnalle muodostui karheutta väsymislujuutta matalammilla jännitysamplitudeilla. Erityyppiset kupariseokset osoittivat eri särönkasvunopeuksia. Mekaaniset väsytyskokeet puristavalla keskijännityksellä osoittivat ettei suurilla kuormanvaihtoluvuilla väsymislujuudessa ole eroja verrattuna vaihtojännitykseen. RF väsytyskokeissa havaittiin anisotrooppista väsymistä eri raeorientaatioiden välillä.

Asiasanat	ultra high cycle fatigue, high gradient, pulsed surface heating, fatigue of copper alloys
ISBN (painettu) 978-952-60-3345-7	ISSN (painettu) 1795-0074
ISBN (pdf) 978-952-60-3346-4	ISSN (pdf)
Kieli englanti	Sivumäärä 104
Julkaisija	Materiaalitekniikan laitos
Painetun väitöskirjan jakelu	Materiaalitekniikan laitos
☒ Luettavissa verkossa osoitteessa http://lib.tkk.fi/Diss/	

Preface

The research work of this thesis has mainly been carried out at the European Organization for Nuclear Research in Switzerland (CERN) under the doctoral student programme. Part of the experiments were carried out at the Stanford Linear Accelerator Center in the USA (SLAC). I would like to thank my instructor Dr. Walter Wünsch who provided me with the opportunity to work on the interesting R&D project CLIC. Dr. Wünsch has not only given me valuable guidance and encouraged me during the work, but has also supported my ideas and given me responsibilities throughout the experimental study. As well, I wish to thank my supervisor, Professor Simo-Pekka Hannula from Aalto University, School of Science and Technology, Department of Materials Science and Engineering, for giving me helpful advice and with whom I have had useful discussions throughout this study. I also wish to give special thanks to my colleagues at SLAC, Professor Sami Tantawi, Dr. Valery Dolgashev and Dr. Lisa Laurent who hosted me during the experiments which were carried out at their Klystron Department.

I wish to thank the preliminary examiners, Professors Gary B. Marquis and Hannu Hänninen, for their efforts. I am very grateful to all of my CERN colleagues for the rich discussions and priceless help they provided in the course of the study, especially: Dr. Ian Wilson, Dr. Alexej Grudiev, Dr. Igor Syratchev, Miss Raquel Fandos, Mr. Markus Aicheler, Mr. Erminio Rugo, Mr. Franck Perret, Mr. Claude Achard, Dr. Thibaut Lefèvre, Dr. Steffen Döbert, Mr. Harri Hellgren, Mr. Keith Richardson, Mr. Peter Brown, Dr. Mauro Taborelli, Dr. Sergio Calatroni, Mr. Holger Neupert, Dr. Gonzalo Arnau Izquierdo, Dr. Stefano Sgobba, Mr. Ahmed Cherif, Mr. Didier Glaude and Mr. Dominique Pugnat. I would like to specially thank the external collaborators without whom the use of many of the technologies and materials would not have been possible: Dr. Roger Rupert from Uppsala University, Sweden, Mr. Kazuo Sugaya and Mr. Takashi Araki from Hitachi Cable Ltd., Japan, and companies: Luvata Oyj, Finland, Dr. Hielscher GmbH, Germany, Willy Flückiger SA, Switzerland, and VDL Enabling Technologies Group, Netherlands.

Last but not least I want to emphasize my gratefulness for my loving parents Sirkka-Liisa and Markku who have given me excellent guidance for life and of course, for my sweet wife Anu and lovely daughters Lisa and Sandra for understanding, being patient and just being there.

Barcelona, July 2010

Samuli Heikkinen

Author's contribution

The author of this thesis has been fully responsible of the ultrasonic fatigue experiments including the development of the apparatus, the operation of the experiments and the interpretation of the results. The pulsed laser (CERN) and pulsed RF (SLAC) experimental setups used in this study already existed and the experiments were operated by Holger Neupert, Sami Tantawi and Valery Dolgashev. Most of the Scanning Electron Microscope images (SEM) of the pulsed RF experiments has been produced by Lisa Laurent, SLAC. The laser and RF fatigue experiments described in the thesis as well as the interpretations of the results are the author's own. The text, ideas and conclusions written in this thesis are the author's own.

Contents

List of Abbreviations

3D	3-Dimensional
AC	Alternating Electric Current
AFM	Atomic Force Microscope
ANSYS	General-purpose finite element analysis software
ASM	American Society of Metals
BCC	Body Centered Cubic lattice
BPM	Beam Position Monitor
CAD	Computer Aided Design
CCD	Charge Coupled Device
CERN	European Organization for Nuclear Research
CLIC	Compact Linear Collider
CNC	Computer Numerical Control
Cu-OFE	Oxygen-Free Electronic Copper, C10100
CuZr	Copper Zirconium
EDM	Electrical Discharge Machining
EBSD	Electron Backscatter Diffraction
ESRF	European Synchrotron Radiation Facility, France
FCC	Face Centered Cubic, type of cubic crystal system
FE	Finite Element
FEA	Finite Element Analysis
FEM	Finite Element Method
GCF	Giga Cycle Fatigue
GlidCop®Al-15	Dispersion strengthened copper alloy
HCF	High Cycle Fatigue
HDS	Hybrid Damped Structure (Typically followed by a number, which indicates the number of cells)
HEP	High Energy Physics
HIP	Hot Isostatic Pressing
HSM	High Speed Milling
IACS	International Annealed Copper Standard for conductivity
ILC	International Linear Collider
IP	Interaction Point
ITER	Joint international research and development project that aims to demonstrate the scientific and technical feasibility of fusion power
LCF	Low Cycle Fatigue
LED	Light-Emitting Diode
LEP	Large Electron-Positron Collider
LHC	Large Hadron Collider
LINAC	Linear Accelerator

PETS	Power Extracting and Transfer Structures
PSB	Persistent Slip Band
RF	Radio Frequency
SB	Slip Band
SEM	Scanning Electron Microscope
SLAC	Stanford Linear Accelerator Center, California, USA
SN-curve	Stress vs. Number of Cycles to Failure Curve, Wöhler curve
UFGC	Ultra Fine Grained Copper
UHCF	Ultra-High Cycle Fatigue
UNS	Unified Numbering System for Metals and Alloys
UV	Ultraviolet
VHCF	Very-High Cycle Fatigue

List of Symbols

e^- *and* e^+	electron and positron
δ	skindepth
ω	angular frequency of the wave
κ	electrical conductivity of the material
μ_0	magnetic permeability of free space
R_s	surface resistivity
P_{peak}	peak power density (per area)
H_t *and* H	surface magnetic field
ΔT	maximum temperature rise
t_{pulse}	pulse length
ρ	density
c	specific heat
E_{acc}	accelerating surface electric field
N	number of cycles or number of cycles to failure
T_r	rise time of the RF pulse
T_f	filling time of the accelerating structure
T_p	flat top time of the RF pulse
P_0	peak input power of one accelerating structure
σ	stress
E	elastic modulus
α	thermal expansion coefficient
ν	Poisson's ratio
R	stress ratio
R_a	average roughness. The average height of the bumps on a surface, measured in micrometers
σ_{min} *and* σ_{max}	absolute minimum and maximum stress values
$\Delta\sigma_y$	yield strength
ρ_d	dislocation density
G	shear modulus
Q	quality factor

1 Introduction

1.1 High energy physics research

The progress of High Energy Physics (HEP) has required the use of the largest and most complex experimental facilities ever. Today, particle colliders are enormous projects whose design and construction phases can easily take several decades and whose total cost can reach billions of Euros. These projects have become international big-science collaborations, where countries from all over the world join in their efforts. The facilities are built one at a time thanks to this collaboration. The proposal for a new facility is made by the international high energy physics community. Their proposals are motivated by the latest experimental results and the newest theories of physics. The type, size, etc. of the new facility is thus ideally always driven by physics. Of course they have to take into account what is realistic in regards to existing or near-future technologies. Due to the large size and the ambitious targets regarding energy of the future facilities, their feasibility needs to be studied before the final decision is taken and while the previous facility is still operating. It is even better if there are several well studied options available when the course of physics will be decided.

The Large Hadron Collider (LHC) at CERN (European Organization for Particle Physics) is the current large scale physics facility and is expected to provide new physics results starting from 2010. The LHC has been built in the same tunnel as the previous collider, which was called the Large Electron-Positron Collider (LEP). Interest in the LHC began in the early 1980's and a feasibility study was initiated. It is worth mentioning that the LEP, the predecessor of LHC, ran from 1989 to 2000 which shows that the LEP was not even built yet when scientists were looking further into the future.

The design of the facility that will succeed to the LHC will be decided based on the results obtained with the LHC. Due to the size of the facility and especially the inevitable challenges which will have to be faced in order to obtain even higher energies, various feasibility studies of potential future facilities have already been initiated. The two most mature and advanced options are the Compact Linear Collider (CLIC) and the International Linear Collider (ILC). Among the leading physicists of the field, many believe that a TeV range electron-positron (e^- e^+) linear collider would be the most realistic option [1]. Out of these two, the ILC has a lower center-of-mass energy (0.5-1 TeV) and, arguably, could be built by using today's existing technologies [2]. CLIC is aiming for higher energies (3-5 TeV), but is also more challenging and its feasibility study still needs several years to demonstrate that it is technologically realistic.

1.2 CLIC study

The goal of the CLIC study is to provide the high energy physics community a possible future facility for the post-LHC era. The study has started at CERN around the mid-eighties based on the original ideas of Wolfgang Schnell [3]. Since the early days, the CLIC study group has enlarged and crossed the institutional borders as several members having common interests have joined the study. To this date, about 850 CLIC Notes [4] have been published and the study team is aiming to demonstrate the key feasibility issues of the CLIC technology by the end of 2010.

1.3 Basic features of CLIC

CLIC is based on a novel two beam accelerating scheme. A high intensity and low-energy electron drive beam runs in parallel with the main beam. The drive beam is decelerated and radio frequency (RF) power is generated in special Power Extraction and Transfer Structures (PETS). This RF power is then fed to the main beam accelerating structures, which accelerate the electron and positron beams that collide at the interaction point (IP). The two beam scheme is modular, allowing CLIC to be built in stages, starting from one module on each side of the IP and continuing by adding one module after the other throughout the tunnel. The modularity makes the complexes for the generation of all the beams and the power sources easier, because they can be located in the center of the facility, see Figure 1.1. The two linear accelerators (LINAC) and the beam transfer lines are housed in a single tunnel without any active RF system. This results in a simple configuration extendable to higher energies and which does not cause major modifications to the central facility.

The CLIC drive beam starts at the injector and is then accelerated by the drive beam accelerating structures, which operate at a frequency of 999.5 MHz. The frequency of the beam is then multiplied up to 12 GHz by a special complex consisting of delay loops and combiner rings. The current is simultaneously increased by a factor of 25. This beam is then driven in parallel to the main beam and decelerated by the PETS, where the 12 GHz RF power is extracted and fed to the accelerating structures. One PETS feeds two accelerating structures, see Figure 1.2. The main beam is generated in an injector and accelerated by special main linac accelerating structures, which are powered by the PETS. 79 % of the length of the main linac is filled with accelerating structures having a nominal accelerating gradient of 100 MV/m. The rest, is mainly taken up by quadrupole magnets and by component interconnections. With all the necessary beam delivery systems included, the overall length of CLIC at the nominal 3 TeV centre-of-mass energy is about 47.6 km. Up-to-date information on CLIC can be found on the CLIC Study [5] web pages.

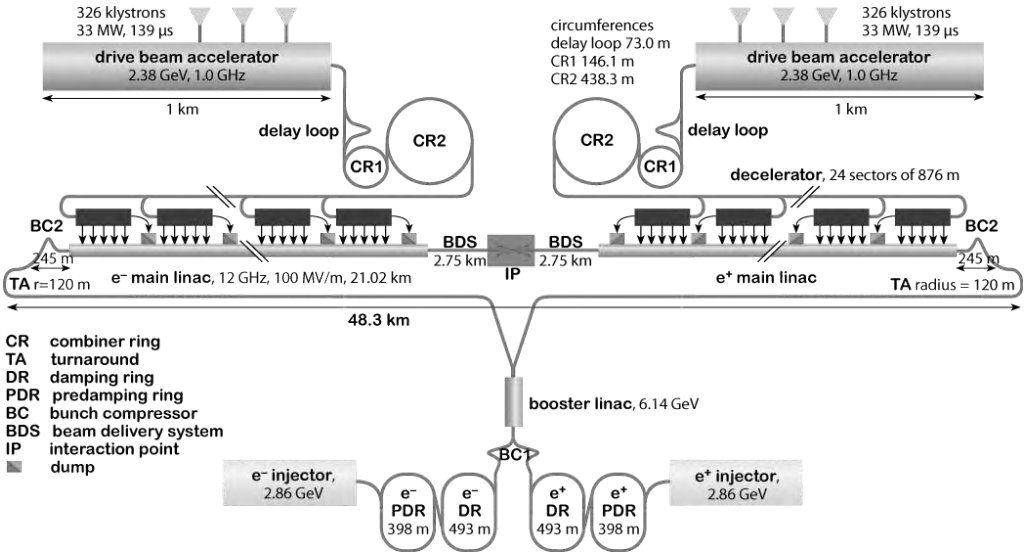

Figure 1.1: CLIC overall layout [5].

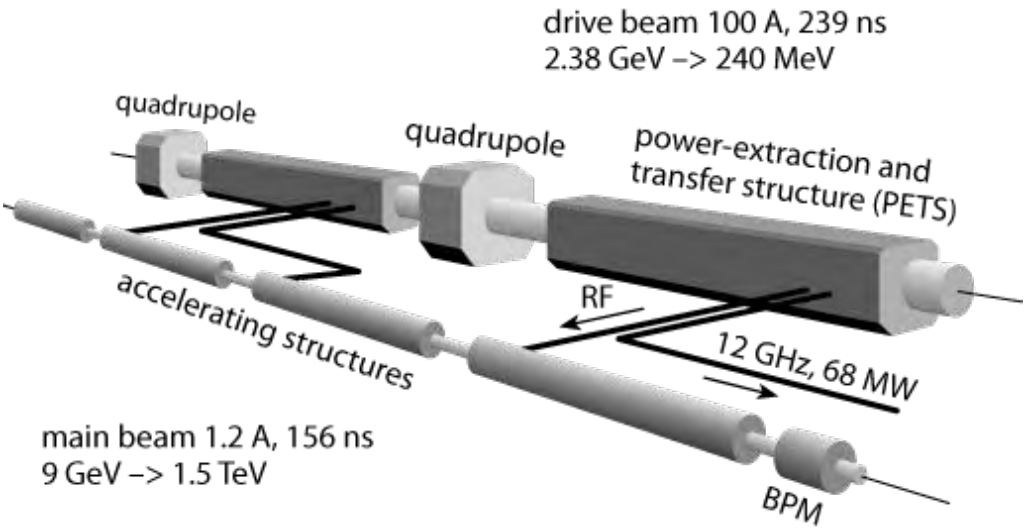

Figure 1.2: Layout of CLIC Module [5].

1.4 The CLIC main linac accelerating structures

The accelerating structures are the core components of the main linac. They provide the accelerating gradient for the particle beam with pulsed RF fields, fix the energy reach and their effect on transport dynamics of the beam has a major influence on

the efficiency and the luminosity of the collider. A number of design options are being studied in parallel. An example of a candidate design is the Hybrid Damped Structure (HDS) [6]. It is an optimum based on high power constraints and beam dynamics effects. A few parameters have evolved since the date of a Grudiev's publication. The nominal RF frequency was changed from 30 GHz to 12 GHz and the nominal accelerating gradient was changed from 150 MV/m to 100 MV/m, due to recent studies which indicated that they combined highest performance with lowest cost [7] [8]. The structure geometry and its key parameters are constant for all of the linac's length. There will be about 160,000 structures made from four main pieces, resulting in a total number of identical pieces of more than half a million.

The CLIC accelerating structure technology is normal conducting, so the operating temperature will be around room temperature (25-40 $°C$). The design of the structures is driven by the following requirements: an accelerating gradient of about 100 MV/m, power flow of 80-100 MW, 1-2 μm dimensional tolerances, an optical-quality surface finish and ultimately, a low mass production cost. The high gradient requires high electro-magnetic fields and power flows, which causes challenges for the materials. The high electric fields near the surfaces trigger RF-breakdowns, which are currently being studied in detail [9] [4], but which are beyond the scope of this study. The magnetic field near the surface induces a temperature rise of the material, which, due to its pulsed nature, does not have time to heat up the bulk uniformly and results into pulsed surface stresses, which is expected to cause a surface breakup by fatigue. This effect is the main subject of this thesis.

The RF-breakdown and fatigue put considerable demands on the materials of the structures. In general, accelerating structure materials must have as good as possible electrical and thermal conductivities. Traditionally, pure oxygen-free electronic copper C10100 (Cu-OFE) has been used for the accelerating cavities in most room-temperature accelerator applications. CLIC is however aiming at significantly higher gradients than previous applications and is running much closer to the fundamental limitations of pure copper. Therefore specific material studies have been initiated. In the main part of the structure - including the outer walls of the cavities - the fatigue loading was estimated and found to be above pure copper's fatigue strength [10]. Therefore, the use of high conductivity copper alloy which has superior fatigue strength than pure copper, was suggested.

The available options to improve the fatigue resistance of the accelerating structures depend on other aspects of accelerating structure development including the geometry optimization, the effect of the radio frequency breakdown and the whole fabrication process.

Currently accelerating structures prototypes are made either by diamond turning or high speed five axis CNC (computer numerical control) milling. This depends on the

concept of the test structure, which is either disc based (turning and re-machining of waveguides by milling) or quadrant based (milling).

Due to the need for ultra-high vacuum compatible connections which have good thermal and electrical conductances, vacuum brazing has been under use as an assembly method in different components of the particle accelerators. The method is particularly suitable for copper and stainless steel joints, which are two of the most used materials in particle accelerators. The thermal cycle lasts typically a few hours at about 800 - 1000 $°C$. The bond at this temperature range is made either quickly (Cu/stainless steel) or throughout few hours (Cu/Cu). This time is also needed in order to bring the piece to a uniform temperature which enables dimensional accuracy. The brazed bonds have good electrical and thermal conductances.

After the fabrication of the individual parts and then assembly there will still be many steps required before the startup of the particle accelerator. Often, the components of an accelerator machine which have an ultra high vacuum volume inside are baked out. This is done in order to remove water from the system. Typically, this implies a day or two at 150 - 300 $°C$.

Other types of possible preparations which are under study are various kinds of surface and thermal treatments which would enable to enhance the RF breakdown resistance of the accelerating structures. The origin of the breakdown is not yet fully understood, but there are some recent experimental evidences [11] which show that post-manufacturing heat treatments might increase the breakdown resistance and thus the high gradient performance of copper alloys.

1.5 The aims of the study

The aims of the study were:

1) To do a theoretical survey and an experimental investigation of high power RF induced ultra high cycle fatigue. The selected scope was to understand the fatigue, lifetime requirements of the CLIC accelerating structures, to study and identify the available candidate materials and their preparation techniques and to initiate and run an experimental program that addresses the CLIC parameter space which was not available in current literature.

2) To provide evidence to whether pure copper, a classical material for normal conducting accelerating structures, could meet the parameters of the CLIC accelerating structures and expose its limitations.

3) To address the fatigue performance of two different temper states of selected copper alloys, cold worked and annealed, because of two possible reasons. The manufacturing process or the high gradient requirements might lead to a high temperature cycle for the accelerating structures before the final installation. Thus, another aim was to provide a quantitative comparison for materials with and without temperature cycles.

4) To establish the damage criteria for the accelerating structures operated by pulsed radio frequency.

5) To propose a material and its possible preparation techniques for the accelerating structures which would fulfil the CLIC requirements.

1.6 Contribution of the research and the original features

It is believed that the best commercially available materials for the high gradient normal conducting accelerating structures which coincide with the CLIC's specific parameters have been identified and included in the experimental program.

Quantitative limits of the candidate alloys up to the UHCF regime have been defined with a reasonable precision. The results suggest that pure oxygen-free copper cannot fulfill the fatigue requirements of CLIC.

Depending on the technology option selected for the CLIC structures (quadrants, discs, vacuum brazing, etc.), a best candidate alloy for each case has been suggested. Obtained fatigue data for annealed material states is limited due to the constraints presented in experimental techniques. However, the existing data allows approximate comparisons between annealed and cold worked states.

The visible surface damage that was developed during fatigue did not decrease the performance of the RF cavity up to the number of cycles conducted, so the damage criterion was not defined.

The effect of compressive mean stress on fatigue strength of precipitation hardenable copper was studied up to UHCF regime.

The original feature of the research is the combination of three different experimental techniques, each addressing one subset of the original problem. Each technique has

an alternate failure mechanism and an alternate test condition. All the techniques were applied for selected materials. Alternating and fully compressive fatigue data of copper alloys was pushed up to UHCF regime, exceeding $7 \cdot 10^{10}$. The influence of compressive mean stress and the thresholds for surface roughening were studied up to this range.

2 Fatigue

2.1 Ultra High Cycle Fatigue of copper alloys

High cycle fatigue (HCF 10^6-10^8) and ultra high cycle fatigue (UHCF 10^8-10^{10}) have become more and more important in engineering of components as in several new industries the required design lifetime often exceeds 10^8 (car engine, high speed train) and even 10^9-10^{10} (gas turbine discs). This has led to increased research in the understanding of the failure mechanisms and development of new experimental techniques. UHCF studies on structural materials, like ferrous metals, have been carried out, but also non-ferrous metals, like copper and copper alloys have been vastly studied due to their high importance in electrical and high heat flux applications. In early studies of fatigue, when maximum lifetime of components was mostly around 10^6-10^7, the Wöhler curve [12] of metallic materials was assumed by having hyperbolic relationships, where the asymptote was horizontal. This created a concept of fatigue limit, a stress amplitude below which the material was assumed to have infinite lifetime. In reality, based on several studies, the asymptote at HCF and UHCF regimes is not really horizontal, especially for non-ferrous metals like copper. It is, thus, a safer and better solution to avoid extrapolations and assumptions on infinite fatigue life and perform fatigue experiments up to a relevant number of cycles regime. This of course is not always possible, especially in real conditions, but efforts have been made to achieve UHCF regime with certain high frequency testing methods.

In addition to the non-horizontal Wöhler curve, the high cycle fatigue prediction based on low cycle tests also have other risks. The favourable material properties can be different between different number of cycle regimes. The strengthening techniques to achieve a better fatigue resistance can also have different approaches for LCF and HCF regimes [13]. By increasing yield and tensile strengths one enhances usually the high cycle fatigue resistance but the ductility, which is important in the low cycle fatigue, is often reduced at the same time.

It has been agreed throughout various studies that the fatigue of copper alloys at HCF and UHCF regime, where the cyclic strain amplitude is small, mostly elastic, originates from the dislocation and persistent slip band (PSB) accumulation and strain localization in PSBs which interferes with the free surface and creates stress concentrations and thus initiates fatigue cracks. However, some studies suggest [14] that in alloyed materials containing non-metallic inclusions, like some copper alloys, the fatigue damage could also initiate from the inclusions inside the material.

The time of the fatigue crack initiation with respect to the time of the crack propagation becomes more and more important at large number of cycles and it is considered as a life-determining factor in the HCF and even more in the UHCF regime [15]. This means that most of the fatigue life is spent during the time before crack nucleation and that the actual crack propagation is only a small fraction of the total life. Two types of materials have been identified. Type I, ductile single phase metals, and type II, alloys containing non-metallic inclusions like high strength steels [14]. For both of them it is essential to focus on the crack initiation rather than only on the fracture mechanics. Fatigue failure at stress amplitudes lower than the conventional HCF fatigue limit of ductile face centered cubic (FCC) metals (type I) was observed at higher number of cycles, which confirms the non-existence of the classical fatigue limit. At stress amplitudes below PSB formation threshold, cyclic strain localisation in PSBs will not occur and it was proposed that surface fatigue cracks can occur even below the PSB formation threshold from the surface roughness developed by irreversible random slips in the matrix dislocation structure. For a mechanism of UHCF crack initiation it is proposed that some valleys, when a critical state of surface roughness is reached, act as stress raisers and that the local stress value exceeds the PSB threshold value. Cyclic strain gets further localized in formed PSBs and the PSB will extend deeper into the material. Finally, stage I fatigue cracks are initiated by propagating essentially to fatigue failure. However, the propagation is short, and the initiation life is considered as the major part of the fatigue life.

The life-controlling factor for type II materials experiences a transition from surface to internal failure when moving from low cycles to higher number of cycles. In addition, for the type II, the crack initiation has been confirmed as being the major factor of the fatigue life at HCF and UHCF regimes. It has not yet been proven which type of failure initiating from inclusions operates - cracking, debonding or slip bands originating from the inclusions. - It has been agreed that the internal cracks originate more easily from larger inclusions than smaller ones and that the closer the fatal inclusions are lying to the surface, the shorter the fatigue life is [16]. Higher number of inclusions increases the probability of a surface crack also at UHCF regimes. The fatigue failure is initiated by internal inclusions for type II materials if the number of inclusions is below a critical value. Above the critical value the probability of having inclusion interfering with the free-surface is higher and the crack tends to initiate at the surface.

Fatigue studies on pure aluminium [17] and pure copper (type I materials) have shown that at large strain amplitudes the cracks usually initiate from the grain boundaries. At small strain amplitudes and, thus, high number of cycles, the cracks usually initiate at persistent slip bands (PSB). The transition regime is typically of about 10^6 cycles. A large scatter of results around 10^6 is related to the competition between these two mechanisms of crack initiation. In addition, type II materials have a transition zone around which a larger scatter of results occur due to competition

between the two mechanisms.

For example, fatigue studies for the ITER's first wall and divertor structures showed that the damage mode for GlidCop® at large strain amplitudes was typically ductile. However, at small strain amplitudes it was brittle [18] and showed high crack growth rate. The selected material was a precipitation hardened alloy - copper chromium zirconium (C18150) [19] - which showed an optimum combination of fatigue strength and ductility. GlidCop® was rejected because of its brittleness. This HCF brittleness could be explained by the theory of type II materials because of its non-metallic inclusions. GlidCop® is a dispersion strengthened copper alloy which has nano meter size alumina particles dispersed in a copper matrix. Indicated type II materials could, thus, include also some copper alloys.

Tensile mean stresses are shown to be detrimental for fatigue strength with respect to zero mean stress conditions [20] [21]. Static straining history effects on fatigue of pure oxygen-free copper have been studied [22]. Cyclic hardening or softening were observed depending on the level of tensile prestraining. Materials with smaller prestrain and completely annealed materials resulted in cyclic strain hardening and vice versa. Fatigue experiments at large cyclic strain amplitudes showed slightly shorter fatigue life for tensile prestrains and the fatigue life decreased with increasing prestrain. The effect was more pronounced at smaller cyclic strain amplitudes and higher number of cycles (10^5 - 10^6). It was observed that the tensile pre-stress vanished almost completely prior to rupture. Tensile mean strains are generally accepted to support crack initiation and growth.

Compressive mean stresses are less studied on ductile metals and to this date, no UHCF experiments are known to exist. Dwell effects on high temperature fatigue (at 538 $°C$) were studied for precipitation hardenable C15000 (CuZr) [23]. It was shown that the material is tensile dwell sensitive, except at large strain levels (5 %). Tensile dwell sensitivity means that the tensile dwell caused detrimental effects on the fatigue life, in comparison to continuous cycling. Small strain amplitudes (1.4 %) created tensile mean stresses and decreased fatigue life. At large strain amplitude the tensile dwell increased the fatigue life, because of the fact that large tensile strain amplitudes created compressive residual stresses. There is, thus, an indication that compressive mean stresses compared to zero mean stresses do not decrease the fatigue life.

Studies around dwell effects on fatigue mechanisms [24] also showed that ductile fractures caused final failure on pure copper below 300 $°C$. Above that, other mechanisms such as oxidation and grain boundary migration occurred.

Room temperature creep-fatigue studies on CuCrZr and GlidCop® [25] showed that

tensile and compression hold times reduce fatigue life, in comparison to continuous cycling. The hold times were identical for compressive and tensile cycles. The effect was stronger for small strain amplitudes (higher number of cycles) and milder on large strain amplitudes. It was observed that crack modes were transgranular for both large strain amplitude cases, with and without hold time, and intergranular at small strain amplitudes, more prominently with hold times. It was suggested that creep during hold time facilitates the intergranular cracking, due to bulk hardening effects, and that the failure process may shift from the grain's interior to the grain boundaries. Stress relaxation during hold times was also observed. GlidCop® showed higher sensitivity on hold times than CuCrZr. For both materials, the peak tensile stress was reduced by 6-12 % during the hold time.

Various studies revealed surface roughening in HCF and UHCF regimes on pure copper. It sometimes has been detected as causing crack initiation, but it does not always lead to a final fracture. On ductile solids, this surface roughness can be described as microscopic hills and valleys where slip bands emerge at the free surface [26]. The roughening occurs during fatigue loading by the irreversibility of shear displacement along the slip bands.

Ultra high cycle fatigue is sometimes called 'giga cycle fatigue' (GCF) or 'very high cycle fatigue' (VHCF). For copper at UHCF regimes, a multi-stage fatigue diagram has been proposed [27]. There, the fatigue at low cycle regimes follows the Coffin-Manson law. The intermediate stage, from 10^6 to 10^8, corresponds to the fatigue limit on standard test bases, which is the minimum amplitude of plastic deformation per cycle at which the formation of stable slip bands is possible. In the gigacycle stage, the fatigue curve decreases again and saturates at the secondary fatigue limit, which is connected to the threshold plastic deformation amplitude at which the irreversible shear formation is virtually absent. At cyclic load ranges which go from 10^8 to 10^{10}, fatigue can lead to the formation of a quite developed local surface texture the genesis of fatigue microcracks, even without macroscopic crack propagation.

Small strain amplitude mechanical fatigue experiments up to $1.5 \cdot 10^{10}$ cycles [28] did not show a fatigue limit in the conventional sense. A surface roughening due to slip band development in the UHCF regime occurred way before and at significantly lower stress amplitudes than the final fracture. Quantitative strength values for UHCF of annealed pure copper were suggested, a fatigue strength of 92.2 MPa for copper at 10^{10} cycles and a threshold value for the surface roughening (persistent slip band formation threshold) of approximately 63 MPa at 10^{10} cycles [28]. These UHCF studies also showed two lifetime regimes, the HCF regime below 10^8 and the UHCF regime with a much shallower slope above 10^8.

The fracture initiation mechanisms in copper polycrystals were observed to be differ-

ent in UHCF and HCF regimes [29]. In HCF regimes, the most common mechanism originated from cyclic strain localization in persistent slip bands (PSBs) when the amplitude was higher than the PSB threshold, but in UHCF regime the failure could initiate at amplitudes well below the PSB threshold. The detected damage features were strain localization, surface roughening and stage I crack initiation. Also here, a significant fatigue induced surface roughening was observed below the PSB threshold. The severity of the surface roughness decreased proportionally to the local stress amplitude.

At UHCF regimes (small cyclic strain amplitudes), the first detectable stage of fatigue damage on polycrystalline copper was found to be the generation of SBs on the surface by strain localization [30]. During further cycling the SBs became PSBs and by continuing the cycling even further all grains were covered by them. Intrusions were formed with small stage I shear cracks, but they were not sufficient to initiate a longer fracture which could propagate further. The threshold of forming a fracture was found to be a factor of two higher than the threshold of forming PSBs (63 MPa). It was also discussed that higher frequency of cycling (19 kHz vs. $20Hz$) results in slightly higher PSB formation threshold (7-10 %) due to higher strain rate.

During recent years ultra fine grained (UFG) materials have grown interest due to their potentially high strength, especially at the UHFC regime. Studies on ultra fine grained (UFG) coppers at low-, high- and ultra high cycle fatigue regimes [31] showed systematically higher fatigue strength, particularly at the UHCF regime, than for conventionally grained copper. Testing frequencies varied from 10 Hz to 20 kHz and no difference in the obtained fatigue strengths were observed. It was also found that lower purity material (99.9 %) resulted in a significantly longer lifetime than higher purity materials ($>$ 99.96 %). This was explained by a higher structural stability of lower purity materials where the impurities contribute to the strength by pinning the mobility of grain boundaries and dislocations. Unlike for higher purities, grain coarsening and cyclic softening was not observed for lower purities. Alloyed UFG coppers, like CuCrZr [13], have shown also significantly higher fatigue strengths than their conventionally grained counterparts. The finely dispersed alloying elements in the matrix resulted in similar behavior than for lower purity UFG coppers.

UFG coppers also showed higher crack growth rates than conventionally grained coppers [32]. A clear change in the crack path morphology was observed below and above 10^8 cycles. Below the crack follows a straight path and above it follows a torturous path. Also, the surface topography was modified above 10^8. A significant surface roughness appeared as a result of accumulation of SBs and intrusions and extrusions.

High cycle fatigue (HCF) studies of high purity (99.99 %) UFG copper [33] showed

that already at the early stage of cycling by a stress amplitude of 240 MPa PSB-like shear bands (SB) appeared on the surface. The orientation of these features seemed to depend on the orientation of the grain. After the development of the SB protrusions with various orientations came out adjacent to it. Further cycling did not grow the SBs and protrusions in size, but their number on the surface was increased until saturation. Lower stress amplitude (120 MPa) resulted in longer protrusions, which were parallel to each other. Otherwise, their behavior during further cycling was similar to higher stress amplitudes.

Generally, the ultra fine grained coppers show significantly higher strengths than conventional grained coppers, but they still remain less studied materials. Moreover, they are not yet commercially available and established industrially. In the laboratory the size of fabricated samples has been relatively small. Nevertheless, the UHCF properties of UFG coppers have been studied. Although the strength has been shown higher, the UFG coppers show many similar fatigue mechanisms than conventionally grained coppers at UHCF regime.

Surface evolution characterizations during fatigue loading have shown anisotropies in fatigue damage on conventionally grained polycrystalline copper [34]. At applied number of cycles of $6.9 \cdot 10^3$ and $7.59 \cdot 10^4$, different levels of damages were observed between adjacent grains. This anisotropy was suggested being due to favorable and unfavorable slip orientations. It was also observed that cracks were usually formed at the boundaries between grains, one with considerable surface damage and another with much less visible deformation. It has been suggested [26] that for copper, the cracks may nucleate preferably at grain boundaries if the grain boundaries separate highly misoriented grains.

2.2 Thermal fatigue

Thermal fatigue investigations began in the early 1950 due to continually increasing operating temperatures and everlasting need for greater reliability. Thermal fatigue is the definition of a complex phenomena appearing in materials or structures of different materials joined together and exposed to cyclic thermal loads causing cyclic thermal gradients which induce stresses due to non-uniform thermal expansion. Thermal fatigue is a gradual degradation and eventual break of a material by alternated heating and cooling processes with partial or total constraint of the thermal expansion [35]. When thermal cycles are coupled with external mechanical loads, the phenomena is called thermo-mechanical fatigue, although sometimes these two are mixed in the literature. Thermal and mechanical fatigue have both the same source of damage, cyclic stresses, but are due to different origins: The former from temperature transient, which imposes self-induced stresses in order to guaran-

tee the continuity of the structure, and the latter from external loads. The induced cyclic thermal stresses can be caused by different mechanisms. The local expansion can be hindered by the surrounding material and the expansion of a component can be limited by adjacent components. The former case can still be divided into two different types. The thermal gradient can be caused by short heat flux pulse, which does not have enough time to warm the component uniformly, and, thus, causes a thermal stress. Other cases can occur in anisotropic or bi-metallic structures, where the thermal stress or gradient can be due to different thermal expansion coefficients or a conductivity mismatch between adjacent grains. Thermal stress evaluation differs from mechanical stress evaluation. As it was said above the thermal stresses arise from the structure itself due to thermal cycles. They cannot often be directly calculated, but are typically based on an analysis which has another calculation as an input, the thermal calculation. Therefore, thermal stresses and fatigue are often characterized with more uncertainty than the mechanical stresses and fatigue.

The thermal stresses in thermal fatigue investigations, like in [36], [37] and [38], can be defined by the thermal stress equation for the local expansion which can be hindered by the surrounding material, it is thus believed to give a reasonably good estimate of the stresses in plane stress conditions [39]:

$$\sigma = \frac{E \cdot \alpha \cdot \Delta T}{1 - \nu} \tag{2.1}$$

where

σ = stress
E = elastic modulus
α = thermal expansion coefficient
ν = Poisson's ratio
ΔT = maximum temperature rise

Thermal fatigue experiments on ceramic materials have shown a similar relationship between the thermal and mechanical stresses [37]. Cyclic thermal stresses having short pulse length induced thermal gradients in the specimen and the samples were cracked when the thermal stress exceeded the material's strength.

Most of the processes that have been explained for mechanical fatigue also take place during thermal fatigue as long as the temperature stays below half the melting point of the material. For temperatures higher than the half of the one at melting point, processes like creep become dominating. Also, the lifetimes are found to decrease

faster - with respect to corresponding strain amplitude in mechanical fatigue - with increasing temperature. On the other hand, on thermal fatigue studies, a phenomena of crack arrest or dormant cracks has been observed [35]. Induced thermal stresses, especially if the pulse length is short and the infected depth is small, the nucleated cracks propagate to the zero stress zone and can be stopped there. The cracks, thus, do not propagate further but only increase in number as the number of cycles increases.

In thermal fatigue the most important parameter is the temperature difference during the cycle. In addition, if the mean temperature is high the properties of the material change significantly. For instance, its strength often decreases when the temperature increases. Holding time is another important parameter of the thermal fatigue. Long times spent at the high maximum temperatures enhances the creep and recovery effects of the material.

Generally, the known thermal fatigue investigations have been concentrated on the low cycle fatigue studies. Not until recently there have been few high cycle studies. In the low cycle studies the transient temperature differences are typically of the of order several hundreds of degrees K. The induced thermal stress for such a temperature difference is well in the plastic regime of the material. The number of cycle ranges concerned go typically from 10^2 to 10^5. The pulse length of the thermal cycle often lasts several minutes. Therefore, creep considerations play an important role [40]. It has been suggested that low cycle thermal fatigue is always somewhere between creep and mechanical fatigue [40]. It has been postulated [41] that the approaches to thermal fatigue problems, where the representative isothermal fatigue resistance is assumed at the maximum temperature of the thermal cycling, do not give conservative estimates of thermal fatigue life, although it was earlier believed to be so.

Thermal fatigue does not have a standard testing procedure [41]. Because there are so many variables associated with thermal cycles it is impossible to define a single representative cycle. The test results serve mainly as a way of ranking the relative thermal fatigue strength of different materials for a given application.

A thermal and mechanical fatigue study on copper conducted for the printed circuit board industry [42] showed strong lifetime dependence on frequency and amplitude of the thermal cycles. The frequency was varied from 100 Hz to 10 kHz and the oscillations had a sinusoidal shape. The strain rate of the constant amplitude cycles was, thus, higher for higher frequencies. Thermal fatigue experiments on thin copper films showed isolated microstructural modifications. Anisotropic fatigue damage was related to crystallographic orientations. The grains having a crystallographic orientation (111) showed damage at earlier stages than the grains having a crystallographic orientation (100). By extrapolating, a damage threshold was suggested as

ΔT of 100 K after $3 \cdot 10^9$ cycles at 200 Hz. The pulse length used was of 5 ms. The sample materials used were thin films of sputtered copper, which have generally shown higher fatigue strength than bulk materials [42]. However, a comparison between bulk copper thermal and mechanical fatigue [43] [44] data was done where failures occurred at the same stress amplitudes and number of cycles. Also, the general mechanical and thermal fatigue behaviors of thin film and bulk copper were found to be similar.

For thermal fatigue resistance, the strength of the material is not the only parameter of interest. Physical properties like high thermal conductivity, low thermal expansion coefficient and low specific heat are also crucial parameters. The thermal fatigue studies [45] [46] [19] have often resulted in the selection of materials among the high conductivity, high strength, copper alloys.

3 Numerical analyses of the CLIC fatigue problem

The highest accelerating gradient at which the CLIC structures can operate is limited in part by fatigue. In principle, the total energy of a linear collider could be increased up to the required levels just by increasing its length. But in reality, there are constraints for the length. These have led to an estimation for the realistic maximum total length to be of the order of 50 km. Within 50 km of total length and length taken by the final focus system, quadrupole magnets etc., a 3 TeV machine would require an accelerating gradient of about 100 MV/m.

To accelerate particle beams, pulsed RF waves are guided into the accelerating structures. The cavity geometry of the structure makes waves at the design frequency travel in synchronism with the beam. The bunches of particle beams have a spacing equal to an integral multiple of the RF wavelength so that they can arrive in the structure with the same phase which causes the beam to get accelerated by the RF. The part of the RF pulse energy whish has not been transferred into the beam is coupled out from the structure and is absorbed by a special RF load. The RF load is made of a material which absorbs electromagnetic energy and converts it into heat which is then transferred into cooling water outside the system.

When an oscillating RF electro-magnetic wave interacts with conductive material, mobile electrons within the material oscillate back and forth with the same frequency, and thus create an alternating electric current (AC) near the surface. This surface current encounters the electric resistance of the material and when there is an electric current through an object whish has a resistance, some of the electrical energy is converted into heat. The resistance depends on the electrical conductivity of the material and its skin depth, which corresponds to the distance of how deep these currents flow. The surface resistance can be calculated as [47],

$$R_s = \frac{1}{\delta \cdot \kappa} \tag{3.1}$$

where

R_s = surface resistance
δ = skindepth
κ = electrical conductivity of the material

For a good conductor, the skindepth can be calculated with the formula [48],

$$\delta = \sqrt{\frac{2}{\omega \cdot \kappa \cdot \mu_0}} \tag{3.2}$$

where

ω = angular frequency of the wave
μ_0 = magnetic permeability of free space

For cavities made of Copper Zirconium C15000 and working at a frequency of 11.944 GHz, the equation (3.2) gives us a skindepth of 0.63 μm.

Based on the current accelerating structure design, the peak input of RF power for one structure is of about 65 MW. The structures are operated in a pulsed mode with a typical RF pulse length of a few hundred nanoseconds at a repetition rate of 50 Hz. The peak power density (per unit surface area) depends on the field distribution inside the structure. The relation between the surface magnetic field [47] and the temperature rise [49] in a rectangular RF pulse can be calculated with the two following two equations:

$$P_{peak} = \frac{1}{2} \cdot R_s \cdot H_t^2 \tag{3.3}$$

$$\Delta T = \frac{2 \cdot P_{peak}}{\kappa} \cdot \sqrt{\frac{\kappa \cdot t_{pulse}}{\pi \cdot \rho \cdot c}} \tag{3.4}$$

where

P_{peak} = peak power density (per area)
H_t = surface magnetic field
ΔT = maximum temperature rise
t_{pulse} = pulselength
ρ = density
c = specific heat

In June 2007, the pulsed surface temperature rise in the CLIC parameters list was limited to 56 $°C$ and the resulting RF pulse had the shape shown in Figure 3.1. The parameters for the pulse in Figure 3.1 are shown in Table 3.1. Keeping ΔT constant and using a representative flat top value of 270 ns for the pulse length, the equations from (3.1) to (3.4) give a magnitude of $4.79 \cdot 10^5$ A/m for the surface magnetic field (H_t).

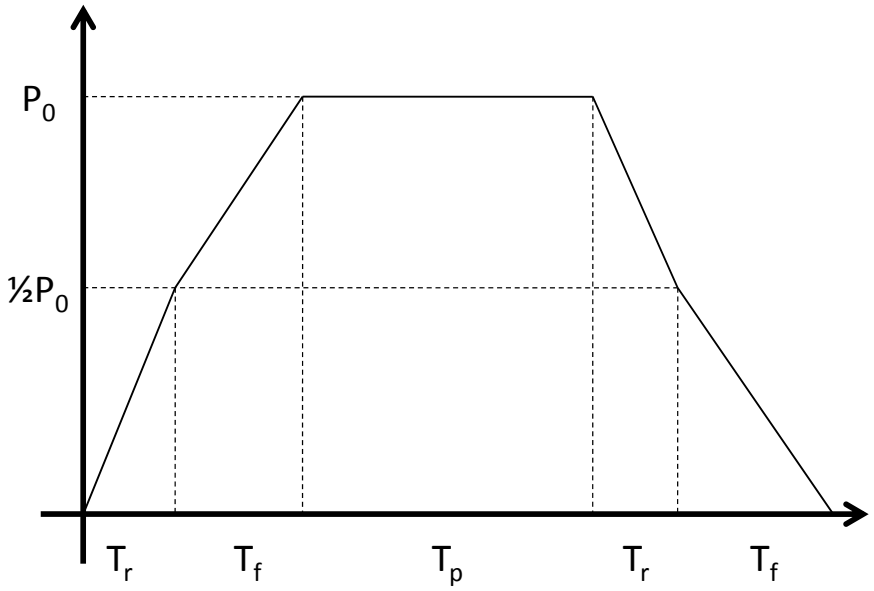

Figure 3.1: CLIC RF pulse profile (June 2007 parameters). See the parameters in Table 3.1.

Table 3.1: CLIC RF pulse parameters [50].

T_r	rise time	30.3 ns
T_f	filling time	59.8 ns
T_p	flat top time	207 ns
P_0	peak input power of one structure	65 MW

The surface temperature rise was also calculated using the Finite Element Analysis (FEA) software ANSYS. In these calculations the temperature dependent material properties and correct pulse shape, as in Figure 3.1, were taken into account.

Figure 3.2 represents the simulated surface heating cycle during the RF pulse. The maximum value of ΔT occurs just after the flat top part of the pulse. The value

is very close to the one calculated by the analytical formula, indicating that the temperature dependent properties do not significantly affect the situation within this temperature range.

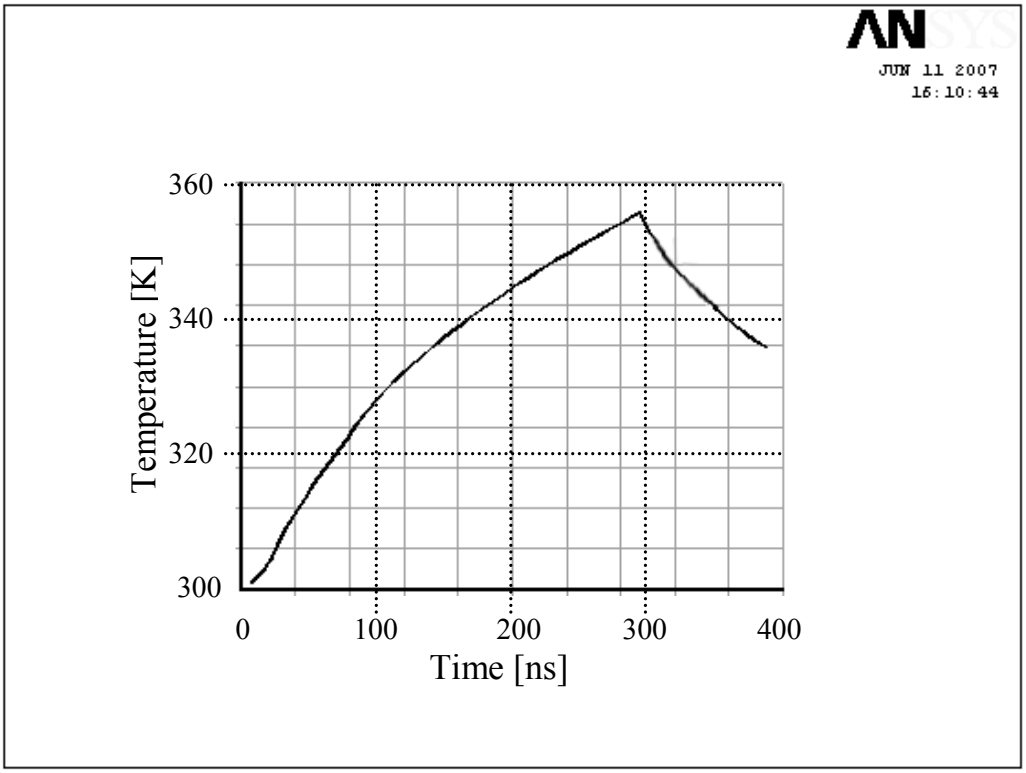

Figure 3.2: Simulated surface temperature versus time in the cavities during the RF pulse of Figure 3.1.

The induced heat is conducted into the bulk during the idle time between the RF pulses. This idle time is of about 20 ms. The cooling of the surface was also simulated by ANSYS and the result is shown in Figure 3.3. One accelerating structure will generate approximately 55 W of average heat load, which has to be transferred out. The structures will be water cooled and it can be seen that the cyclic temperature decreases close to initial value after 300 ns, Figure 3.3. The average temperature rise due to cycling after saturation is of about 1.5 K [51], so the thermal loading can be considered to have a fully cyclic nature.

Figure 3.4 shows the temperature profile from the surface into the bulk at the point of maximum ΔT. The depth affected by the temperature gradient is of about 18 μm.

The thermal cycles result in repeated thermal gradients which, due to a non-uniform

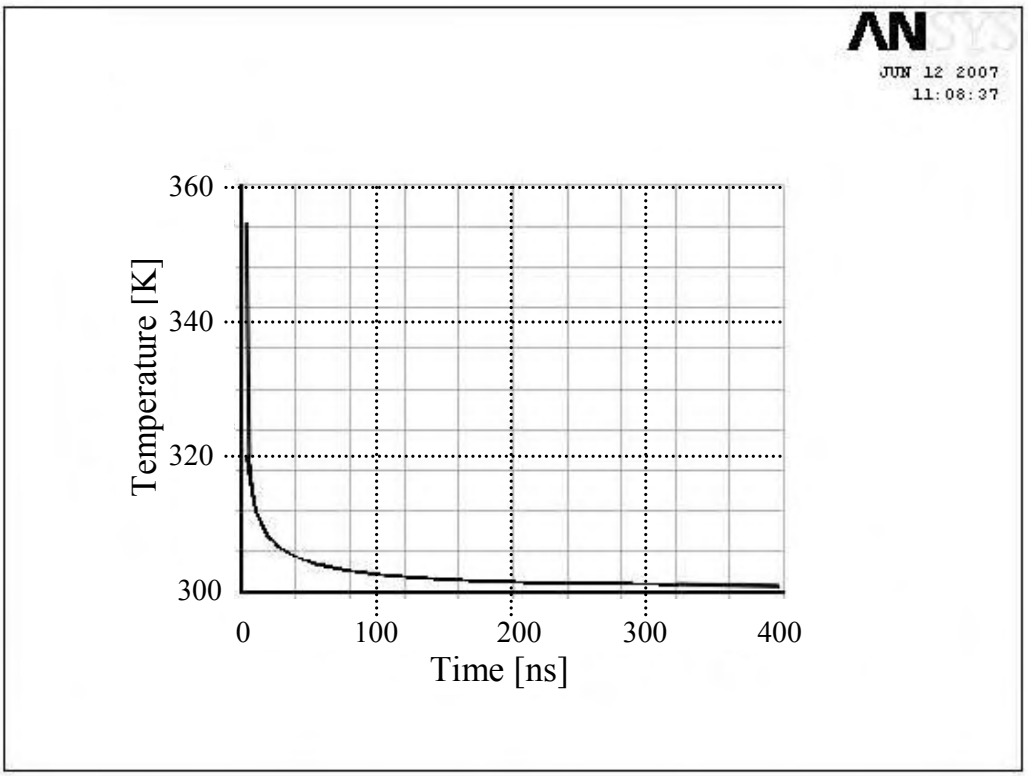

Figure 3.3: Simulated surface temperature versus time in the cavities during the idle time between the RF pulses.

thermal expansion, result in cyclic compressive stresses. Equation (2.1) gives -160 MPa for Copper Zirconium C15000 (UNS C15000, Unified Numbering System for Metals and Alloys). The stress is compressive, resulting in a negative value of stress. This value corresponds to the peak to peak stress, so the condition of the loading can also be expressed as a stress amplitude of 80 MPa with a mean stress of -80 MPa. Later in the text this distinction will be used.

The stress level was calculated by an ANSYS coupled field thermo-structural analysis. There, the results of the above mentioned thermal analyses were used as an input for a structural analysis. The maximum equivalent Von Mises Stress profile from the surface into the bulk is shown in Figure 3.5. The compressive stress is due to the non-uniform temperature distribution, where the expansion is hindered due to the small heated depth compared to the dimensions of the piece. It can be seen that the 160 MPa peak to peak stress is similar to the value obtained with the analytical calculations.

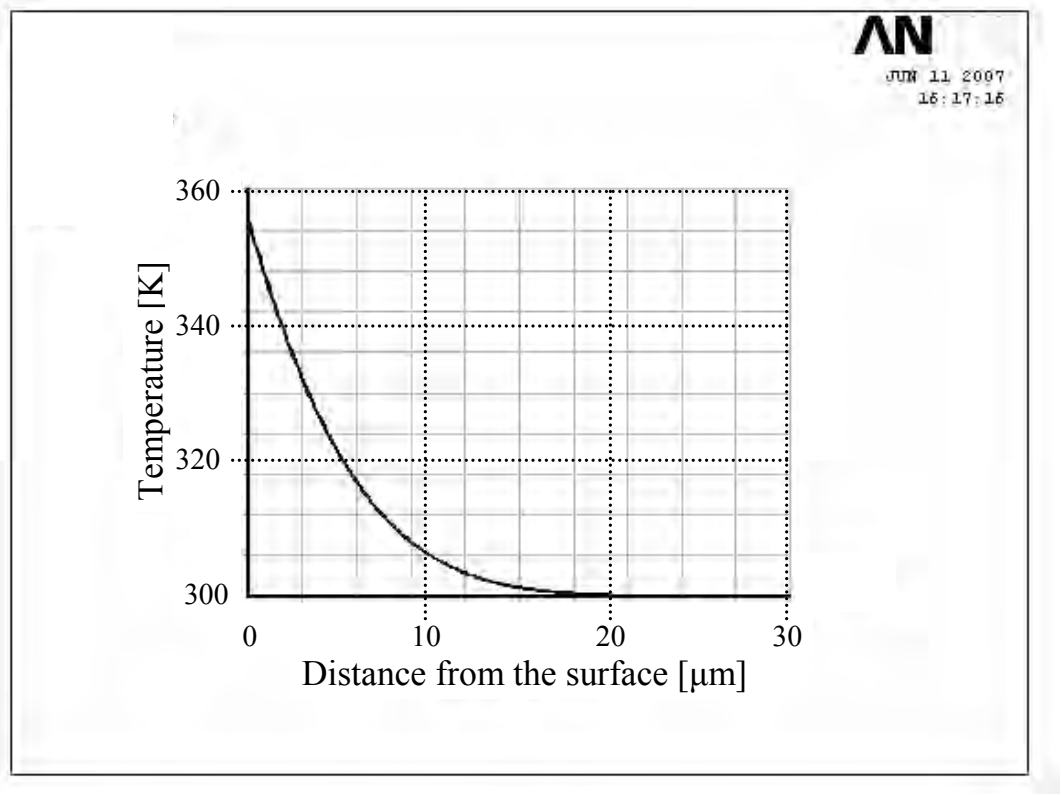

Figure 3.4: Simulated temperature profile from the surface of the cavity into the bulk at the moment of maximum temperature difference.

Figure 3.6 shows a 3D CAD (Three Dimensional Computer Aided Design) model of the CLIC prototype structure. The highlighted maximum magnetic field region has the highest pulsed temperature rise and the thermal stress. Figure 3.7 shows an example of the simulated field distribution in an HDS-type prototype cavity. The figure illustrates the complexity of 3D geometry, which has been applied in order to reduce the peak field values.

In addition to the stress amplitude, the other main parameter for fatigue is the number of cycles. The number of thermal stress cycles (N) during the estimated 20 *year* lifetime of CLIC is shown in Table 3.2.

The fatigue loading encountered in CLIC is fully compressive (thermally induced) repeated stress with $2.33 \cdot 10^{10}$ *cycles*. A schematic presentation of the fatigue loading is shown in Figure 3.8 with a stress amplitude of 80 MPa and a mean stress of -80 MPa.

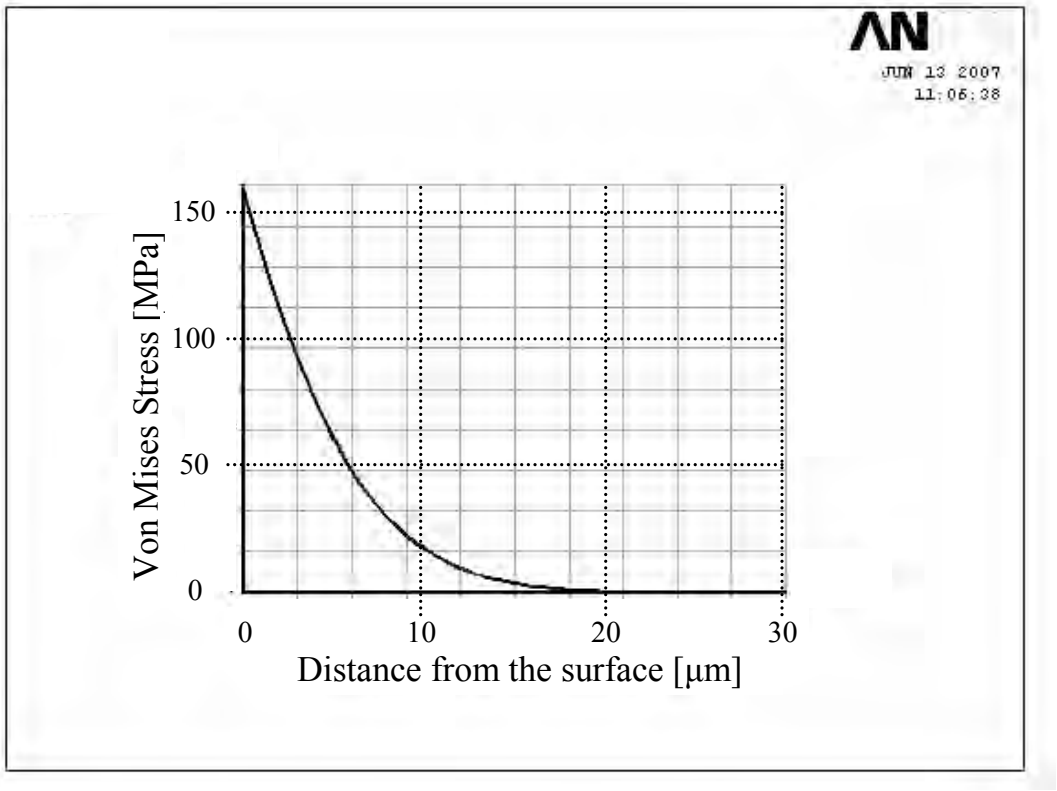

Figure 3.5: Simulated equivalent Von Mises Stress profile from the surface of the cavity into the bulk at the moment of maximum temperature difference.

Table 3.2: Estimated number of cycles in the CLIC lifetime.

Years	20
Months/Year	9
Days/Month	30
Hours/Day	24
Repetition rate	50 Hz
Total N	$2.33 \cdot 10^{10}$

The fatigue damage criteria of the CLIC accelerating structures differs from classical mechanical engineering components where a macroscopic fracture is usually used. RF cavities have currents flowing in a skin depth under surfaces.

A small crack or increased surface roughness, having a size of the same order of magnitude as the skindepth, is expected to disturb the surface current flows of the

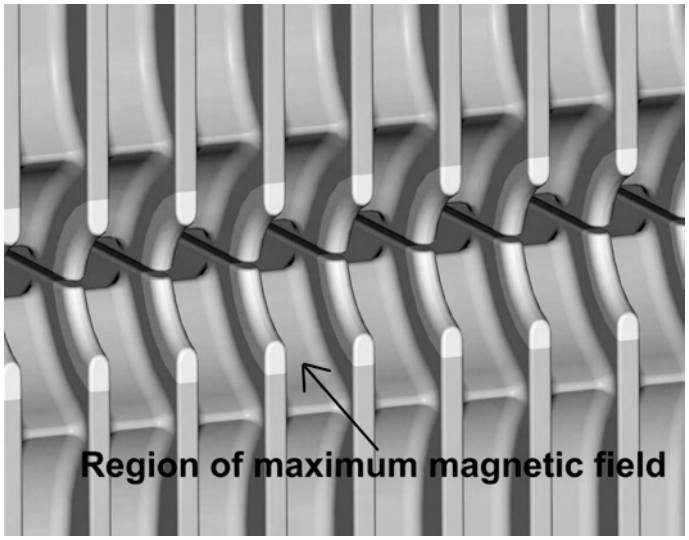

Figure 3.6: 3D CAD model of the HDS-type CLIC prototype structure. The region of maximum magnetic field is in the outer wall of the cavities.

RF cavities [48]. Surface flaws increase the electrical resistance and thus increase the pulsed temperature rise and the stress amplitude. On the contrary the small cracks and surface damage can cause stress relaxation. Consequently, it is not clear whether the damage by pulsed RF loading has an amplification mechanism. Due to the complexity of this effect the criteria of damage for the RF cavities will be defined qualitatively by RF fatigue experiments.

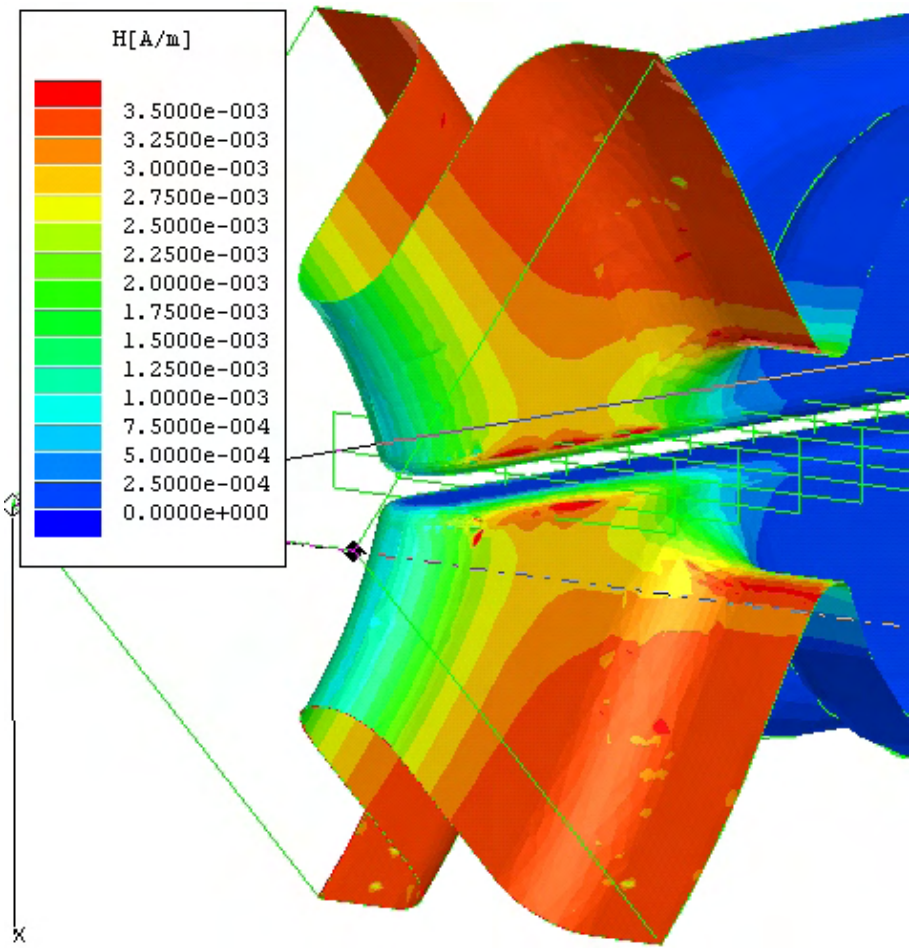

Figure 3.7: Magnetic field distribution on the cell walls of an HDS CLIC prototype structure [52]. The magnetic field distribution in the figure (H $[A/m]$) is given for 1 MV/m accelerating gradient. For fixed geometry, the magnetic field is proportional to the gradient, so for 100 MV/m H needs to be multiplied by 100.

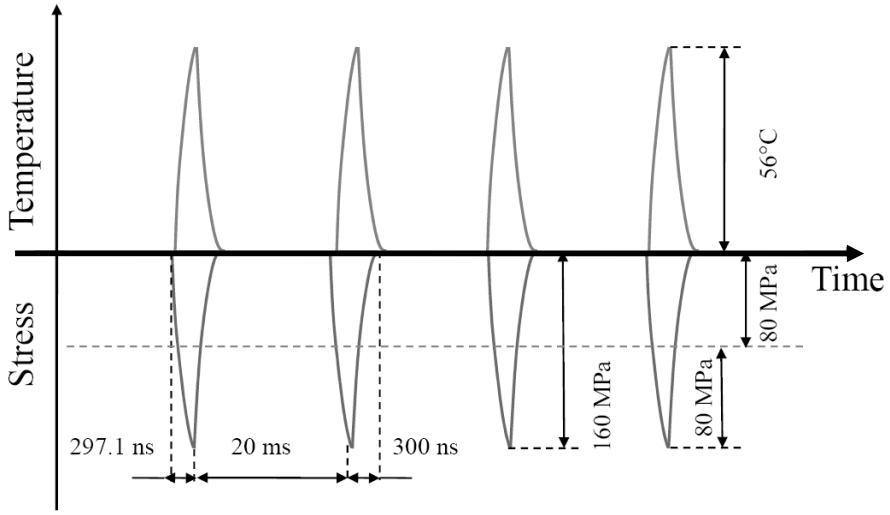

Figure 3.8: Schematic of fatigue loading in the accelerating structures. The temperature is the top curve and the stress curve is at the bottom. (Not in scale)

4 Undertaken fatigue experiments

A comprehensive experimental program for fatigue has been set up in the context of the CLIC study. The aims are: (i) to provide insight into fatigue effects in the CLIC range, (ii) to establish a relation to classical fatigue studies and (iii) to provide data for a range of materials to be used in the CLIC optimization. Ideally, all the experiments would be carried out with a radio frequency fatigue experimental setup. However, the number of cycles range of CLIC (Table 3.2) is above what is reachable by available RF sources in a reasonable time.

Two experiments were established to increase the number of tests and cycles; pulsed laser and ultrasonic fatigue experiments. Eventually, the RF fatigue experiments were made as well and few targeted runs were carried out for the most interesting materials in states which were deduced from the other experiments.

In summary, the ultrasonic fatigue experiments were performed to study the ultra high cycle fatigue behavior, the pulsed laser fatigue experiments to study the thermal fatigue effects at low cycle range with the correct time structure and the RF fatigue experiments to study the RF induced fatigue as well as benchmark the two others.

4.1 Ultrasonic fatigue experiments

An ultrasonic fatigue experimental setup was used to study the UHCF behavior of different alloys. Currently, the ultrasonic method is the only one that can reach the UHCF regime within a reasonable testing time. The technique was developed and introduced originally by Mason in 1950 [53]. Since then there have been numerous evolutionary versions of such a setup reported by various authors. The authors have always developed their own setups, which differ more or less from one another, although the basic concepts have been similar. Up to this date there is no standard technique for ultrasonic fatigue testing.

The ultrasonic setup is based on an ultrasonic generator and transducer, as shown in Figure 4.1. The generator transforms the low frequency of wall plug electric energy to higher ultrasonic frequencies, typically from 5 kHz to 25 kHz. The device converts this high frequency electric energy into mechanical motion (vibration) by a piezoelectric transducer. To operate correctly, all the vibrating components attached to the piezoelectric transducer have to have the same resonant frequency for longitudinal oscillation. Under operation the system produces a longitudinal

standing wave. The small amplitude of vibration of the piezoelectric transducer is amplified first by special booster geometry, which is typically built in the ultrasonic devices. The principle of the booster simply is that the longitudinally vibrating volume's cross section is varied. The last basic part of the ultrasonic device is an exchangeable tip called the sonotrode. Typically, the same amplifying method as the one in the booster is used for the sonotrode. In Figure 4.1, an example of amplitude magnification of US systems is presented.

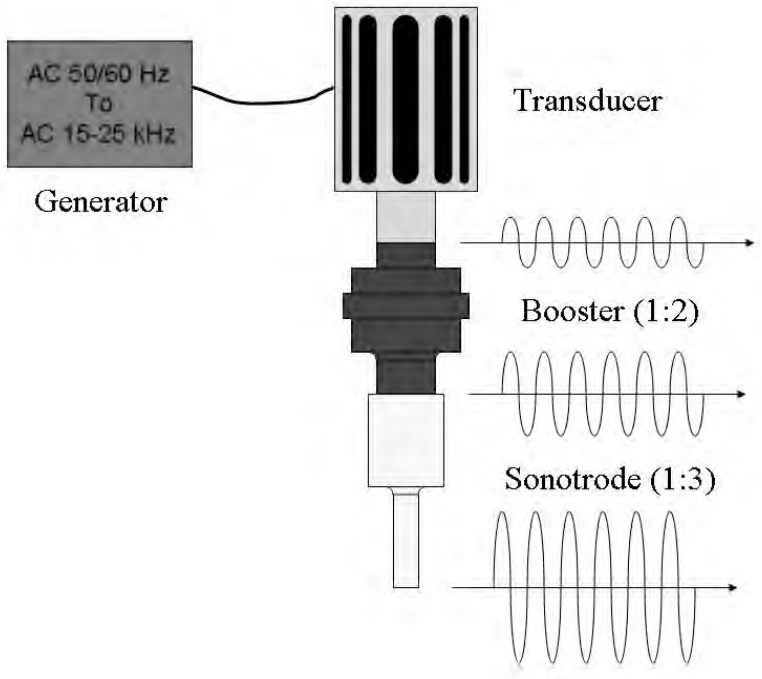

Figure 4.1: The basic components of the ultrasonic system and an example of the amplitude magnification where the initial amplitude of the transducer is multiplied by a factor of 6 by the booster and the sonotrode.

4.2 Details of the ultrasonic experimental setup

In the CLIC fatigue study the ultrasonic method was introduced and commissioned by Alexander Menshov [54], although no calibrated experiments at CLIC parameter space were done. The two devices selected were 250 W ultrasonic processors, of type UIP250, by Hielscher GmbH, Germany.

In the ultrasonic fatigue experimental system used here, the sonotrode represents the material sample. The mounting of the sonotrode to the booster was made by

a screw connection. Such a solution is possible when the junction of the two parts is in the node point of the standing wave where the strain is zero. In this case the forces on the screw connection were relatively low and no failures were observed.

Figure 4.2: Diamond turned sonotrodes for ultrasonic fatigue experiments.

The UIP250 device is originally designed for industrial use, mainly for smaller scale liquid treatment applications. In this study it was also found to be very reliable for laboratory fatigue experimental use. The device has a control unit which ensures a constant set amplitude of vibration which worked without any problems even during the longest conducted run of $7 \cdot 10^{10}$ cycles which took approximately one month of non-stop operation. The device has a built-in system to lock the resonant frequency of the sonotrode in the range of $24 \pm 1\ kHz$. This feature gives some flexibility in the sonotrode design, because the sonotrode does not have to match the nominal frequency with an excessively tight tolerance. The relative amplitude of vibration can be adjusted from 20 % to 100 %. The absolute value of the displacement amplitude depends on the sonotrode's volume, density and geometry.

The technique used to measure the stress amplitudes in the samples (sonotrodes) in ultrasonic fatigue experiments varies between different authors. In this study an optical method was used to measure the amplitude of the oscillation of the tip of the sonotrode. From this the stress level was calculated. The system is based on a LED (Light-Emitting Diode) and a light sensor. The sonotrode tip is placed between the two. The moving tip changes the total light falling on the sensor which gives an output signal. This signal is analyzed by an oscilloscope. A mechanically vibrating object produces an AC (Alternating Current) signal on the scope where the voltage amplitude is proportional to the mechanical displacement amplitude of the object. The voltage is calibrated against displacement by moving the sonotrode by a known

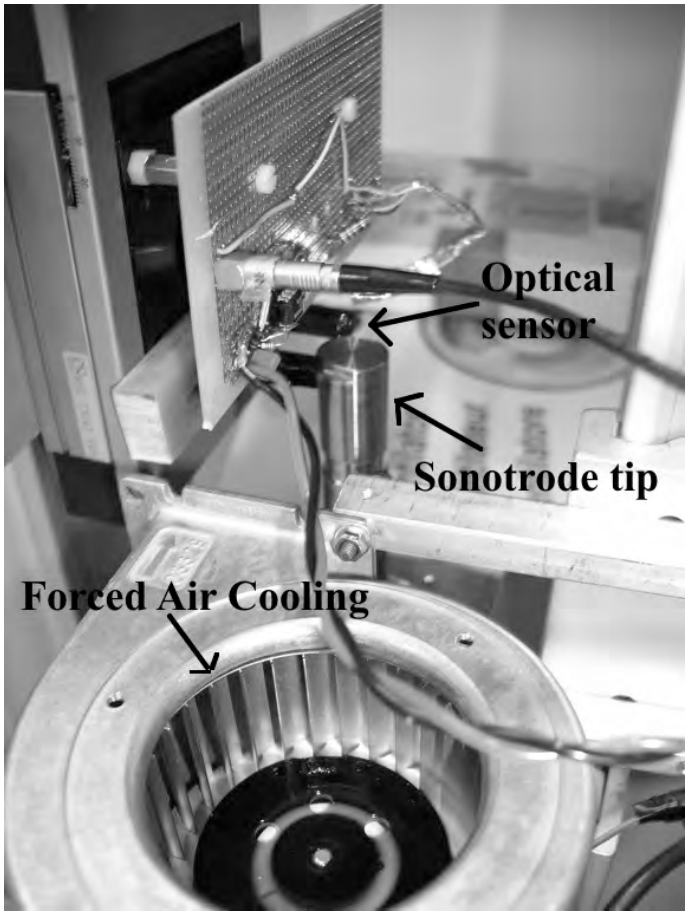

Figure 4.3: The magnitude of the vibrational amplitude was measured by an optical sensor.

amount using a micrometer.

The free end (tip) of the sonotrode was placed between the optical sensor, as shown in Figure 4.3. A micro-mover with a resolution of 0.1 μm was used to move the tip between the sensors in order to do the calibration. The vibration amplitude was of the order of 10-20 μm and the corresponding voltage range was 60-120 mV. At the smallest detectable displacement of 0.1 μm the corresponding voltage value was thus 0.6 mV. The amplitude of the AC signal from the oscilloscope could be read with a precision of $\pm$ 1 mV, so the accuracy of the displacement amplitude measurement was within $\pm$ 0.2 μm or $\pm$ 1-2 %.

The exact frequency of the vibration was also measured by the oscilloscope used in spectrum analyzer mode. This was important when calculating the number of cycles. In addition, the effective elastic modulus of the material was calculated based

on the measured resonant frequency. The displacement amplitude was kept constant during every run, so the experiments performed were strain controlled fatigue tests.

4.2.1 Sonotrode design for ultrasonic fatigue experiments

ANSYS FEM (Finite Element Method analysis software by ANSYS, Inc.) software was used to design the sonotrodes. Few analytical calculations were conducted in order to cross check the results. A dog-bone shaped design was selected for the sonotrode design and a typical geometry is shown in Figure 4.4. The maximum stress is a narrow zone near the rounding in the gage area resulting in an easily detectable fatigue damage. The heat generation during cyclic loading was relatively low due to the high stress concentration. A forced air cooling was sufficient for the cooling.

The element type used in the analysis was a rectangular shape (8 nodes Plane 82) in axis-symmetric mode. The element side length was typically 0.1-0.5 mm. An alternating cyclic force load with an amplitude of 1 N was applied to one end representing the interface to the booster. The results obtained from ANSYS were the resonant frequency and the ratio between the tip displacement amplitude and the stress amplitude distribution in the sonotrode. The maximum value of the stress was determined from this distribution.

Figure 4.4 presents a typical ANSYS simulation model of a sonotrode. The stress contours show the location and value of Von Mises stress. The maximum stress is located at the junction between the radius and the straight cylinder part of the gage. Figure 4.5 presents the internal stress profile from the surface to the symmetry axis in the center of the sonotrode at the longitudinal position of maximum stress. One can see that the stress level on the surface is typically a factor of two higher than in the center. This non-uniform condition was made intentionally, because in the RF cavities the stress is also concentrated close to the surface and, thus, the damage is expected to initiate in the surface. Figure 4.6 presents the stress profile on the surface along the longitudinal axis. It can be seen that the stress outside the gage area is practically zero and the peak stresses close to radiuses were about 50 % higher than the stress elsewhere in the gage area. It should be noted that the stresses in these figures must be normalized by the actual strain amplitude. A linear elastic relationship between these two by Hooke's Law [55] was assumed as the stress amplitudes of interest at ultra high cycle fatigue are low and well below the yield strength of the alloys selected.

In major part of the experiments the stress ratio for ultrasonic setup was fully reversed, $R = -1$, in equation (4.1) [56]. The stress ratio was varied in some

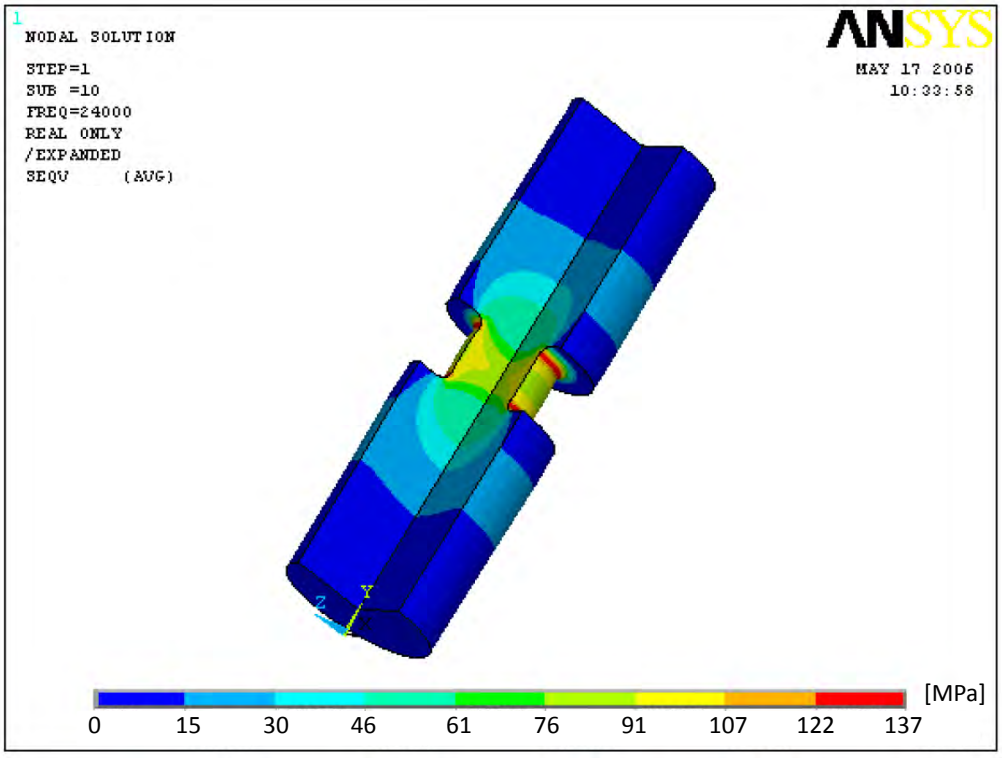

Figure 4.4: An example of a typical sonotrode simulated in ANSYS with the stress contours. The maximum Von Mises stress is at the radius of the gage area.

samples by applying a fixed pre-stressing. This will be discussed in Chapter 4.2.2.

$$R = \frac{\sigma_{min}}{\sigma_{max}} \tag{4.1}$$

where

R = stress ratio
$\sigma_{min,max}$ = absolute minimum and maximum stresses of cyclic loading

The damage criteria used in the initial ultrasonic experiments was a macroscopic fracture. This condition was detected by using a diagnostic output of the ultrasonic generator control system. The UIP250 has an operating frequency range of $24 \pm 1\ kHz$. When the frequency of the sonotrode is out of range, the device outputs an error condition. This can also happen if the resonant frequency of the sonotrode

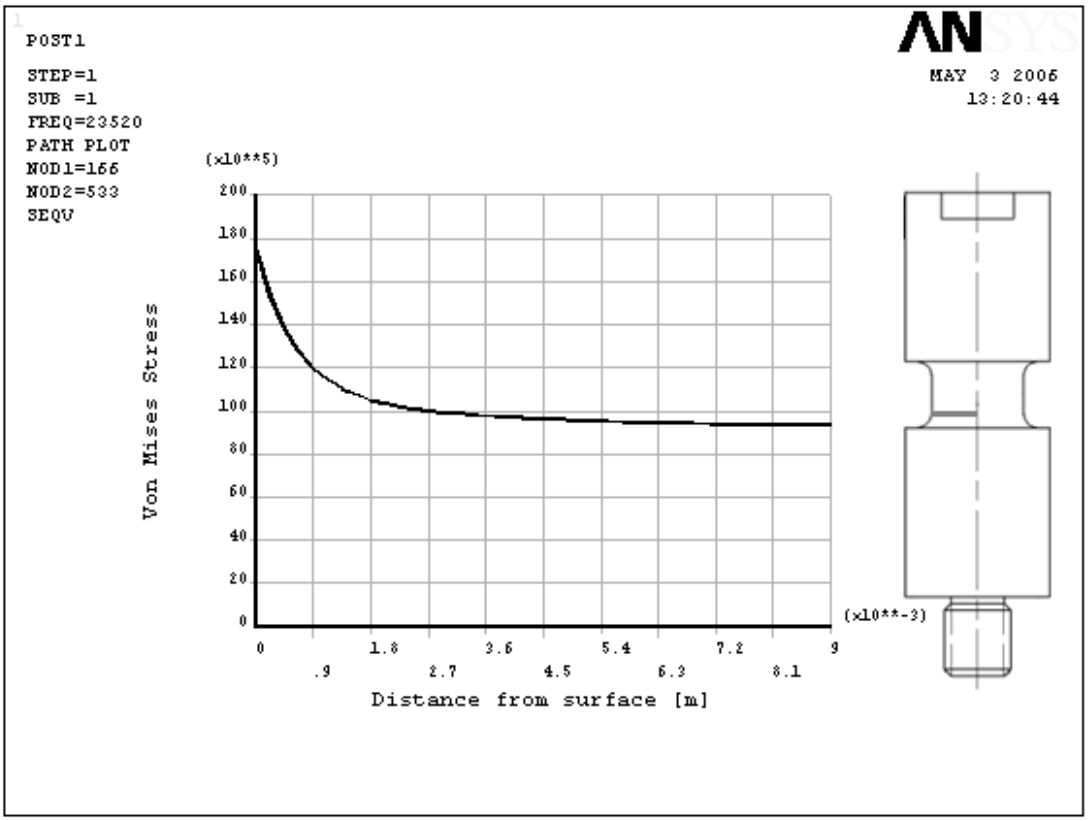

Figure 4.5: The stress profile perpendicular to the longitudinal axis of the sonotrode at the point of maximum stress, from surface to central axis. (red line in the drawing on the right).

changes during a run. A crack in a sonotrode changes its resonant frequency. It was calculated by ANSYS and also measured experimentally for the shapes used, that when a crack reaches typically a depth of 2 mm the resonant frequency is about 1 kHz off and the device stops normal operation. During the crack propagation phase, when the resonant frequency of the sonotrode is changing, the system tries to keep the fixed frequency and amplitude until the frequency is off by 1 kHz. This transient off-resonant phase requires more power and the increase of the input power to the system was read from the control software of the device. The crack propagation time from zero to 2 mm was of the order of 1 - 5 s. The lifetime investigated by these ultrasonic experiments was from 10^7 to 10^{11} cycles. The shortest experiment (10^7) took about 600 s, so the crack propagation time was thus less than 1 % of the total number of cycles.

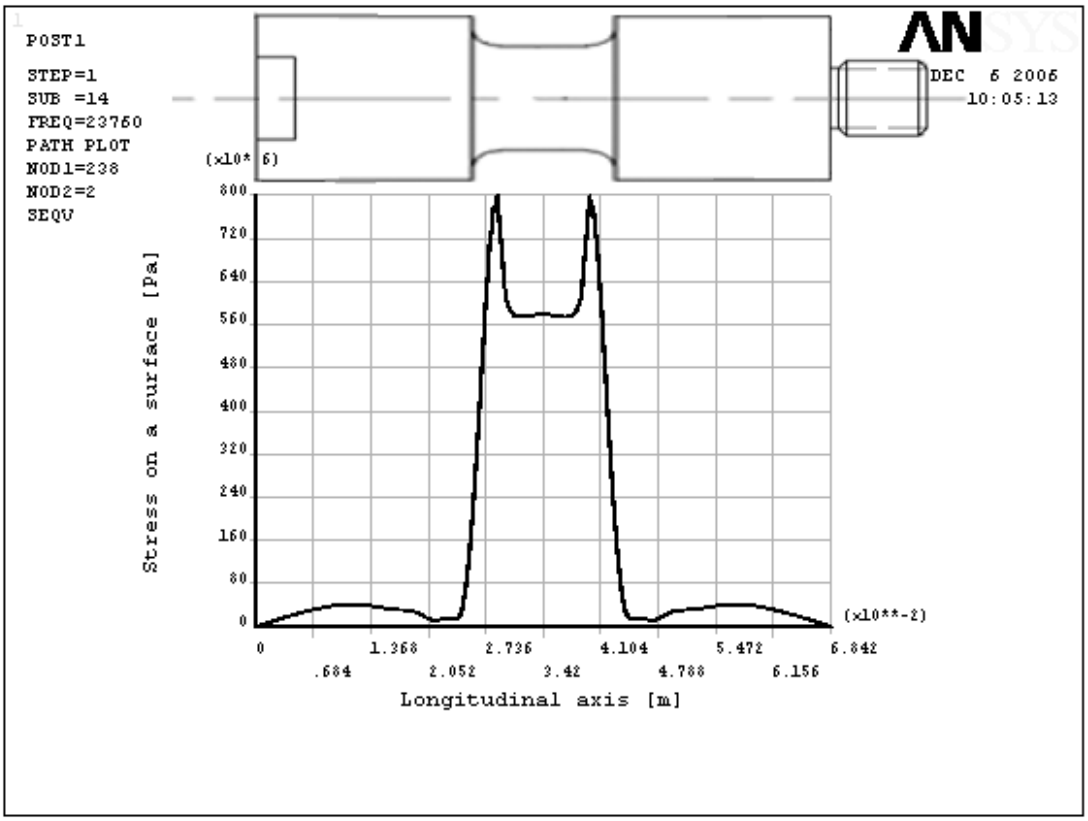

Figure 4.6: The stress profile on the surface along the longitudinal axis of the sonotrode. The peaks are located at the roundings in the gage regions.

4.2.2 Compressive mean stress experiments

A special pre-stressed sonotrode was developed in order to create conditions in a sonotrode closer to the RF induced thermal stress in the cavities, which is fully compressive $R = \infty$ (compr.), instead of fully reversed (tension - compression) stress condition. The idea was to introduce a compressive pre-stress of the sample, which is then exposed to the ultrasonic oscillations. If the static pre-compression in the sample is higher than the cyclic stress amplitude induced by the oscillations, then the stress in the sample is fully compressive. Figure 4.7 presents the assembly of the pre-stressed sample. A body made out of titanium alloy Ti6Al4V [57] holds a hollow sample made out of the desired copper alloy. This titanium alloy was chosen because of its good fatigue strength in order that it will not fail during an experimental run. The sample is compressed by screw threads and a nut on the body.

The magnitude of the pre-stress was determined by measuring the elongation of the

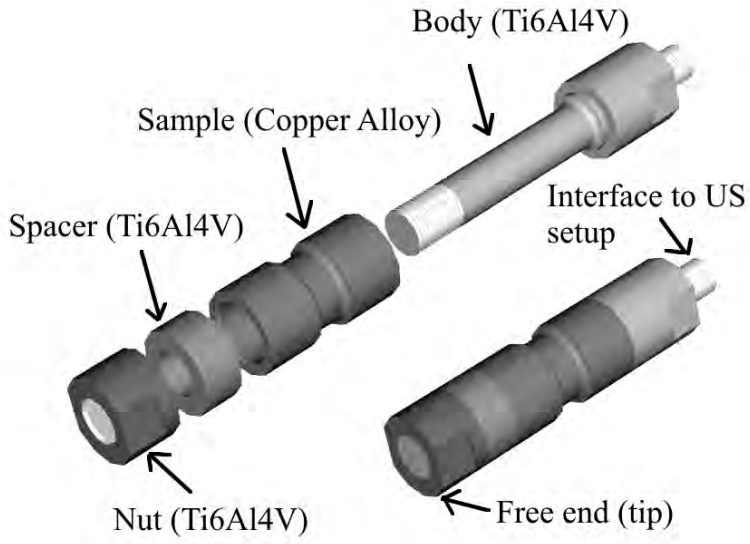

Figure 4.7: The exploded and assembled views of the special pre-stressed sonotrode. The sample made of the desired copper alloy is hollow, but the outside geometry of the assembly is identical to the standard sonotrodes.

Ti6Al4V bolt. Bolt's elongation of 50 μm corresponds to a static compressive stress of 200 MPa in the copper sample. The location of this stress is at the notch, which is the same for the cyclic stress.

The stresses were calculated in ANSYS. Figure 4.8 shows an example of a typical case. It can be seen that the stress in the Ti6Al4V bolt was about 20 % of the maximum stress in the gage area of the sample. Note that again, the stress values (Pa) in the ANSYS figure are relative and the absolute values are determined from the measurement of the strain amplitude using the LED device.

4.3 Pulsed laser fatigue experiments

The idea behind the laser experiment [58] is to simulate accurately the surface thermal fatigue of the RF cavities with the correct time structure and distance scale. In the case of RF cavities the heating occurs within the RF skindepth, which is 0.63 μm based on the parameters of June 2007, Chapter 3. In the case of pulsed laser the UV radiation is absorbed in the first nm of the surface and about 20 % of the radiation is reflected. The heat is thus deposited in the topmost surface layer

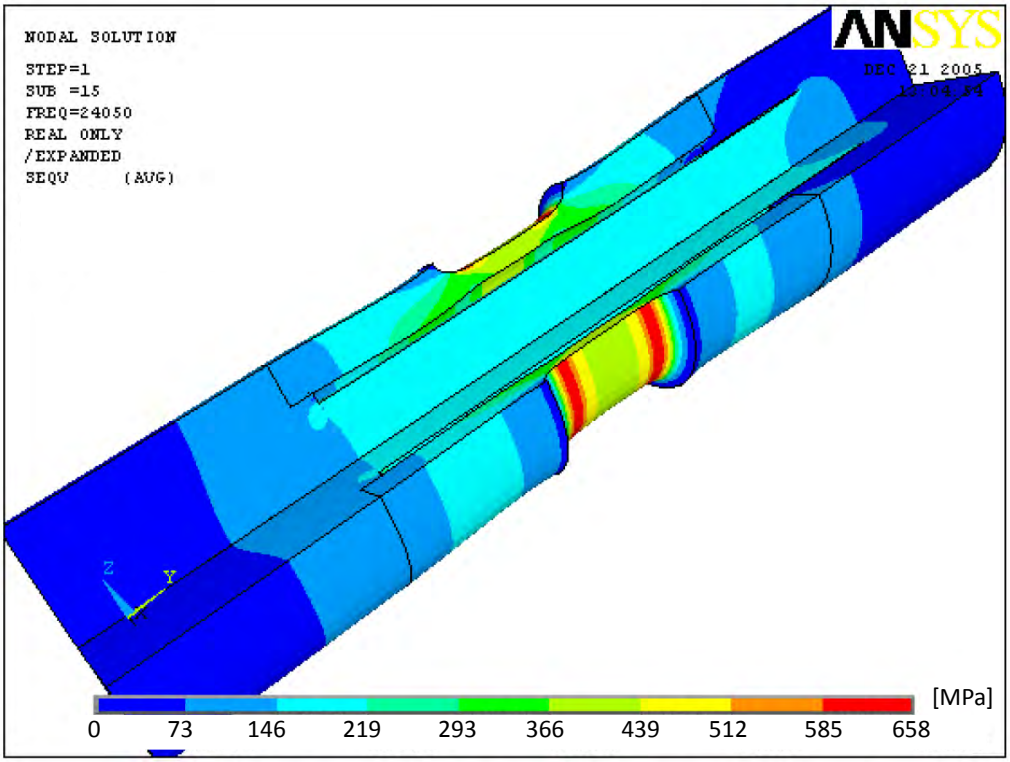

Figure 4.8: The compressive pre-stress and the cyclic stress amplitude were simulated in ANSYS.

but in both cases is small compared to the diffusion depth of the heat which is about 30 μm after 300 ns. The repetition rate of the laser pulses was 25 Hz, so the method was limited to the number of cycles in the range of about 10^3 - 10^7. The apparatus used was a pulsed excimer laser at 308 nm wavelength, see Figure 4.9. The sample shape was a disc made out of the desired material. The dimensions were about 25-50 mm in diameter and 5 mm in thickness. The samples were made by diamond turning. The sample was placed in a vacuum chamber (pressure $2 \cdot 10^{-7}$ $mbar$) in order to have similar conditions to RF cavities and to avoid induced chemical reactions. The target vacuum level for the CLIC cavities is about 10^{-8} - 10^{-9} $mbar$.

The irradiated spot on a sample was a rectangle of 1 mm by 1 mm. The intensity of the laser beam was measured by a CCD (Charge Coupled Device) camera. The temperature rise was then calculated taking into account all the relevant material and pulse power parameters. Details of the custom made computer program used for the calculations are presented in [59]. In Figure 4.11 an example of the temperature vs. time dependence and the profile inside C15000 for the laser pulse and a comparison to the 130 ns CLIC RF pulse is presented. 130 ns was chosen because this was the nominal CLIC pulse length at time the laser data was taken.

Figure 4.9: Picture of the laser setup in 2004. The laser is the orange box in the upper left hand corner and the sample is located in a vacuum chamber.

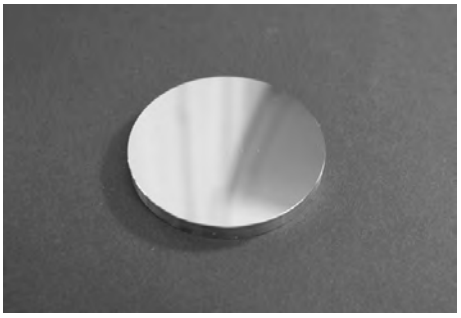

Figure 4.10: Diamond turned specimen for the laser fatigue experiments.

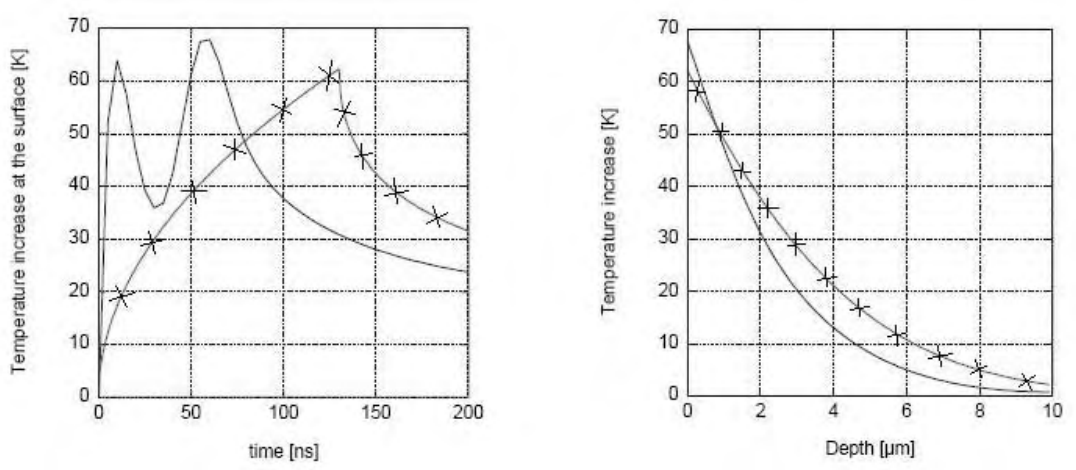

Figure 4.11: Left: Temperature variation on a C15000 surface for laser (normal line) at 0.1 J/cm^2 and for CLIC 130 ns RF pulse (crossed line) [58]. Right: Temperature profile inside C15000 at the peak temperature rise (after 60 ns for laser and 130 ns for RF pulse) [58].

The samples before and after irradiation were characterized in several ways. Scanning Electron Microscope (SEM) images were used to show degradation of surfaces as a function of irradiation conditions. The damage features are more numerous and larger when the laser energy density is higher and when the number of shots is increased for constant energy density. The SEM images of samples which were processed by RF show reasonably similar degradation except that RF fatigue samples also have opened cracks, because the cyclic loading on them was continued further than when the first damage was observed. Details of the RF fatigue tests are presented in the Chapter 4.4.

Another analysis technique, which is more quantitative, was the measurement of the average surface roughness (Ra) by means of a non-contact dynamic-focusing laser surface profilometer, see Figure 4.12. The samples had an initial surface roughness of Ra 0.01 μm and the damage criteria for tests was set to Ra 0.02 μm. This value is based on old CLIC parameters when the skin depth was about 0.3 μm and the criteria was set to roughly one tenth of the skindepth. For the CLIC cavities the criteria is likely to be different and the RF experiments are expected to help define the appropriate damage criteria.

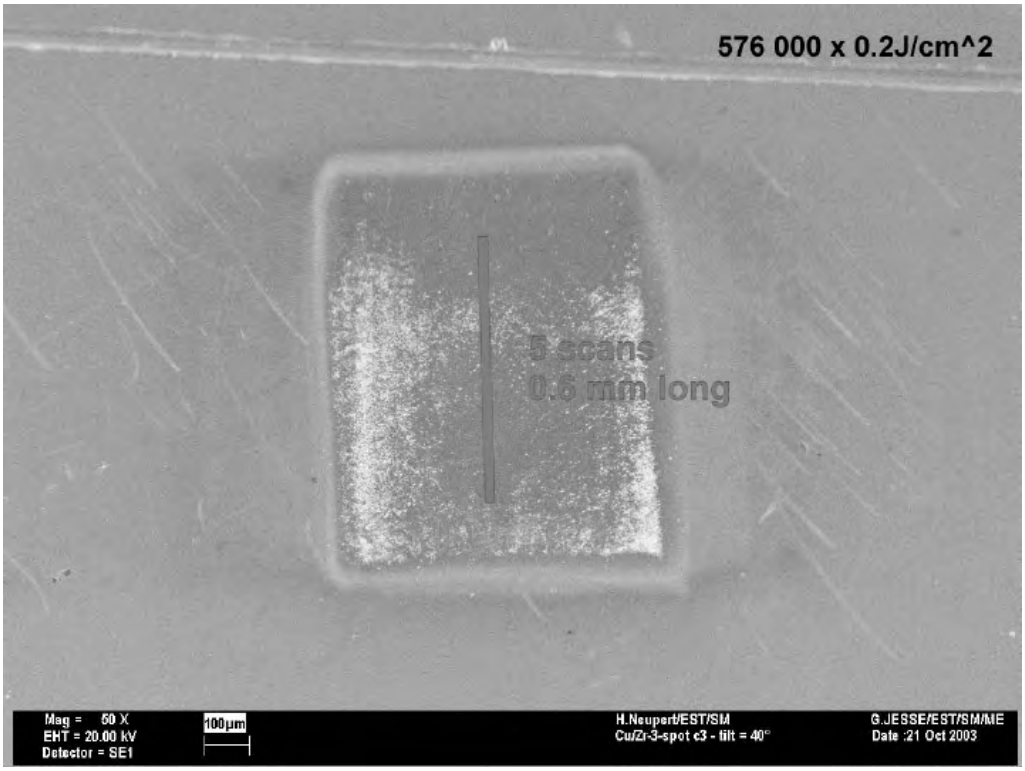

Figure 4.12: The average roughness (Ra) was measured on the laser spot by a laser surface profilometer.

4.4 Pulsed radio frequency fatigue experiments

Fatigue of CLIC accelerating structures is induced by radio frequency power so RF fatigue experiments were conducted in order to establish the damage criterion and to benchmark laser and ultrasonic fatigue data, to be able to make specific prediction of the number of cycles. The radio frequency fatigue experiments for this study were carried out at SLAC (Stanford Linear Accelerator Center, California, USA). The samples for the RF fatigue experiments were prepared the same way as for the ultrasonic and laser fatigue experiments (diamond turning) to allow direct comparison with the results.

The apparatus was originally developed to study superconducting materials for particle accelerator use. It is based on a resonant cavity with high quality factor and an interchangeable wall (the specimen), which can be made of different materials. A specially designed compact mode launcher excites the azimuthally symmetric cavity mode which, due to its current distribution, allows a gap between the cavity body and the changeable wall (the specimen). The specimen itself is a relatively simple

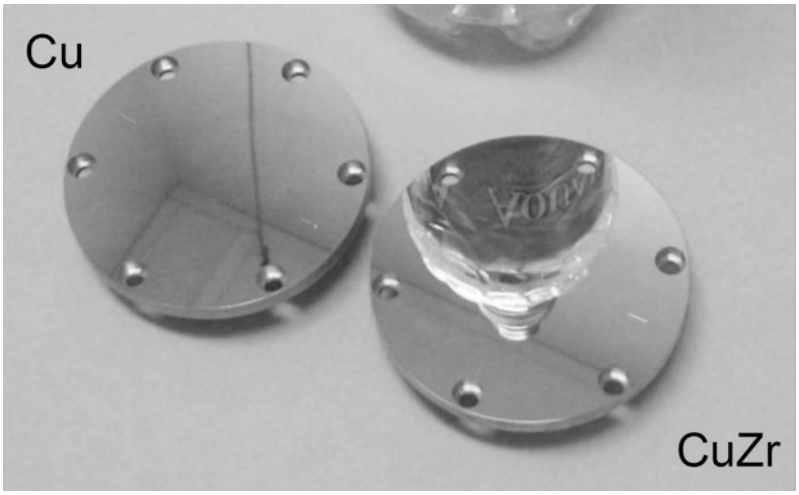

Figure 4.13: Mirror finished RF fatigue test specimens in C10100 and C15000.

piece, a flat disc with clamping holes. Specimens in C10100 and C15000 are shown in Figure 4.13.

The cavity is designed so that there are no high surface electric fields that could generate field emission and RF breakdowns. The cavity geometry is also designed to focus the maximum surface magnetic field on the test specimen, Figure 4.14. The magnetic field is distributed circularly, symmetrically, Figure 4.15, over the sample surface and its maximum value is a factor of two higher than elsewhere in the cavity. The magnetic field distribution on the specimen is smooth with relative values from zero to one over a distance of one *inch*, 25.4 *mm*. This allows simultaneous investigation of a range of stress amplitudes with one specimen.

The cavity is powered by a high power klystron with available input power up to 60 MW. For these power levels there is considerable average power induced on the surface, which increases the average temperature of the cavity. A powerful water cooling system was installed around the cavity in order to keep the average temperature as close to room temperature as possible, Figure 4.16.

The pulsed temperature rise on the surface is proportional to input power, and for example, 12 MW results in approximately 100 $^{\circ}C$ of maximum surface temperature rise [60]. The repetition rate of the klystron was set to its maximum, 60 Hz, in order to reach as high number of cycles as possible in a minimum time. The resonant frequency of the system was 11.424 GHz, so the skindepth, where the RF currents flow and heat up the surface was 0.64 μm, which is approximately the same as for the 11.944 GHz CLIC accelerating structures, 0.63 μm, Equation 3.2. A feedback

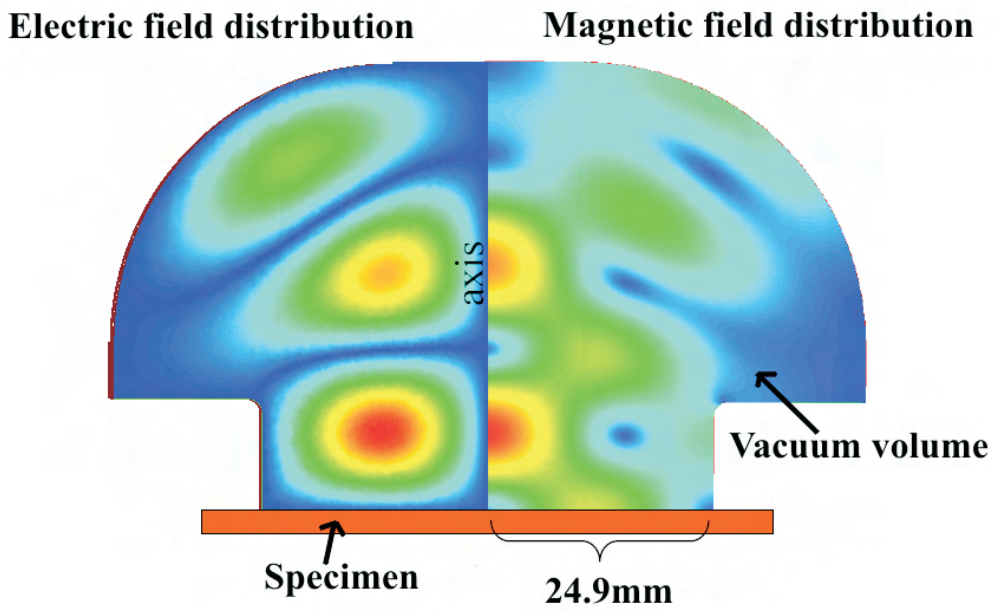

Figure 4.14: Schematic view of the electric and magnetic field distributions inside the cavity simulated by finite element electromagnetic software (Ansoft HFSS). The red contour is the maximum value and the blue is the minimum [60].

loop was used so that the low level RF drive tracked the resonant frequency and the quality factor Q of the resonance.

The basic features of the experimental setup used at SLAC can be seen in the schematics shown in Figure 4.17. The RF power is generated in the klystron and is then delivered to the test cavity by the waveguide system. When pulsed radio frequency waves arrive at input of the cavity, part of the signal is reflected back and part of it is absorbed in the cavity walls and thus heats the surfaces. Excessively high reflected power can cause severe damage for the klystron. In order to avoid this, a high power attenuator was installed in the waveguide system. The level of attenuation was chosen to let a significant fraction of the forward power to go through into the cavity and still absorb enough reflected power, limiting it to safe levels. The water cooling system of the attenuators transports the heat out of the system. After this attenuation the transmitted reflected power is low enough that it does not damage the klystron.

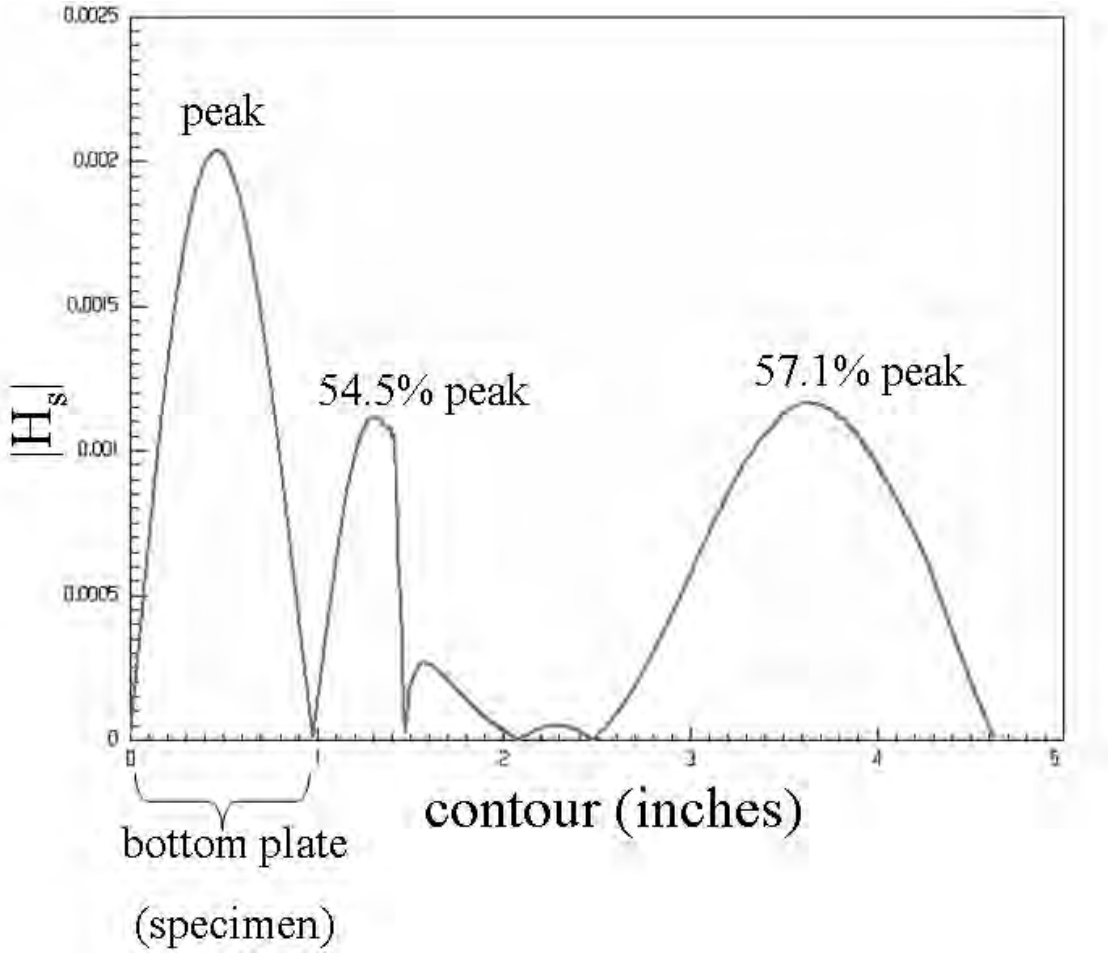

Figure 4.15: Magnetic field distribution in arbitrary units. The x-axis represents the projection of the cavity walls starting from the center of the specimen (bottom) to the top of the cavity [60].

The fields in the cavity can be determined from the forward and the reflected RF signals which are measured by directional couplers. A directional coupler is a RF component that picks up a known fraction of the main signal. The picked up signal is electronically processed and then captured by an oscilloscope. From this, the parameters of the main signal can be calculated. The total absorbed power in the cavity is basically the forward power minus the reflected power. The distribution of the temperature rise of the specimen inside the cavity can be simulated by finite element electromagnetic simulations and with the total power known, the temperature rise everywhere in the cavity can be determined.

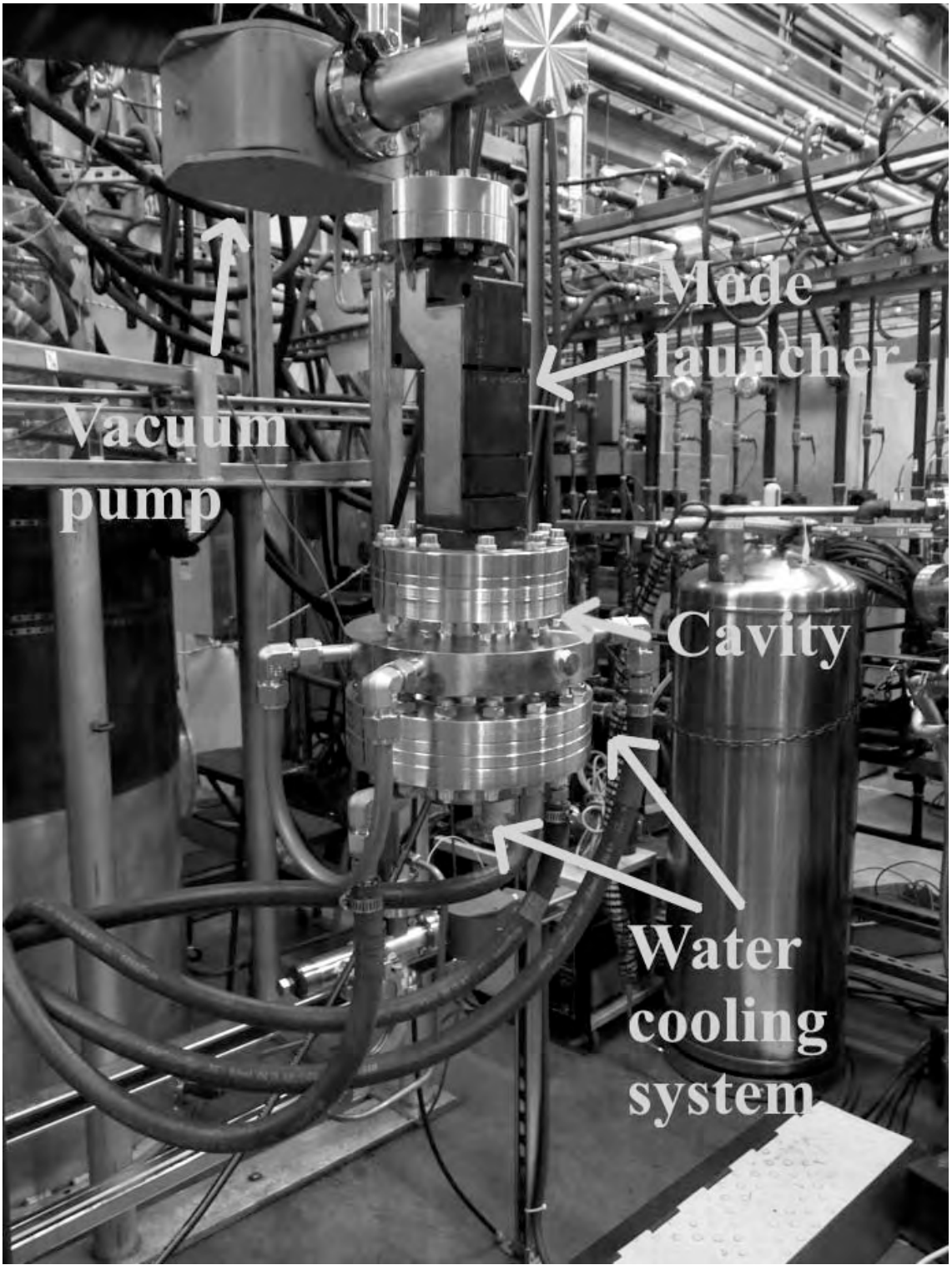

Figure 4.16: A close up view of the test cavity in the setup.

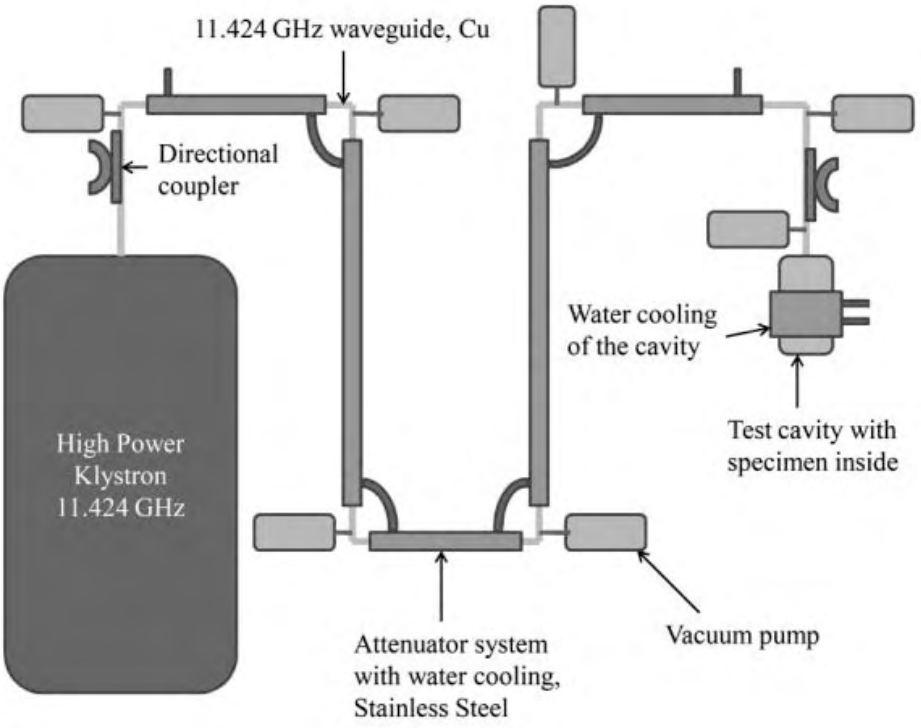

Figure 4.17: Schematics of the used radio frequency experimental setup.

5 Materials and their characterization

5.1 The selection of the candidate materials

The normal conducting accelerating cavities, which operate at room temperature, have traditionally been made out of pure copper. Cavities are usually vacuum brazed, so the copper comes out annealed. The most common grade is C10100, (Cu-OFE) oxygen free electronic copper. However, as was discussed in Chapter 3, annealed copper is not likely to meet the fatigue requirements of the CLIC scheme and increased strength would give performance improvements.

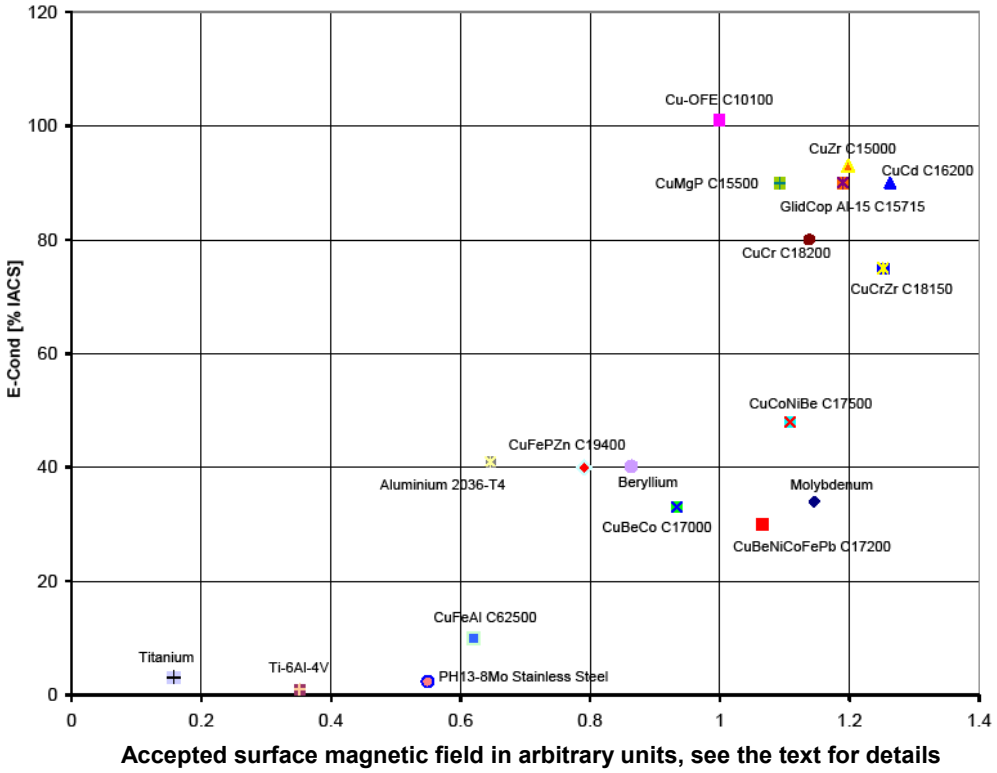

Figure 5.1: Comparison of different pure metals and alloys.

Figure 5.1 shows a material comparison where different pure metals and alloys are presented. By plotting the electrical conductivity in % IACS (International Annealed Copper Standard for conductivity) on the y-axis and the surface magnetic field calculated from the typical fatigue strength at 10^8 on the x-axis, one can class the performance of the materials. Magnetic field calculations are based on the

equations from (3.1) to (2.1) using the CLIC parameters of June 2007. The surface magnetic field is normalized to C10100 (pure oxygen free copper, 404900 A/m, 117 MPa). The y-axis is related to the relative electrical energy consumption and the x-axis as a relative accelerating gradient of the cavities. Materials in the upper right corner are the best candidates. These are without an exception high conductivity copper alloys. High electrical and thermal conductivities are crucial material parameters along with fatigue strength. For example, pure copper with a fatigue strength of 117 MPa is a factor of two better in corresponding magnetic field than high strength PH13-8Mo stainless steel (S13800) which has a fatigue strength of 1100 MPa [61]. The electrical conductivity for S13800 is 2.33 % IACS while for pure copper it is 101 % IACS. The materials selected for this study were all high conductivity copper alloys.

According to the Figure 5.1, copper cadmium C16200, is one of the most interesting alloys. However, cadmium is not a vacuum compatible material as it has prohibitively a high vapour pressure and crystalline whiskers [62] can grow on it which can cause short circuits. In addition it is toxic.

Table 5.1: Selected candidate copper alloys

UNS Name	Chemical composition	Thermal state
C10100 Cu-OFE	Cu 99.99 % min., O_2 5 *ppm* max.	Cold worked 50 %
C15000 CuZr	Cu+Zr 99.96 % min., Zr 0.13-0.2 %	cold worked 39 %, 40 %, 80 %, hot extruded
C15100 CuZr	Cu+Zr 99.96 % min., Zr 0.05-0.15 %	cold worked 39 %, 80 %
C15150 CuZr	Cu+Zr 99.96 % min., Zr 0.015-0.30 %	cold worked 39 %, 80 %
C15715 GlidCop® Al-15	Cu 99.62 % min., Al_2O_3 0.13-0.17 %	hot extruded
C18150 CuCrZr	Cu 98.85 %, Cr 1 %, Zr 0.15 %	cold worked 20 %

The subset of materials which has been selected for further study is presented in Table 5.1. In addition to material choice is the question of material's temper state, which can have a significant impact. The fabrication techniques which will eventually be chosen will have an influence on the accessible material states. For example assembly by brazing would lead to an annealed state. Also, preparation for good RF breakdown characteristics might require heat treatments.

Similar alloys appear also under thermal conductivity and yield strength consider-

ations [63], which are also key parameters. The pulsed temperature rise is proportional to thermal conductivity, Equation 3.4. The yield strength is a second order parameter, which contributes to general structural stability of the structures.

Alloys C10100, C15000 and C18150 were purchased from Luvata Ltd, Finland. C15000, C15100 and C15150 were donated for this study by Hitachi Cable, Japan. C15715 was purchased from SCM Metal Products, Inc., USA.

5.2 Materials characterization

The electrical conductivities of the candidate alloys were measured by the Forster 2063 apparatus (standard ASTM E1004 [64]), the tensile properties by the UTS 200 tensile testing facility (standard ASTM E8/E8M [65]) and the Vicker's hardness values by the Wolpert W-Testor hardness indentor (ASTM E92 [66]). The material characterization results are shown in Table 5.2.

Table 5.2: Properties of the candidate copper alloys.

UNS Name	State	Yield strength $[MPa]$	Tensile strength $[MPa]$	Hardness HV30	Electrical conductivity [% IACS]
C10100	Annealed	49	216	40	101
C10100	Cold worked 50 %	313	323	93	101
C15000	Hot extruded	72	225	46	82
C15000	Cold worked 39 %	323	370	120	93
C15000	Cold worked 80 %	386	428	130	93
C15100	Cold worked 39 %	309	315	115	94
C15100	Cold worked 80 %	364	407	121	94
C15150	Cold worked 39 %	299	335	106	97
C15150	Cold worked 80 %	344	349	117	97
C15715	Hot extruded	318	339	128	92
C18150	Cold worked 20 %	386	393	147	80

The roughness measuring device used was a non-contact dynamic focusing laser surface profilometer, the Rodenstock RM600 (ASME B46.1 - 2002 [67]). The lateral resolution of the device is 0.005 μm.

5.3 Pure oxygen-free copper

Cu-OFE C10100, pure oxygen-free electronic copper (Table 5.1), is a grade made for electrical industry and for vacuum applications, where high purity is a key factor. Pure copper is ductile material, which can be strengthened by work hardening, which is a commonplace technique used to improve the strength of metallic solids [55]. The effect of work hardening is the largest on the yield strength and the hardness of the material. When a ductile metal is deformed plastically, the change of shape is carried at the microscopic scale by dislocations and twinning. Dislocations are created by stress and the material is deformed by their movement. When the deformation of material is continued they start to interfere with each other, blocking their mobility and thus increasing the strength and decreasing the ductility. The contribution of work hardening to the yield strength of pure metals can be estimated by the dislocation density and the shear modulus as [68],

$$\Delta\sigma_y = G \cdot \alpha \cdot \sqrt{\rho_d} \tag{5.1}$$

where

$\Delta\sigma_y$ = yield strength
ρ_d = dislocation density increase
G = shear modulus
α = material parameter

Cold working is a general term which can be accomplished by cold forging, cold rolling and cold extrusion for example. It is often a technique in the fabrication process of metals which combines the work hardening of the material and the shaping of the metal into its final form. By annealing the metal at a high temperature, the dislocation density is decreased by recovery and re-crystallization and the metal is softened again.

Measured mechanical and physical properties of the used C10100 alloy are presented in Table 5.2.

In this manuscript the quantity cold working ratio (%) is often used. This is defined as a reduction in the cross sectional area when producing rod products by cold drawing. For example 80 % cold worked means that the final cross sectional area is 20 % of the initial one and 40 % cold worked that the final cross sectional area is 60 % of the initial.

5.4 Precipitation hardened copper alloys

CuZr grades C15000, C15100 and C15150 are precipitation hardened oxygen-free coppers alloyed with zirconium (Table 5.1). Adding a small amount of zirconium to copper raises the softening temperature significantly. The electrical conductivity remains still close to pure copper with increased strength due to fine zirconium precipitates. As the zirconium content is reduced, the electrical conductivity between the three grades slightly increases, but at the same time the strength is reduced.

CuCrZr C18150 is a precipitation hardened copper alloyed with chromium and zirconium (Table 5.1). This is also a high conductivity and high strength alloy as the copper zirconium. The solubility of zirconium to copper is limited so the strength can be further increased by adding chromium to the alloy. The strength of CuCrZr is higher than that of the CuZr alloys, but the addition of chromium results in lower electrical conductivity.

Precipitation hardening is a technique where a second phase, like an inter-metallic, is precipitated in an alloy from a supersaturated solid solution. The fine particles of the precipitate formed by the second phase impede the movement of dislocations and defects in a crystal lattice of the first phase. This hardens the material, because the dislocations are the major carriers of plastic deformations in a material. Depending on the tempering history of a component, precipitation can produce many different sizes of particles, which results in very different properties. In the tempering process of precipitation hardening, alloys must be typically kept at an elevated temperature for a fixed period of time to allow precipitation to take place, a procedure which is called aging.

Precipitation hardenable copper alloys are mainly used in electrical and heat conduction applications, where good mechanical strength is also required. The tempering treatment must therefore be optimized to achieve a good mechanical strength along with good electrical and thermal conductivities. The process for the alloys concerned consists of a solution heat treatment at 900 - 925 $°C$ followed by fast cooling (quenching) in water for example. The time spent at the solution treatment temperature should be minimized in order to limit the oxidation and grain growth. Aging can be done right after the quenching. Cold working can be applied before and/or after the aging. If no cold working is applied between solution heat treatment and aging, then the aging should be done at 500 - 550 $°C$ for 1 to 4 hours. If the material has been cold worked after the solution heat treatment and quenching, then the aging temperature can be reduced to 375 - 475 $°C$. The best strength properties can be achieved when the cold working is applied twice, prior and after the aging treatment. Measured mechanical and physical properties of the used precipitation hardened alloys are presented in Table 5.2.

5.5 Dispersion strengthened copper alloys

GlidCop® Al-15 C15715 is an aluminum oxide (alumina, Al2O3) dispersion strengthened copper (Table 5.1). The electrical and thermal conductivities are close to pure copper whilst the strength is significantly higher. It consists of a copper matrix containing finely dispersed particles of alumina. The dispersed alumina particle phase is thermally stable so that it acts to retard recrystallization of the copper. It is produced using an internal oxidation powder metallurgy process where aluminum oxide is formed in the Cu matrix. The electrical conductivity was measured to be 92 % IACS and is independent of the cold working ratio and thermal state of the component. The yield and tensile strengths are about 25 % and 10 % higher (respectively) for cold worked compared to annealed states.

The main advantage of the dispersion strengthening compared to precipitation hardening is the minor dependence of the temper state on the mechanical and electrical properties. Dispersion strengthening differs from precipitation hardening in that there is a metal or alloy matrix which is compounded with chemically and thermally stable sub-micron size particles of a nonmetallic phase, usually a ceramic. The actual strengthening mechanism is the same as for precipitation hardening. The particles act as barriers for the dislocation movement. Because the second phase particles are chemically and thermally stable, unlike the precipitated inter-metallics, good mechanical and electrical properties can be preserved even after exposure to elevated temperatures. The main disadvantage is that the second phase particles, which are often a hard ceramic, make the machinability and formability of the dispersion strengthened materials difficult. Ceramic particles may also increase the brittleness compared to the original matrix material. Measured mechanical and physical properties of the used dispersion strengthened alloy are presented in Table 5.2.

6 The results of the fatigue experiments

6.1 Results of ultrasonic fatigue experiments

6.1.1 Compressive mean stress experiments

The method of ultrasonic experiments with a compressive mean stress was described in Chapter 4.2.2. The material selected for these experiments was C18150, which is a copper chromium zirconium, age hardened and 20 % cold worked alloy, see Chapter 5.4. The sonotrodes for reversed $R = -1$ and fully compressive $R = \infty$ (compr.) and $R = 6$ (compr.) (4.1) conditions were prepared from the same bar. For the definition of R values, see Equation 4.1. Figure 6.1 shows the results of these sonotrodes. The reversed conditions are represented by the diamonds and the pre-stressed ones by the rectangles. The fitted curve corresponds only to the data points for the reversed stress conditions. It can be seen that the fatigue strength is the same or could be even slightly higher when compressive mean stress is applied. At least it seems not be lower.

6.1.2 Crack propagation rates in different materials

The crack propagation rate was measured in the ultrasonic experiments. Once the crack was initiated it advanced inside the specimen. The crack advancement could be detected by the control unit as described in Chapter 4.2.1. One alloy showed a different qualitative behavior to the others. Under cyclic loading by ultrasound, the crack advanced much faster for GlidCop than for the other materials. GlidCop® Al-15 differs from the others as it is a dispersion strengthened alloy while the others are pure metals or precipitation hardened alloys, see Chapter 5.1.

The fatigue cracks of sonotrodes of GlidCop® Al-15, C15000 and C18150 were pulled open by tensile testing apparatus for microscopic investigations. Figures 6.2, 6.3 and 6.4 show three opened sonotrodes, which had undergone similar ultrasonic fatigue experimental runs. The fatigue crack has a similar shape in all three, which indicates that the crack was initiated in similar way from one point near the surface and propagated in the same way. It can be seen that in GlidCop® Al-15 the crack surface is smoother and larger in the surface area compared to the other two, and the crack depth is approximately the double.

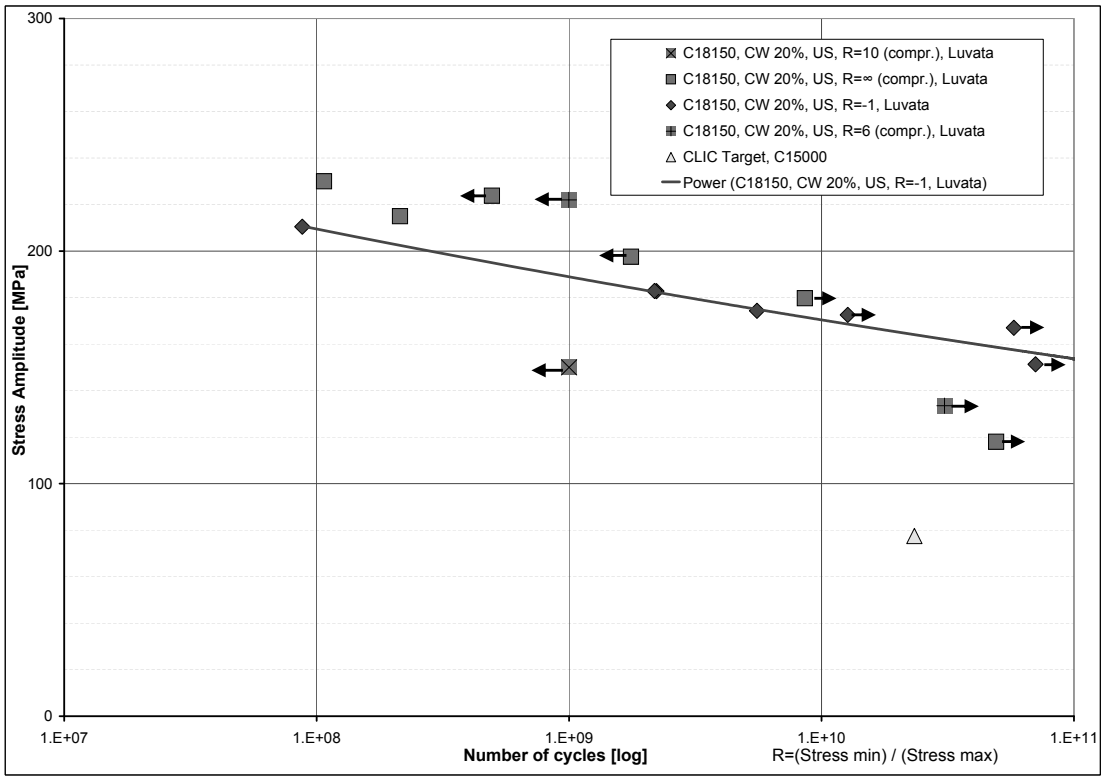

Figure 6.1: Wöhler curves for C18150. Diamonds are for reversed stress condition and the blue curve is the corresponding fitted curve. Rectangles are for a fully compressive stress condition.

The crack advancement in GlidCop® Al-15 is thus faster than for other alloys, but this parameter was not quantified because it is not important for the ultra high cycle fatigue, where the crack initiation dominates the fatigue life.

CuZr alloys showed systematically a straight crack path below 10^8 cycles and highly deflected following crystallographic planes above 10^8.

6.1.3 Influence of the zirconium content on UHCF strength of copper zirconium alloys

Different copper zirconium alloys were studied. Samples for ultrasonic experiments made of C15000, C15100 and C15150 from two different suppliers were prepared. The difference between these is basically that the nominal zirconium contents are

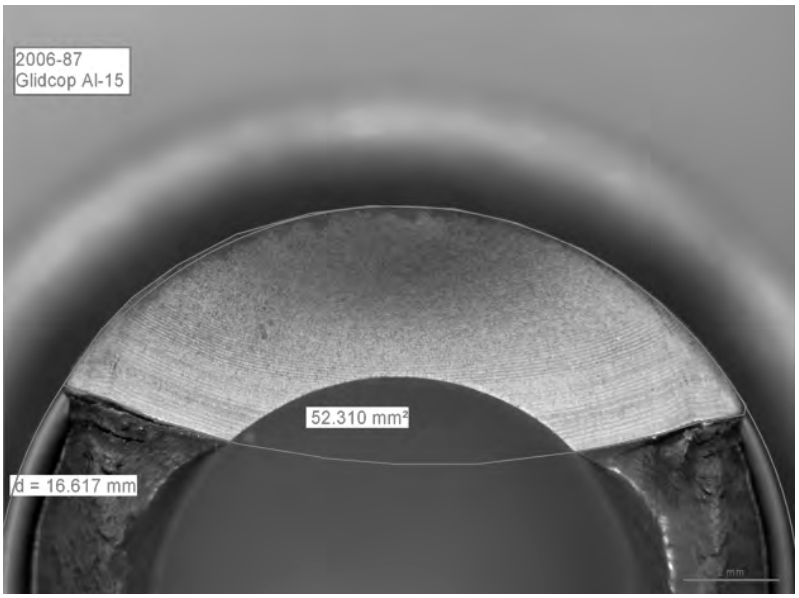

Figure 6.2: Opened GlidCop® Al-15 sonotrode. The fatigue crack is the "half circle" highlighted in red.

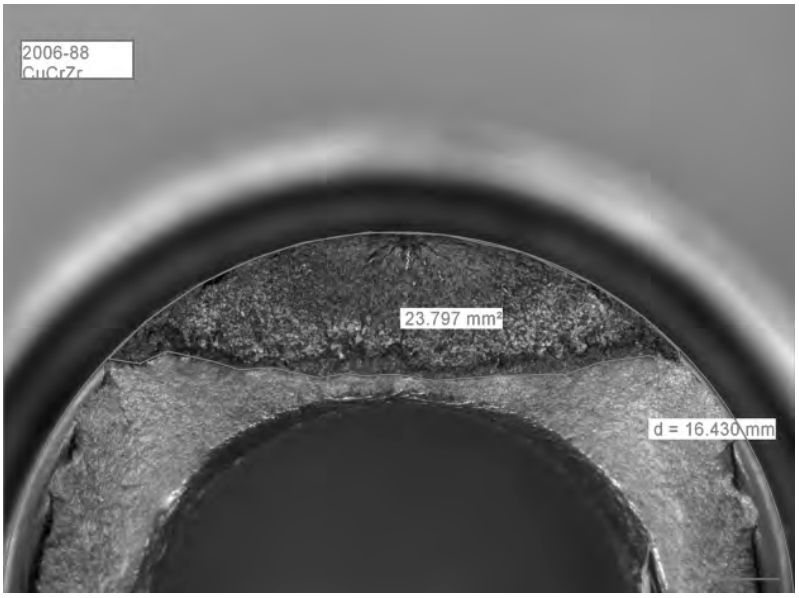

Figure 6.3: Opened C18150 sonotrode. The fatigue crack is the "half circle" highlighted in red.

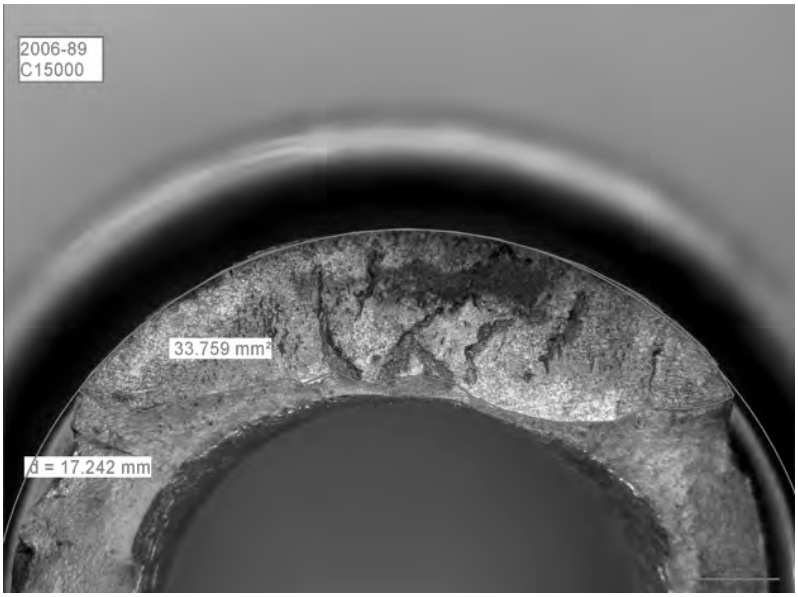

Figure 6.4: Opened C15000 sonotrode. The fatigue crack is the "half circle" highlighted in red.

0.13-0.2 wt.%, 0.05-0.15 wt.% and 0.015-0.03 wt.% respectively (wt.% = weight percentage). Figure 6.5 shows the results of these specimens. Pure copper (Cu-OFE, C10100) is also shown as a reference material. The thermal state of the CuZr alloys is similar. C10100 differs from those as it is not a precipitation hardenable material and the cold working ratio is 50 % compared to 39 % of the CuZr alloys.

The results clearly show the influence of the zirconium content on fatigue strength, where the highest alloying rate is also the strongest. Alloying generally increases the electrical resistivity, which has detrimental effects on the tolerable magnetic field. Figure 6.24 shows that the ordering of materials remains the same, due to the relative smaller increase of the electrical resistivity than the increase of the fatigue strength.

The zirconium content of C15000 is about at the saturation of zirconium precipitates which can be formed in a copper matrix. A higher concentration would result in an insoluble zirconium phase in the matrix which would decrease the fatigue strength [69] and the electrical conductivity dramatically.

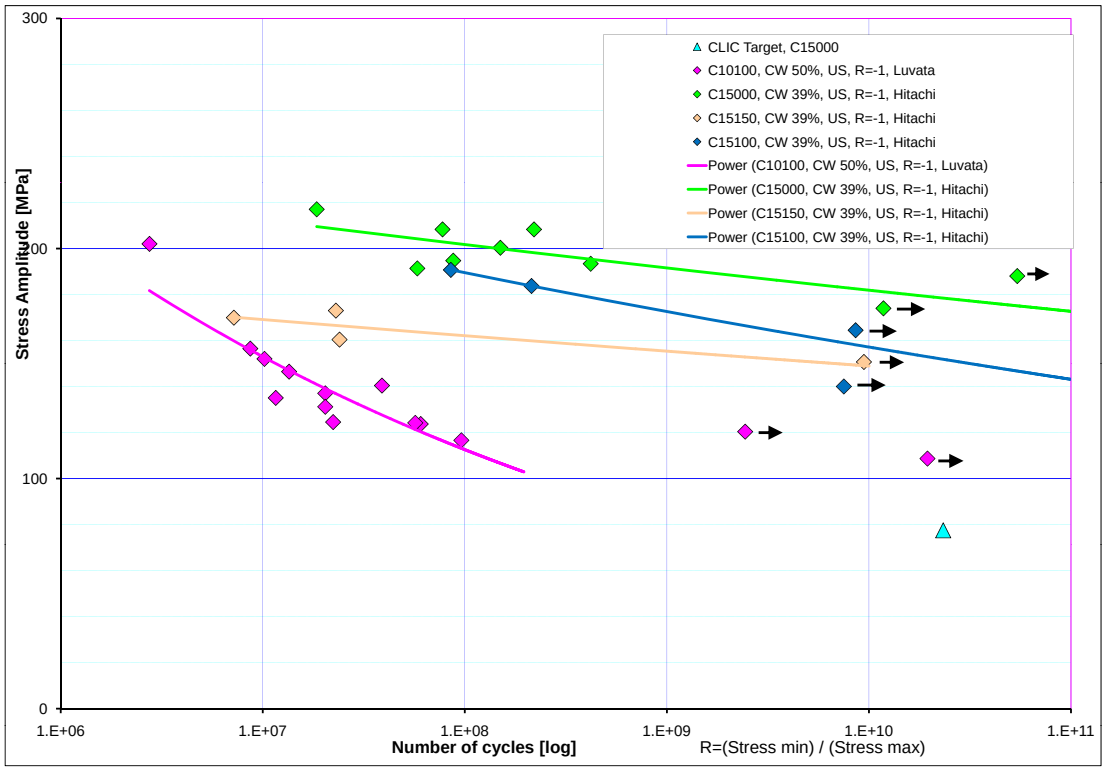

Figure 6.5: Wöhler curves representing the ultrasonic fatigue experimental results of the different copper zirconium alloys (C15000, C15100 and C15150) and pure copper (C10100).

6.1.4 Influence of cold working ratio on the UHCF strength of copper zirconium alloys

The fatigue strength for the three copper zirconium alloys was measured at two different cold working ratios, 39 % and 80 %, by the ultrasonic setup. The results are shown in Figure 6.6 and no difference at UHCF range between the two states can be distinguished so each alloy has a similar fatigue strength in 39 % and 80 % cold worked states.

6.1.5 Surface roughening at UHCF range

During the ultrasonic fatigue experiments, surface roughening of most of the samples was observed. This occurred at the point of the maximum stress, which was located

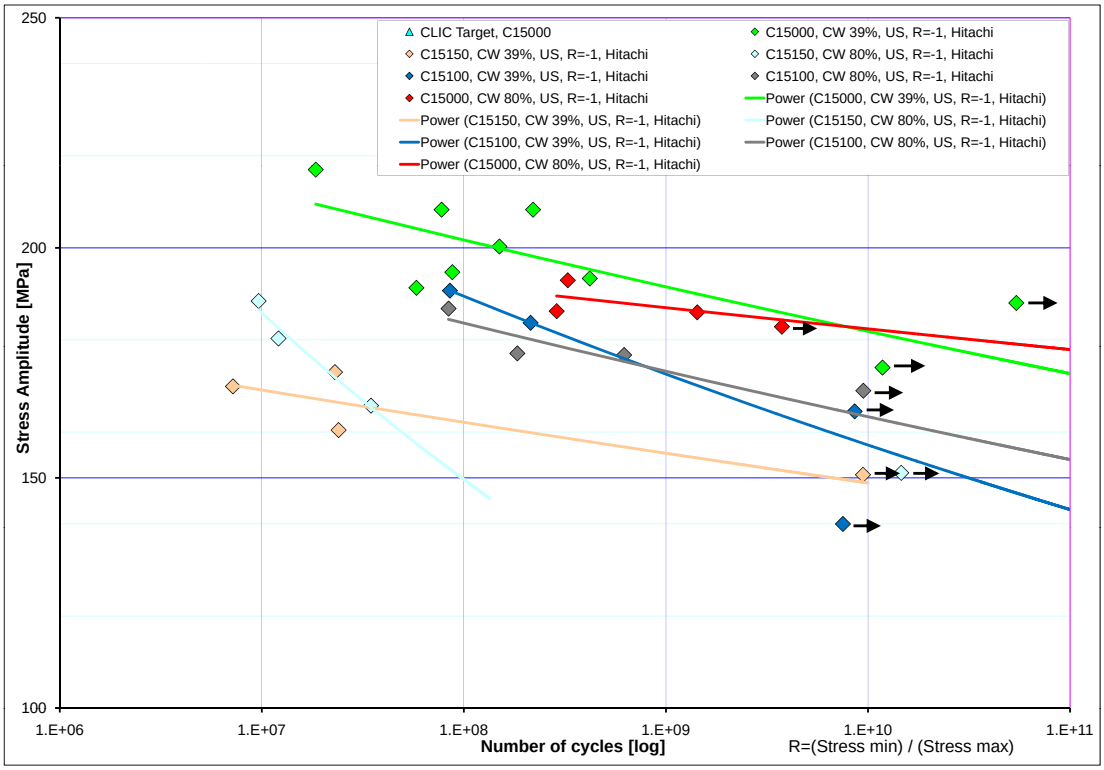

Figure 6.6: Wöhler curves of experimental ultrasonic fatigue results for the three copper zirconium alloys (C15000, C15100 and C15150) in different cold working states, 39 % and 80 %.

in the rounding of the gage area. Roughness appeared for specimens especially at the ultra high cycle regime having low cyclic stress amplitudes. Figure 6.7 shows an optical image of the roughening.

A sonotrode made of 39 % cold worked C15000, which reached $7.11 \cdot 10^{10}$ cycles without a fracture at 188 MPa, was inspected with a scanning electron microscope (SEM). The Sonotrode was cleaned before SEM imaging to remove possible oxidation. Figures 6.8, 6.9 and 6.10 show the SEM images of the same point at different magnifications. The images are taken at the point of maximum stress where the roughening was observed.

Figures 6.8, 6.9 and 6.10 clearly show some modifications of the surface microstructure due to the cyclic loading. The same phenomena also occurred for other copper alloys, like C10100, C15100, C15150 and C18150.

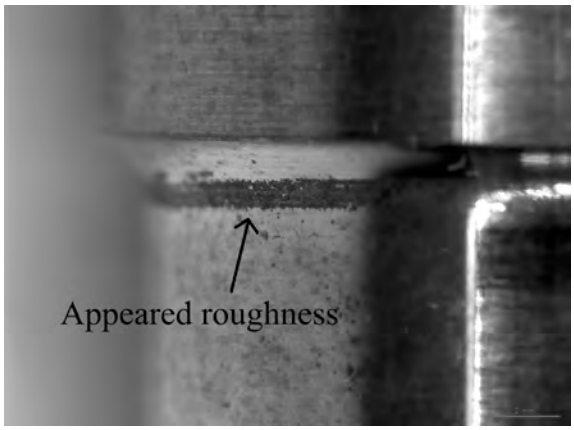

Figure 6.7: Most of the processed ultrasonic fatigue specimens experienced surface roughening at the zone of the maximum stress.

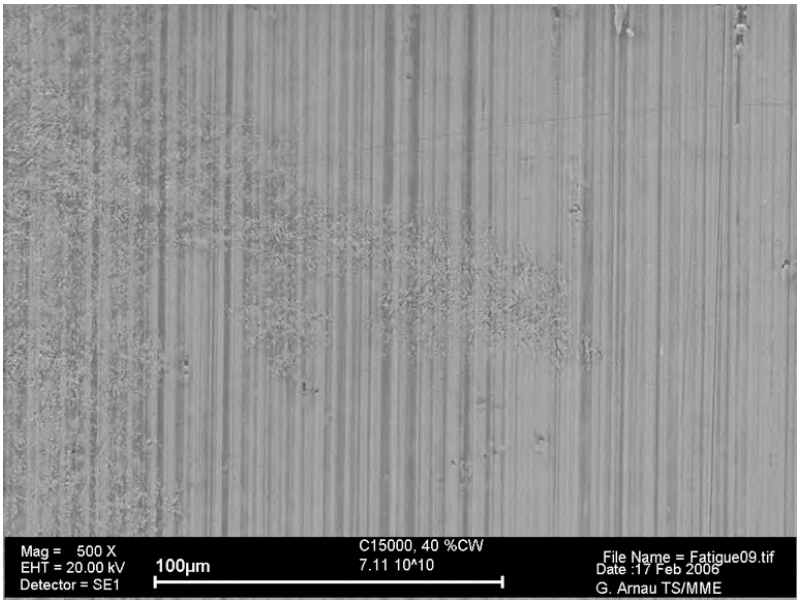

Figure 6.8: 500X SEM image of the sonotrode surface at the point of maximum stress, see the text for details.

The roughening of the surface is a critical issue, because it could disturb the RF currents that flow near the surface of the accelerating cavities. A simple experiment was launched in order to study if the applied stress amplitude has an influence on the roughening effect. There, the reference specimen of C18150 in a 20 % cold worked state was tested with ultrasound at 167 MPa and reached $5.78 \cdot 10^{10}$ cycles without a fracture, but surface roughness appeared. Then an identical sample was tested

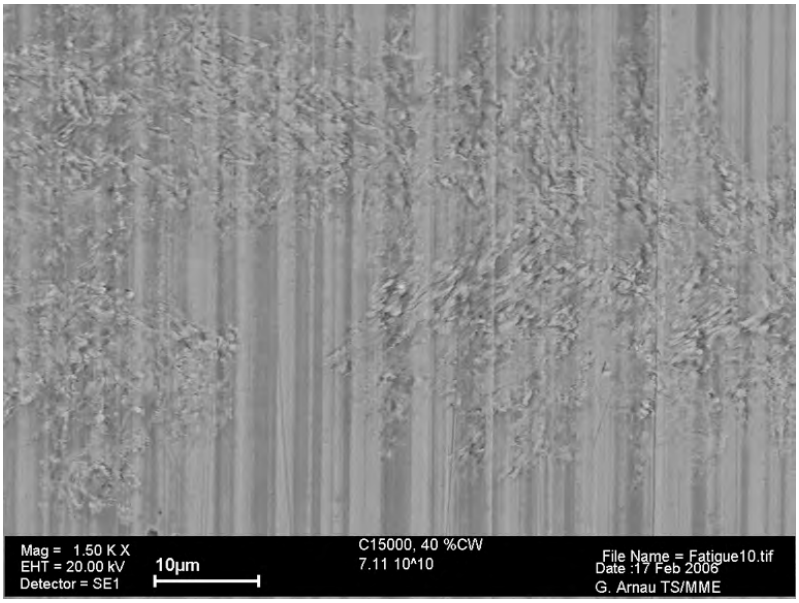

Figure 6.9: 1500X SEM image of the sonotrode surface at the point of maximum stress, see the text for details.

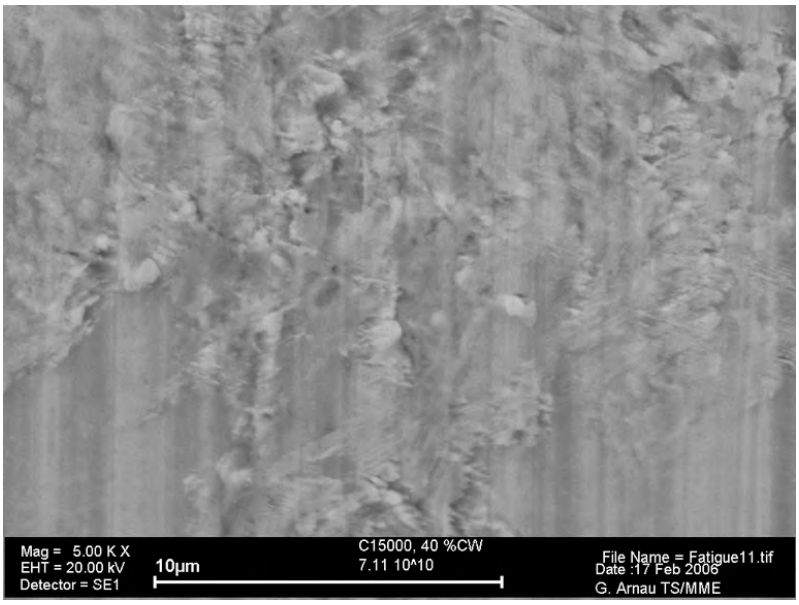

Figure 6.10: 5000X SEM image of the sonotrode surface at the point of maximum stress, see the text for details.

with a 10 % lower stress amplitude (151 MPa). This sonotrode reached $7.04 \cdot 10^{10}$ cycles without a fracture and without the appearance of surface roughness. This gives a strong indication that this surface modification is related to stress amplitude. Additional evidence comes from the fact that the sonotrodes shows this behavior only in the region close to maximum stress. The stress profile is shown in Figure 4.6, where the peak stresses at the roundings were 50 % higher than elsewhere in the gage area.

Table 6.1: The results of the surface roughening investigations.

UNS Name	Fabricated by	Stress amplitude [MPa]	Number of cycles	Appeared roughness	Fracture
C18150 CuCrZr	Flückiger	167	$5.78 \cdot 10^{10}$	yes	no
C18150 CuCrZr	Flückiger	151	$7.04 \cdot 10^{10}$	no	no
C15000 CuZr	VDL	236	$1.59 \cdot 10^{7}$	no	yes
C15000 CuZr	Flückiger	199	$9.2 \cdot 10^{7}$	yes	yes
C15000 CuZr	VDL	199	$1.79 \cdot 10^{8}$	no	yes
C15000 CuZr	Flückiger	197	$3.34 \cdot 10^{8}$	yes	yes
C15000 CuZr	VDL	197	$4.77 \cdot 10^{8}$	no	yes
C15000 CuZr	Flückiger	193	$5.47 \cdot 10^{8}$	yes	yes
C15000 CuZr	VDL	193	$1.29 \cdot 10^{9}$	no	yes
C15000 CuZr	Flückiger	191	$6.94 \cdot 10^{8}$	yes	yes
C15000 CuZr	VDL	191	$6.47 \cdot 10^{8}$	no	yes

After the observation of the surface roughening in a number of samples, another dedicated set of experiments to study this phenomena was designed to measure the growth of surface roughness. In order to carry out this, two sets of sonotrodes were prepared in C15000 in a 39 % cold worked and age hardened state. The geometry and the material of these two were identical, but two different suppliers were chosen to fabricate them. The first firm, VDL ETG (VDL Enabling Technologies Group, Netherlands) produces diamond turned surfaces with special custom made equipment using single crystal diamond tools, air bearings and optimized processing, where the last material removal is of a μm range. Flückiger (Switzerland) also uses single crystal diamond tools, but on conventional lathes. The initial roughness of VDL sonotrodes was measured to be Ra 0.05-0.1 μm and on Flückiger sonotrodes as Ra 0.1-0.2 μm. The number of cycles of the 5 pairs of sonotrodes varied from 10^7 to 10^9 and they showed identical final fracture fatigue strength within 5 %. The most significant difference of these two sets was that all the Flückiger sonotrodes did show induced surface roughness, but the VDL sonotrodes did not. The measurable surface roughness did not change for both sets of sonotrodes, even for the Flückiger sonotrodes, where the induced roughness was visible by eye. The results

of the ultrasonic experiments dedicated to the surface roughening investigations are summarized in Table 6.1.

Two explanations on why the roughening was not detected have been identified. The first is that the lateral resolution of the measurement device was too coarse (0.005 μm, see Chapter 5.2. However, this is contradicted if one considers the Figure 6.10, where the features seem to have lateral dimensions of the order of one μm. Another possibility is that the initial surface roughness was already too high and the average roughness measurement (Ra) cannot distinguish these new features from the background roughness. In order to quantify the induced roughness, a better initial surface finish would help for the future as well as an analysis with an atomic force microscope (AFM) for better lateral resolution. Other surface roughness parameters than Ra could distinguish these induced features.

6.2 Laser fatigue experimental results

The scanning electron microscope (SEM) pictures of the specimens tested show the evolution of the surface during the pulsed laser irradiation. Figures from 6.11 to 6.15 are SEM pictures before and after laser processing of C10100 (pure copper) in a 50 % cold worked state and C15000 (copper zirconium) in a 40 % cold worked and age hardened state. The corresponding data points can also be seen in the Wöhler curves, Figures 6.23 and 6.24.

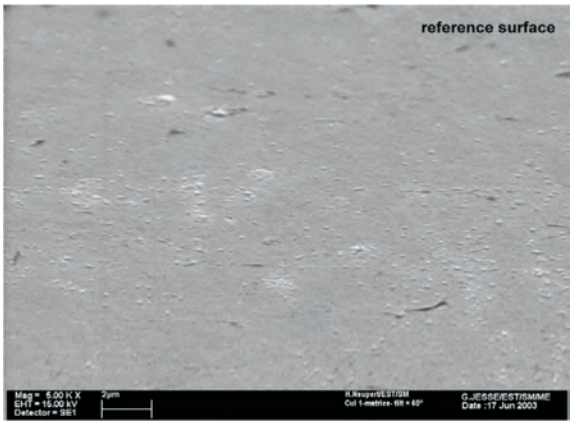

Figure 6.11: SEM image of the reference surface of C10100 laser test specimen.

The diamond turned surface of C10100 before testing are shown in Figure 6.11. After $6 \cdot 10^4$ cycles at 226 MPa cyclic stress amplitude, which are fully compressive

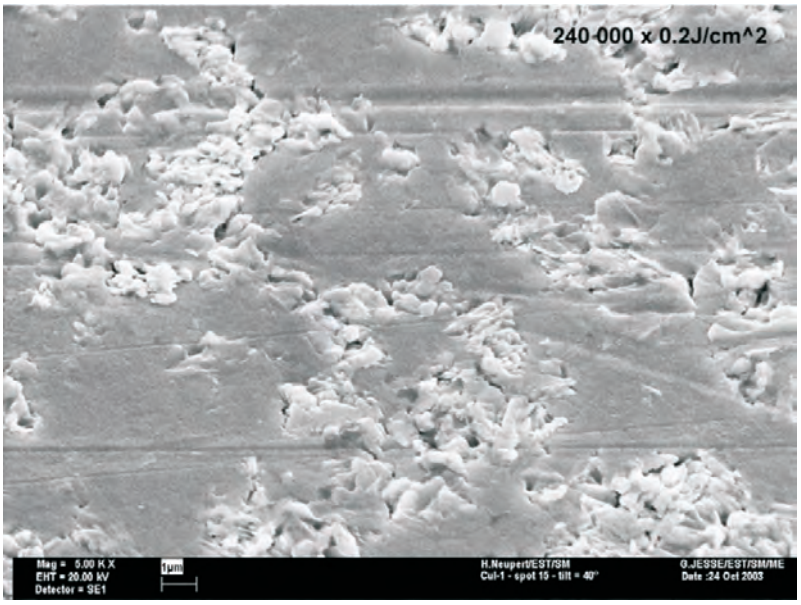

Figure 6.12: SEM image of the C10100 laser test specimen after $2.4 \cdot 10^5$ cycles at 226 MPa cyclic stress amplitude. The damage criteria of Ra 0.02 μm was exceeded already at $6 \cdot 10^4$ cycles.

thermal stresses in the case of the laser exactly as in the RF, the surface roughness was measured to be above the damage criteria of Ra 0.02 μm. The specimen was processed even further and at $2.4 \cdot 10^5$ the surface is shown in Figure 6.12 and the surface roughness was well above the damage criterion.

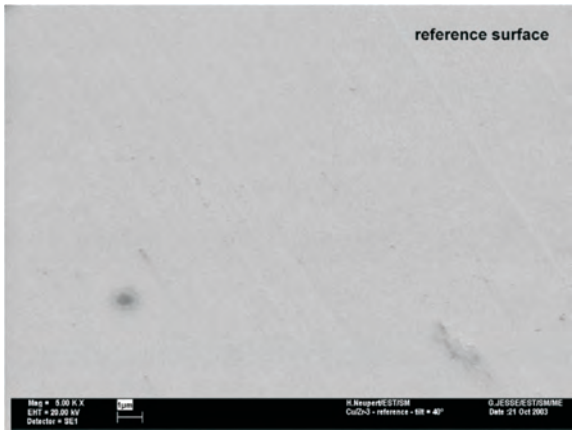

Figure 6.13: SEM image of the reference surface of C15000 laser test specimen.

Similarly, a diamond turned specimen of C15000 before laser irradiation is shown in

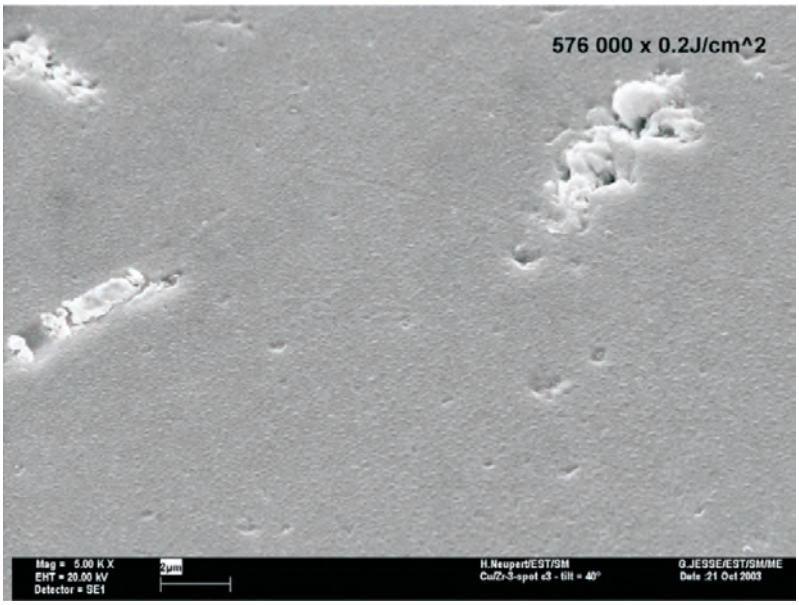

Figure 6.14: SEM image of the C15000 laser test specimen after $5.76 \cdot 10^5$ cycles at 226 MPa cyclic stress amplitude. The damage criteria of Ra 0.02 μm was reached after the taking of this picture at $6 \cdot 10^6$ cycles.

Figure 6.13. The same 226 MPa cyclic stress amplitude as for the C10100 mentioned above was applied and after $5.76 \cdot 10^5$ cycles the surface had still not reached the damage threshold, Figure 6.14, while C10100 was already damaged at $6 \cdot 10^4$. There are some localized damaged zones visible in the figure, but the surface roughness evolution did not reach the damage criteria. The C15000 specimen reached the damage criteria (Ra 0.02 μm) at $6 \cdot 10^6$ cycles, which is two orders of magnitude later than C10100.

Figure 6.15 shows a high stress amplitude (nominally 451 MPa) specimen of C15000 at $6 \cdot 10^3$ cycles, by which time it had reached the damage criteria. The damage features clearly look different than for C10100 in Figure 6.12, but one has to bear in mind that the C10100 reached the damage criteria before the taking of this picture and it was processed further, while the C15000 specimen had just reached the damage criterion.

A summary of the laser fatigue experiments is shown in Table 6.2. A first conclusion that can be made from the results is that the ordering of the materials is the same as for the ultrasound. This consistency indicates that the results are reliable within the error margins. C15000 is the best alloy in the laser experiments followed by C15715 GlidCop® Al-15. C10100 is the last. C15000 was tested in two different temper states: annealed and 40 % cold worked. The same stress amplitude of 338 MPa

Table 6.2: The results of the laser fatigue experiments (cw = cold worked).

UNS Name	Thermal state	Stress amplitude [MPa]	Number of cycles at Ra 0.02 μm
C10100 Cu-OFE	cw 50 %	227	$6 \cdot 10^4$
C15000 CuZr	cw 40 %	451	$6 \cdot 10^3$
C15000 CuZr	cw 40 %	338	$1 \cdot 10^4$
C15000 CuZr	cw 40 %	338	$1.5 \cdot 10^4$
C15000 CuZr	cw 40 %	225	$1 \cdot 10^6$
C15000 CuZr	cw 40 %	169	$1 \cdot 10^7$
C15000 CuZr	annealed	338	$7 \cdot 10^3$
C15715 GlidCop® Al-15	hot extruded	442	$3 \cdot 10^2$
C15715 GlidCop® Al-15	hot extruded	321	$5.7 \cdot 10^4$
C15715 GlidCop® Al-15	hot extruded	214	$1 \cdot 10^5$

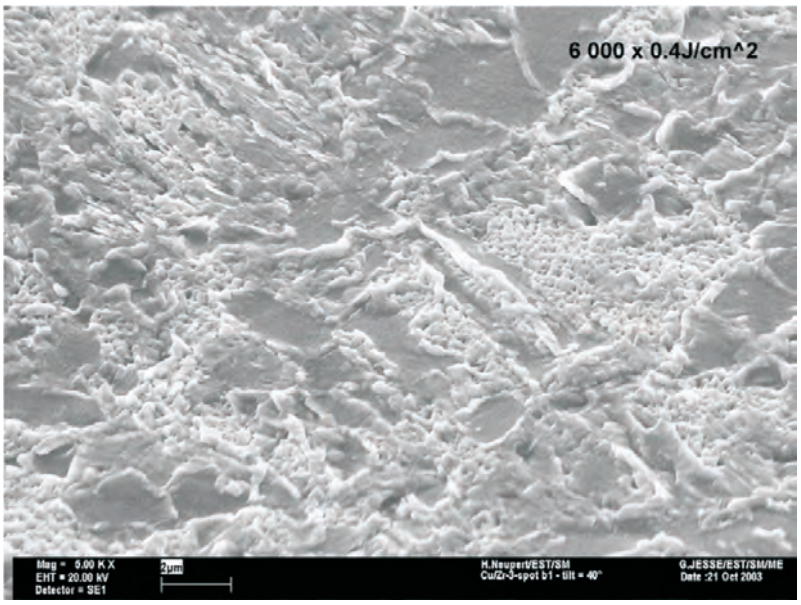

Figure 6.15: SEM image of the C15000 laser fatigue specimen after $6 \cdot 10^3$ cycles at 451 MPa nominal cyclic stress amplitude. The damage criteria of Ra 0.02 μm was reached at this point.

was applied and the number of cycles up to Ra 0.02 μm varied, as shown in the summary Table 6.2: Annealed was lower and 39 % cold worked higher.

6.3 Pulsed radio frequency fatigue experimental results

Compared to ultrasonic and laser fatigue setups, the RF experiments are much more complex, expensive and time consuming. The first specimen was C10100 in a 50 % cold worked state. The same material has also been tested by laser and ultrasound to allow direct comparison. About $2 \cdot 10^6$ cycles were applied with a pulsed temperature rise of 110 $°C$. The temperature rise value has some error margin, due to the difficulties in measuring the input and the reflected power of the cavity. The difference of these two is taken as absorbed power, which heats up the cavity. An error margin of $\pm$ 10 % should be considered for the temperature rise. The 110 $°C$ temperature rise corresponds to a 155 MPa stress amplitude. Optical bright and dark field images of the specimen after processing are shown in Figure 6.16.

Figures 6.17 and 6.18 show SEM images of the fatigued zone on the first C10100 RF fatigue specimen. The images are from the zone, where the magnetic field has its maximum value and the pulsed temperature rise was 110 $°C$. The images clearly show fatigue features which are typical of early stage fatigue failure of copper [34]. There are lots of visible extrusions and opened cracks. The level of damage seem to have significant differences between adjacent grains. There are even grains without visible damage features inside the maximum magnetic field zone. The cracks seem to follow the grain boundaries, especially between grains that have significantly different levels of damages. There are also smaller cracks which seem to be inside the grains starting and ending at the grain boundaries. The cracks inside the grains seem to have the same orientation within a grain. This indicates that the cracks are formed along specific crystal planes within the grain.

The surface roughness of the disc before RF processing was Ra 0.004 μm. After RF fatigue experiment the roughness at the most damaged zone was measured to be Ra 0.15 μm, so it had increased significantly.

The second specimen, also in C10100 and manufactured in the same way by the same supplier, was planned in the following way. As was explained in Chapter 4.4 (Figure 4.15), the normalized magnetic field distribution on the specimen is continuous with relative values from zero to one over a distance of 25.4 mm (one $inch$). Also the normalized pulsed temperature rise (ΔT) and the stress amplitude have a range from zero to one. In the first specimen, where the peak temperature rise was

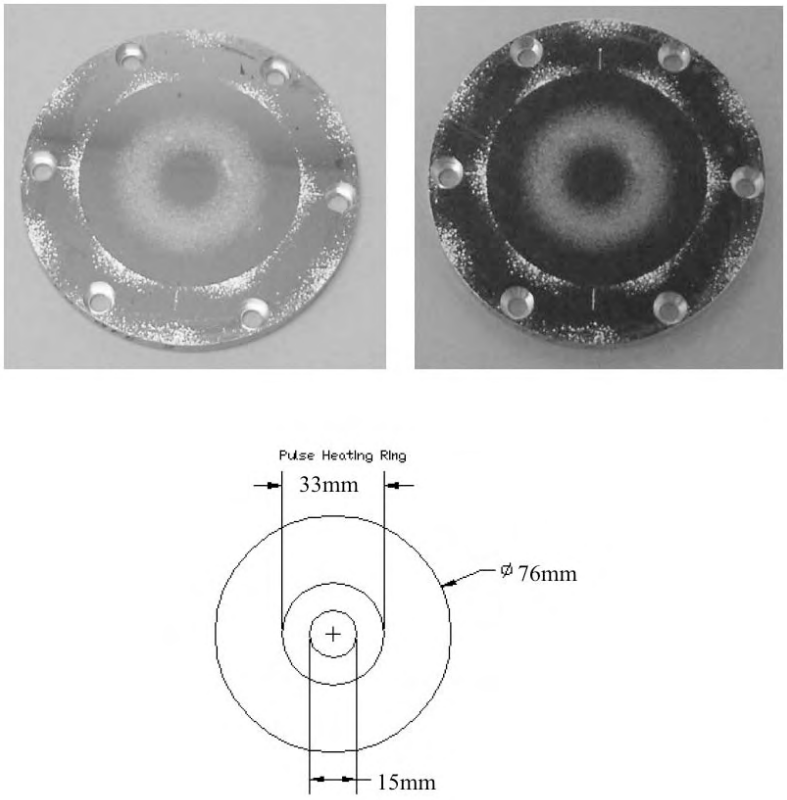

Figure 6.16: Bright and dark field images of the first radio frequency fatigue specimen at SLAC (after processing). The fatigue damage is the inner ring indicated at the bottom drawing. The magnetic field is a ring which has a Gaussian cross section, which is reproduced in the intensity of the damaged zone. Damaged regions closer to the outer diameter and the bolt holes are most likely due to the RF breakdown events, a completely different process, which was observed during the processing of the cavity.

110 $^{\circ}C$, the visual threshold of the fatigue damage was at a radial position where the nominal temperature rise was about 70 $^{\circ}C$, Figure 6.21. So, the power level was set to give a peak temperature rise of 70 $^{\circ}C$, which corresponds to a stress amplitude of 100 MPa. The number of cycles applied was $2 \cdot 10^6$.

Figures 6.19 and 6.20 show scanning electron microscope (SEM) images of the damaged zone of the second C10100 specimen. It can be seen that the results are consistent with the first specimen. The density and dimensions of the fatigue features correspond to the damaged zone's edge on the first specimen, where the pulsed temperature rise was the same as the peak value here (70 $^{\circ}C$).

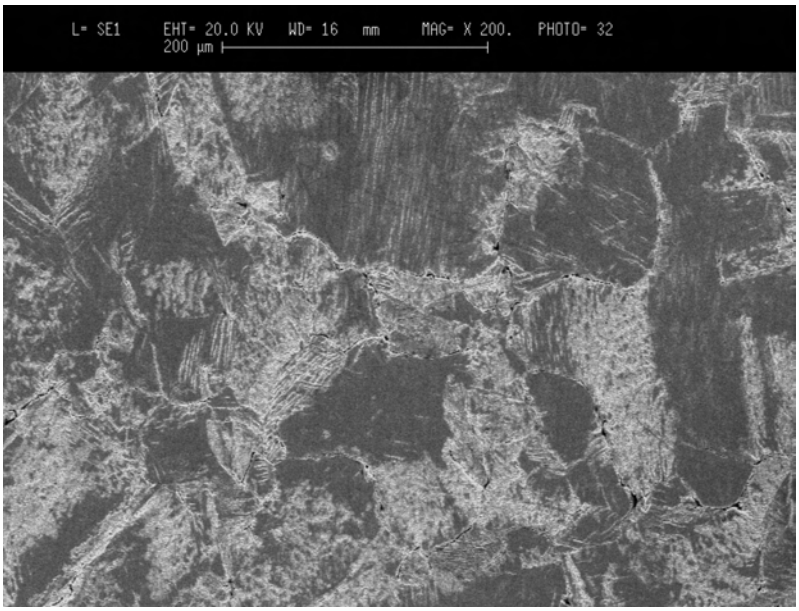

Figure 6.17: SEM image of the fatigued zone of the first C10100 specimen. The image is taken from the maximum magnetic field zone, which is in the middle of the fatigued ring, see Figure 6.16 for the definition of the zone on the specimen.

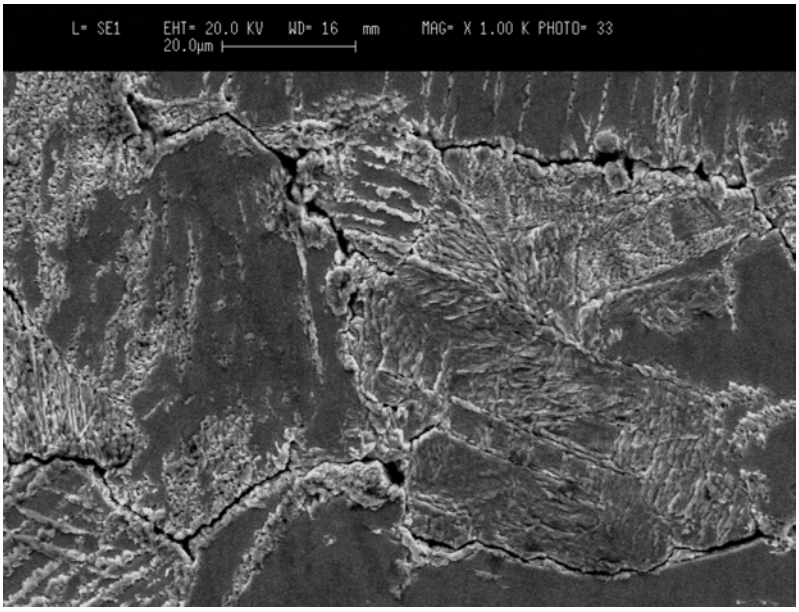

Figure 6.18: Close up SEM image of the zone shown in Figure 6.17.

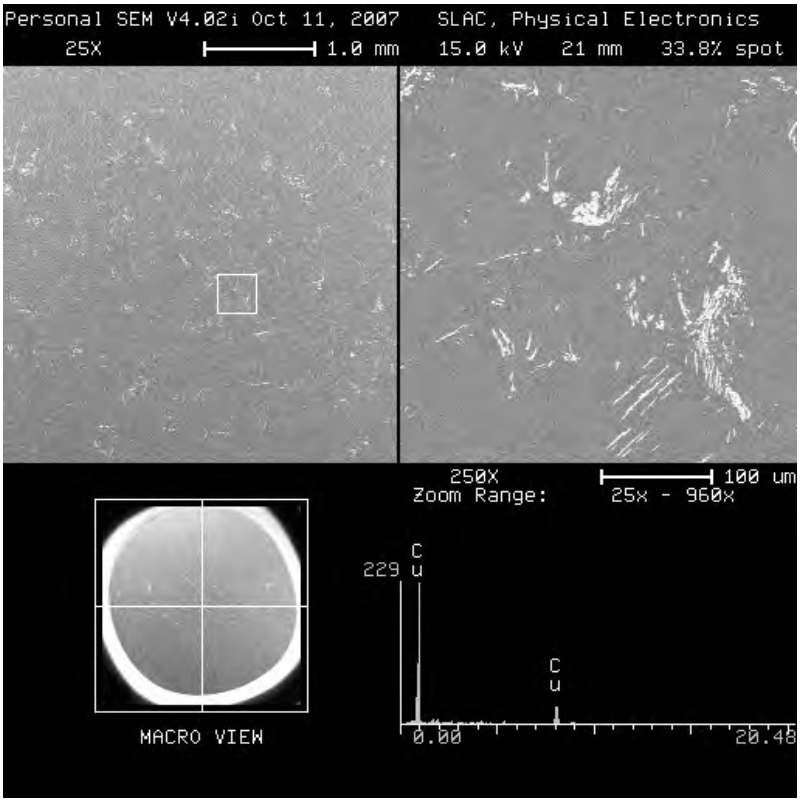

Figure 6.19: A low magnification SEM image of the damaged zone of the second C10100 specimen. The density of the fatigue features is lower than for the first specimen.

The third RF fatigue specimen was C15000 in a hot extruded state. This state is not the optimum for C15000 as the important manufacturing steps of solution heat treatment, quenching, aging and cold working were not applied. The electrical conductivity of the sample was measured to be 82 % IACS. C15000 in the best state has conductivity of 94 % IACS. The Vickers hardness (HV30) for the hot extruded state was measured to be 45, while for 39 % cold worked state it was measured to be 120. The hot extruded C15000 specimen was subject to the same pulsed temperature rise as the cold worked C10100, 70 $^{\circ}C$. After $1 \cdot 10^7$ cycles it showed no surface damage, while the C10100 was damaged at $2 \cdot 10^6$ cycles. The corresponding stress amplitude was 100 MPa.

The fourth RF processed fatigue specimen was also hot extruded C15000. As the third specimen did not show any damage the pulsed temperature rise was increased to 100 $^{\circ}C$. It was run up to $1 \cdot 10^7$ cycles. Figure 6.22 shows the resulting surface damage. The level of the damage is similar to RF processed C10100 in a 50 % cold worked state, which was run $2 \cdot 10^6$ cycles at 70 $^{\circ}C$ pulsed temperature

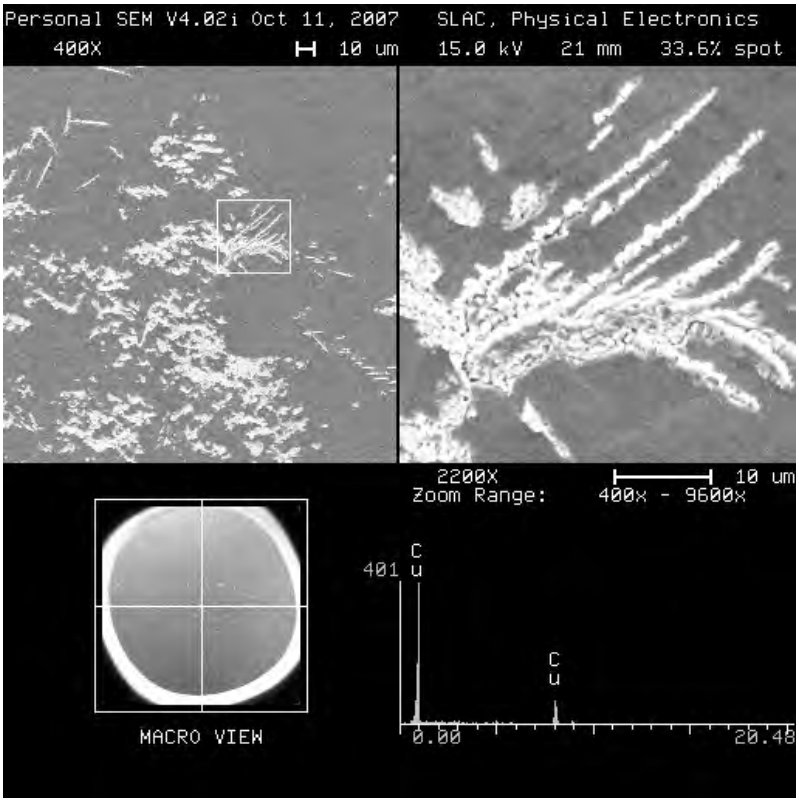

Figure 6.20: A high magnification SEM image of the damaged zone of the second C10100 specimen. The fatigue features are similar to the first specimen, except that the density and the dimensions are lower.

rise, see Figure 6.20.

The fifth specimen was C15000 in 39 % cold worked state. It was processed at a pulsed temperature rise of 110 $^{\circ}C$ up to the same $1 \cdot 10^7$ cycles range. The strength of cold worked 15000 was expected to be higher than hot extruded 15000 based on basic mechanical strength measurements, Table 5.2. Therefore, the pulsed temperature rise was set to slightly higher. The specimen did not show any damage after the run and it is considered as a run-out specimen.

This series of RF experiments were important in showing high consistency with the laser and the ultrasound and gave evidence that copper zirconium C15000 has better fatigue resistance even in a hot extruded state than pure copper C10100 in a cold-worked state. Also the difference in fatigue strengths between cold worked (and age hardened) and hot extruded C15000 was demonstrated.

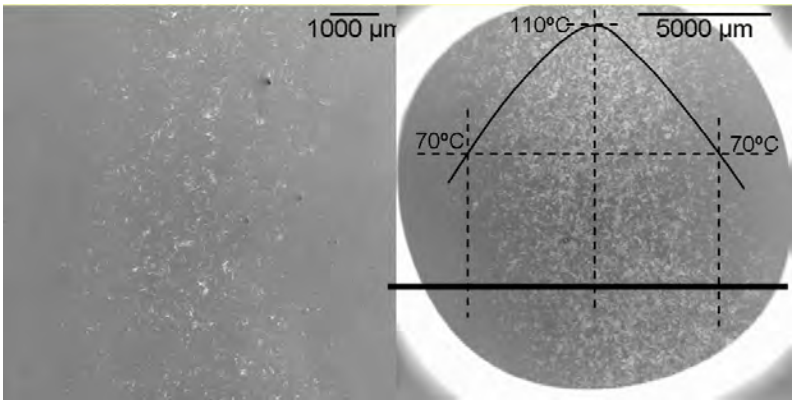

Figure 6.21: Right: a close up SEM image of the damaged zone of the first C10100 specimen after RF processing. As the temperature distribution graph shows the damage threshold seems to be at 70 $°C$ pulsed temperature rise. Left: a close up SEM image of the damaged zone of the second C10100 specimen after processing. The peak pulsed temperature rise was set to 70 $°C$. The achieved density of fatigue features at the same number of cycles ($2 \cdot 10^6$) is consistent with the edge of the damaged zone of the first specimen.

6.4 Compilation of the results of the three experiments

The experimental results from the three types of experiments have been put in a Wöhler plot [12], with the objective to benchmark the experiments and to be able to make predictions for tested materials in the CLIC application. However, the damage criterion was different in the three experiments. In the ultrasonic experiments it was a final fracture, see Chapter 4.2.1 and in the laser experiments the criteria was an increased surface roughness of Ra 0.02 μm, see Chapter 4.3. The aims of the first radio frequency experiments were to demonstrate the performance of the experimental setup at SLAC, establish the validity and benchmark for RF induced fatigue of the collected data, by ultrasonic and laser setups and especially by determining an appropriate damage criterion.

To this date, about 11 laser fatigue specimens were conducted. The ultrasonic setup had a much higher throughput with a total of 104 specimens tested. At SLAC, a total of five RF fatigue specimens were processed.

All the laser and ultrasonic experimental data are presented together in Figures 6.23 and 6.24. Figure 6.23 is the classical form of the Wöhler curve, where the fatigue life is shown as the applied stress amplitude in MPa in function of the number of cycles N. Circles in the figure represent the laser specimens. Diamonds are standard

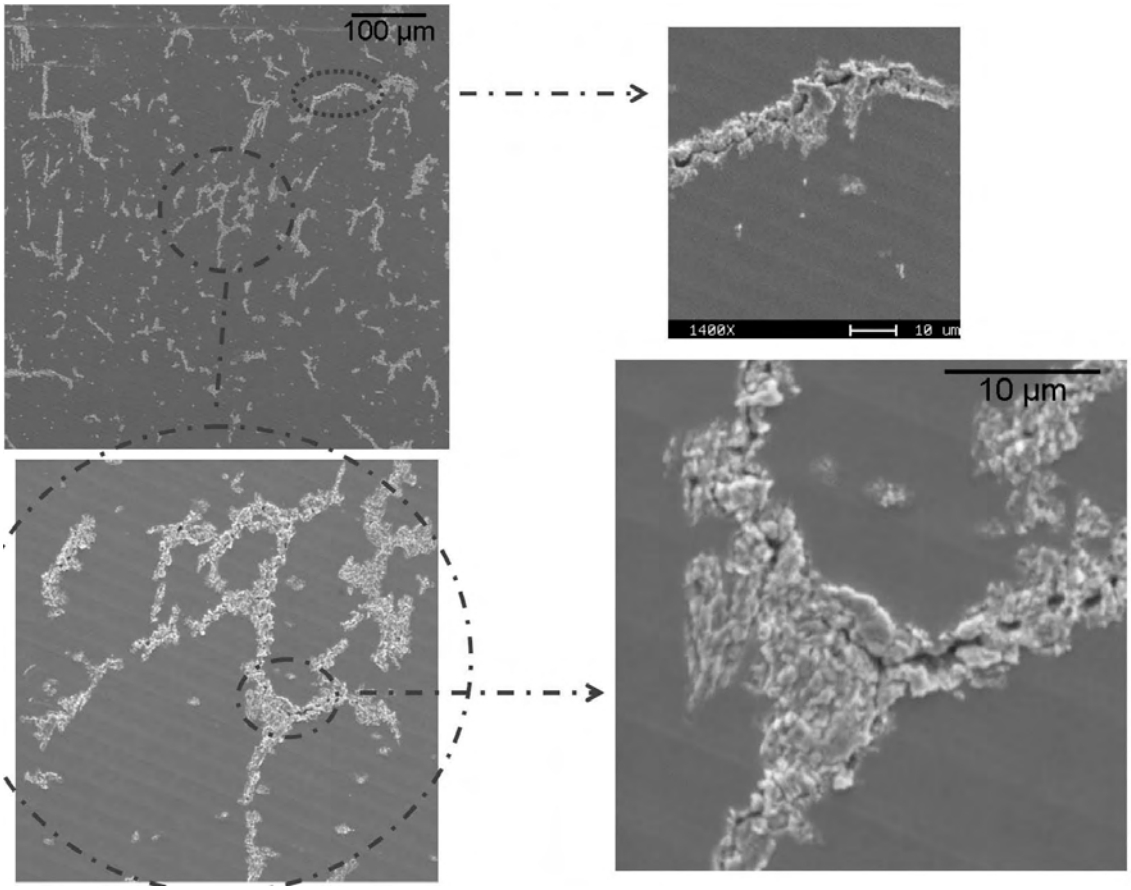

Figure 6.22: A high magnification SEM image of the damaged zone of the fourth RF fatigue specimen in C15000. The level of the damage is similar to RF processed cold worked C10100 at 70 $°C$ after $2 \cdot 10^6$ cycles, Figure 6.20.

ultrasonic specimens. Squares are pre-stressed ultrasound specimens. The triangle is the current CLIC target value for C15000. Different materials are distinguished by colors and lines are the corresponding fitted curves. The right pointing arrow represents a run-out specimen and the left pointing arrow means that the specimen had cracked before the run was terminated, without exact detection of the moment of failure. The data was fitted with a least square best-fit to Equation 6.1 [39]. This is a simplified version of the stress amplitude versus the number of cycles. Since there were no entire life curves, this equation gives a good approximation of when the cycles are above or below the transition value from plastic to elastic dominated strain. The run-out data points are not included in the curve fitting.

$$\Delta\sigma = A(N)^b \tag{6.1}$$

Table 6.3: The best candidate alloys

UNS Name	Thermal state	Fatigue strength [MPa at 10^8]	Fatigue strength [MPa at 10^{10}]
C10100 Cu-OFE	50 % cold worked	120	110
C15000 CuZr	39 % cold worked	200	180
C15715 GlidCop® Al-15	hot extruded	200	160

where

$\Delta\sigma$ = stress amplitude
A and b = material parameters
N = number of cycles

The lowest fatigue strength was measured for C10100, Oxygen-Free Electronic Copper (Cu-OFE) in a half hard state (50 % cold worked). The best copper alloys at 10^8 cycles are C15000 GlidCop® Al-15 and C18150. At UHCF regime the C15000 remains the best alloy. Fatigue strength values of the best copper alloys are shown in Table 6.3.

Figure 6.24 is a modified version of a Wöhler plot adapted to CLIC accelerating structures. Here the vertical axis shows the surface magnetic field, which induces the corresponding stress amplitude. Calculations are based on the equations from (2.1) to (3.1) using the CLIC parameters in June 2007 (accelerating gradient of 100 MV/m, peak input RF power of one structure 65 MW, frequency of 11.944 GHz). The surface magnetic field presented is normalized to the CLIC target value for C15000 (479000 A/m). The symbols in Figure 6.24 have the same meanings as in Figure 6.23. It can be seen that the differences between all the materials diminish when the magnetic field is considered rather than simply the stress amplitude. However, the ordering remains the same and C15000 is still the best material.

The laser experimental setup had a lower throughput than the ultrasound. Based on the data collected, C15000 (CuZr) in an age hardened and 39 % cold worked state is the best material followed by GlidCop® Al-15 and C10100 (Cu-OFE). The laser fatigue data varied between 10^2 and 10^7 cycles. The laser data shows larger scatter than the ultrasound data. The C10100 data contains currently only one point, so

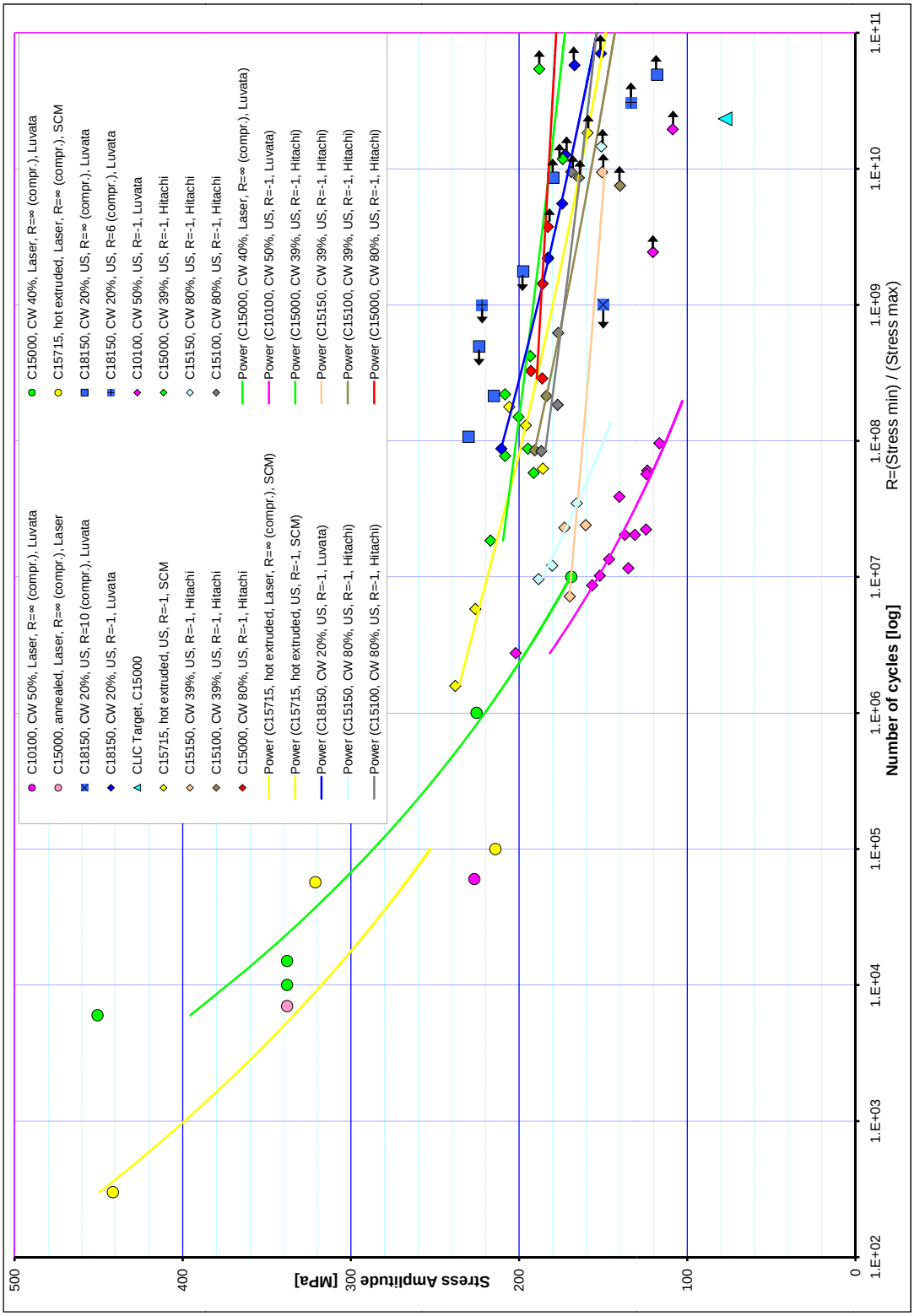

Figure 6.23: Wöhler curves for all the results of the laser and ultrasonic fatigue experiments. See the text for details.

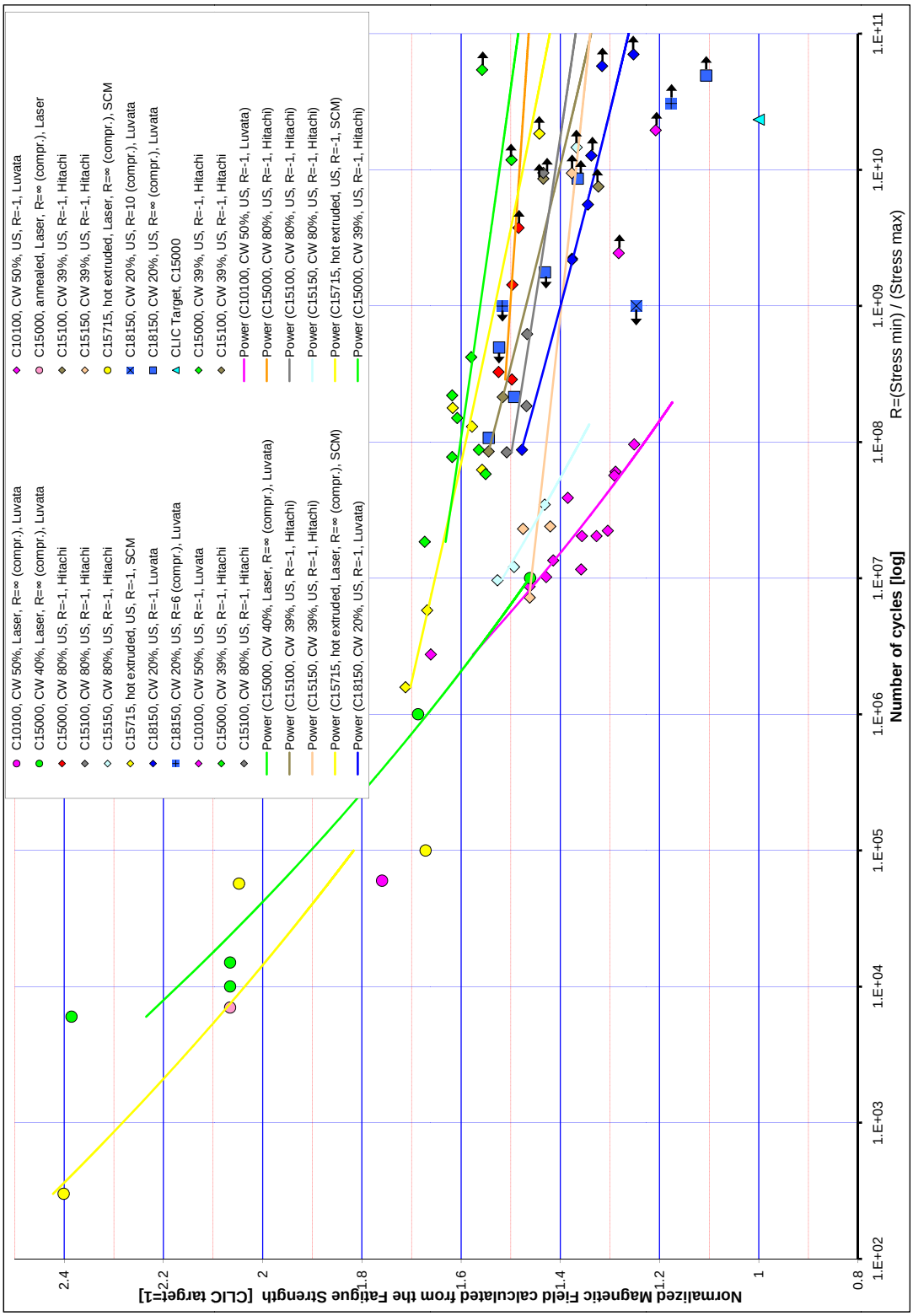

Figure 6.24: The surface magnetic field versus number of cycles to failure Wöhler curves for all the same data as in Figure 6.23. See the text for details.

more laser experiments would improve the quality of the results. The order of the materials for the laser and ultrasonic experimental results are the same. The two materials tested by RF setup have also the same ordering. A general validation of the techniques is thus good.

Figures 6.23 and 6.24 contain all the data, which represents the most complete collection relevant for high-power RF cavity applications to this date.

7 Discussion

In this Chapter the influence of the candidate materials and their preparation techniques on the performance of the CLIC accelerating structures will be discussed based on the results presented in Chapter 6.

7.1 Pure copper C10100 and anisotropic fatigue resistance

For pure copper C10100 the yield, tensile and fatigue strengths for annealed and typical cold worked temper states are shown in Table 7.1. It can be seen that cold working has an improving effect on the yield strength up to a factor of four, but less than 30 % increase in tensile strength. Some experimental fatigue data exists in [70], where fatigue experiments were carried out for cold worked and annealed pure copper. The results suggest about 33 % higher fatigue strength for a cold worked state than for an annealed state. Work hardening occurs usually when making tensile and fatigue tests, except for fatigue of cold worked copper at high temperatures or low cycle fatigue tests where softening occurs. For pure copper, the electrical conductivity does not change significantly between different thermal states. By using the results obtained by RF and laser fatigue experiments and using the ultrasonic data to extrapolate it to CLIC lifetime, it seems that pure copper cannot meet the CLIC target values in cold worked or in annealed states.

Table 7.1: Tensile and fatigue properties of pure copper C10100 in annealed and cold worked states.

State	Yield strength $[MPa]$	Tensile strength $[MPa]$	Fatigue strength at 10^8 $[MPa]$	Fatigue strength at 10^{10} $[MPa]$
Annealed	49	216	70 [70]	-
Cold worked	313	323	120	110

The SEM images of the cold worked copper sample fatigued by RF (Figures 6.17 and 6.18) clearly indicate differences in the fatigue resistance between different grains. This is most likely due to different crystallographic orientations. A similar effect was observed in [42] studies of thermal fatigue in thin copper films. Grains having a (111) orientation showed damage at an earlier stage than the grains having an orientation (100). The two grain orientations experience different stresses and different active slip systems under the biaxial stress state. A SEM inspection of the damaged zone

of the RF fatigue sample in copper also showed that the crack formation seems to prefer systematically boundaries between grains having a high difference in the level of fatigue damage. Similar effects are suggested and explained by Creteny and Saxena [34] and Suresh [26]. Cracks prefer boundaries between highly misoriented grains. This crystal orientation dependent fatigue resistance was observed late in the study and due to time constraints it was not studied further. It is clear that such anisotropy exists for copper. Indeed, the mismatch in the deformation of adjacent grains seems to be the driving force for initiating intergranular cracks. However, it might be tricky to benefit from the anisotropy information in the CLIC accelerating structures, which are based on three dimensional geometry.

The study of high cycle thermal fatigue in thin copper films [42] suggested a threshold pulsed temperature rise of roughly a factor of two, higher (damage at pulsed temperature rise of $100°C$ after $3 \cdot 10^9$ cycles) for copper than what was concluded in this study ($48°C$ after $2.33 \cdot 10^{10}$ cycles). Both are extrapolated data. The properties of thin films are different for bulk materials and it is suggested by several authors that thin films result in a higher strength, which is consistent. In the thin films study, the compressive stress was due to a thermal expansion mismatch between the film and the substrate and in the laser and RF experiments it was due to a temperature gradient in the bulk.

The high cycle fatigue results for pure copper [28] are quite consistent with the results obtained in this study. A fatigue strength of 92.2 MPa at 10^{10} cycles was suggested for annealed copper. The ultrasonic experiments conducted in this study suggested a fatigue strength of 110 MPa at $2.33 \cdot 10^{10}$ cycles for cold worked copper. Therefore, these two studies suggest a 20 % higher fatigue strength for cold worked than annealed copper. This is not far from the above mentioned 33 % in [70], which does not specify the level of cold working and the test conditions precisely.

All the fatigue experiments conducted for all the materials in this study show a descending fatigue strength when the number of cycles is increased, which indicates that no fatigue limit exists in the number of cycles range concerned.

7.2 Precipitation hardenable alloys C15000, C15100, C15150 and C18150 and surface roughening at UHCF range

Based on the ultrasonic fatigue experimental results, an increase of 30 % in CLIC performance can be achieved by using C15000 instead of pure copper C10100 if a cold worked state can be used for the structures. Currently, three data points, one with a laser and two with RF, exist for C15000 in an annealed or hot extruded

state. A hot extruded state is considered to be close to an annealed state. The basic mechanical properties between annealed and hot extruded states are similar, Table 5.2. Soft material states turned out to be impossible to test with the ultrasonic setup, most likely due to a high damping (internal friction) of the annealed state.

C15000 was tested in hot extruded and cold worked stated by the RF setup and the latter resulted in a significantly higher performance. This confirms a beneficial effect of the optimum precipitation hardening treatment, which was expected and suggested by basic mechanical characterization Tables 5.2 and Tables 7.2.

Table 7.2: Tensile and fatigue properties of copper zirconium C15000 in annealed and cold worked states.

State	Yield strength $[MPa]$	Tensile strength $[MPa]$	Fatigue strength at 10^8 $[MPa]$	Fatigue strength at 10^{10} $[MPa]$
Annealed	59	208	-	-
Cold worked 39 %	370	323	200	180
Cold worked 80 %	428	386	190	180

At a higher cold working rate, 80 %, copper zirconium alloys actually showed no higher fatigue strength in this study within the experimental error margins than 39 % cold worked copper zirconium alloys, see Chapter 6.1.4. The increased tensile and yield strength values - when moving from 39 % to higher cold working ratios can be seen in the Table 7.2. The cold working dependence on the tensile strength is stronger for C15000 than for pure copper. For better understanding and completeness it would be interesting to do mechanical fatigue experiments for copper zirconium alloy in an annealed state. It can thus be concluded that the use of C15000 in the CLIC accelerating structures is most profitable when a reasonable cold working ratio could be maintained, and the gain in accelerating gradient in this case would be of about 30 % compared to cold worked copper and of about 65 % compared to annealed copper.

As we have seen, the tempering process has a big influence on the strength of copper zirconium, but the electrical conductivity is also affected. For C15000 in a hot extruded state, where no quenching, aging and cold workings were applied, the electrical conductivity was measured to be about 82 % IACS, while the best conductivity values for optimum conditions were about 93 % IACS. The losses in electrical conductivity and in strength are both due to the incorrect precipitation forming, done without precise thermal and mechanical treatments (aging and cold

working). Thus, for the precipitation hardenable alloys it is the proper combination of the aging and cold working which is important. The RF experimental results show that hot extruded C15000 is still better than cold worked C10100. Therefore, even the use of C15000 in annealed state is advantageous for CLIC accelerating structures. Cold worked C15000 showed the best performance in the RF experiments.

It has been proposed [46] that based on low cycle thermal fatigue experiments made at temperatures close to room temperature, C15000 was the best candidate among similar alloys.

Other grades of precipitation hardenable copper zirconium alloys were also studied. The C15100 and C15150 are based on the same principle as the C15000, but have lower zirconium contents. This results in a higher electrical conductivity - 94 and 97 % IACS - respectively. These low zirconium content alloys were measured to have lower fatigue strengths by the ultrasonic setup, and the combination of these two parameters gives a lower accelerating gradient. C15000 remains the most competent of the copper zirconium precipitation hardenable alloys. See Figure 6.5 for the comparison of the copper zirconium alloys. C15100 or C15150 could be interesting candidates for a lower gradient option of CLIC, where they would give slightly higher overall machine efficiency than C15000, due to higher electrical conductivities.

Another precipitation hardened copper alloy tested was C18150, copper chromium zirconium [71]. Its properties are achieved in the same way as C15000 copper zirconium. Mechanical properties of annealed and cold worked C18150 are presented in Table 7.3. The electrical conductivity of cold worked and aged C18150 was measured to be about 80 % IACS. The thermal conductivity has the same relative difference to pure copper and this results in a lower performance than C15000 in the accelerating cavity application, as it can be seen from the magnetic field versus the number of cycles graphs in the Figure 6.24. Since no further advantages are related to the use of C18150 instead of C15000, the latter remains the preferred candidate among the precipitation hardenable copper alloys.

Table 7.3: Tensile and fatigue properties of CuCrZr C18150 in annealed and cold worked states.

State	Yield strength $[MPa]$	Tensile strength $[MPa]$	Fatigue strength at 10^8 $[MPa]$	Fatigue strength at 10^{10} $[MPa]$
Annealed	97	310	-	-
Cold worked	386	393	210	170

The results presented in Chapter 6.1.5 show a surface roughness that develops dur-

ing the cyclic loading at an ultra high number of cycles range, before the fatigue crack nucleation. This was observed for all the alloys tested and studied in detail for precipitation hardened C15000 and C18150. It has been shown [27] that cyclic loads around 10^8 - 10^{10} cycles can lead to a formation of a local surface texture on copper. The development of local surface roughness can be a critical issue for the CLIC accelerating structures, because in order to be able to operate, they require high surface quality. Ultrasonic experiments for 20 % cold worked C18150 suggested that a threshold for the surface roughening at $7.04 \cdot 10^{10}$ cycles would be 10 % less (151 MPa) than the fatigue strength (167 MPa) at the same cycles range ($5.78 \cdot 10^{10}$). A threshold for surface roughening for annealed pure copper at 10^{10} cycles was suggested to be 63 MPa which is about 30 % less than the fatigue strength obtained at the same cycles (92.2 MPa) [28]. Annealed copper and cold worked copper chromium zirconium are not directly comparable but the order of magnitudes of the ratios are relatively close, 10 % versus 30 %. The surface properties between these two experiments are different. C18150 was diamond turned and annealed copper was machined.

Experiments for identical specimens manufactured in C15000 by different techniques showed that the surface properties have a big influence on the roughening phenomena. Specimens that were diamond turned by a high quality lathe showed no appeared surface roughness, while others that were diamond turned by a conventional machine did show roughness development. It can be concluded that the bulk fatigue behavior is independent of the appearance of roughening, because the crack occurs at the same time for these two sets of sonotrodes and the increased surface roughness is not always the origin of the fatigue crack. Due to time constraints, this fabrication issue was not studied further and it is not understood what actually makes the difference.

The plastic deformation which was part of the strain amplitudes was not quantified. However, it was observed that qualitatively the plastic deformation on pure copper was higher than that on strengthened coppers. This was concluded from the heat generation during cycling. Same amplitude cycles on pure copper required significantly more effective cooling than on strengthened copper in order to keep the average temperature at the same level. A smaller plastic strain component of strengthened material indicates a different dislocation arrangement and clearly contributes to the higher fatigue strength of the alloyed coppers. An example method to quantify the plastic deformation in ultrasonic fatigue testing is presented in [30]. A difference in heat generation was not observed between 39 % and 80 % cold worked CuZr alloys. The fatigue strengths between different cold working ratios showed no differences which means that probably, the difference cannot be seen at small strain amplitudes. Amplitudes that exceed significantly the yield strength would be needed to activate the dislocations in order to show different heat generations and, thus, plastic deformations.

Similar behavior of crack path morphology in high purity (99.99 %) ultra fine grained coppers [32] was observed. Below 10^8 cycles, the crack followed a straight path, while above 10^8 it was torturous. This was observed systematically on precipitation hardened CuZr alloys. This would probably indicate moving from a transgranular fracture mode to an intergranular when increasing the number of cycles, as the crack seems to follow a crystallographic and deflected path. Commercial purity UFG coppers did not show crack path deflection at high numbers of cycles [32]. It is unknown why this occurred on alloyed copper and due to its presumably low importance for this study, it was not studied further.

7.3 Compressive mean stress effects

Experiments up to UHCF regime on precipitation hardenable C18150 (CuCrZr) with compressive mean stress did not result in differences in fatigue strength compared to zero mean stress, Chapter 6.1.1. The relaxation of the static compressive prestress can be excluded because a fully compressive condition was crucial for the operation of the special specimen. This means that the static prestress was always higher than the cyclic stress amplitude. The cyclic stress amplitude was constant during the experiment.

Creep-fatigue studies on CuCrZr suggest a 6-12 % drop on peak tensile stress [25] during hold time. The decrease is relatively small and supports the fact that the stress cycle here was fully compressive from start to finish. The yield strength of 386 MPa and the tensile strength of 393 MPa (Table 5.2) were exceeded for most of the compressive mean stress experiments. The compressive yield strength was not measured, but nevertheless, it seems that compressive stresses are not detrimental for the fatigue of CuCrZr.

This result is in agreement with fatigue experiments performed for prestrained oxygen-free copper [22]. Tensile mean strain reduced the fatigue life and when the mean strain was increased the fatigue life was further reduced. The tensile mean stress vanished almost completely prior to rupture. For copper, the tensile mean stresses were found to be detrimental because they support crack initiation and propagation.

7.4 Dispersion strengthened alloy C15715 and crack propagation rate

If cold working and age hardening cannot be preserved in the fabrication process of the CLIC accelerating structures, or if post manufacturing high temperature cycles are required for the RF breakdown resistance, then the best candidate is the dispersion strengthened alloy C15715 GlidCop® Al-15. Its mechanical properties are weakly influenced by thermal treatments. The material used in ultrasonic and laser experiments was already in a non-cold worked state and resulted in fatigue strength only slightly less than cold worked C15000, Table 7.4

Table 7.4: Tensile and fatigue properties of C15715 GlidCop® Al-15 in annealed and cold worked states.

State	Yield strength $[MPa]$	Tensile strength $[MPa]$	Fatigue strength at 10^8 $[MPa]$	Fatigue strength at 10^{10} $[MPa]$
Annealed	318	339	200	165

There are some disadvantages however for GlidCop® such as a lower fracture toughness and worse machinability. Chapter 6.1.2 contains results showing a higher crack propagation rate for C15715 than for any other alloy tested. A higher crack propagation rate may be a result of a composite-like micro-structure, where alumina particles can de-bond from the copper matrix and create voids. This makes the material's fatigue behavior brittle and result in fast crack propagation. In case of precipitation hardened copper alloys the bond between the matrix and the intermetallic precipitates is strong and often the matrix and precipitates may have the same crystal lattice within a grain and de-bonding of these is less likely to happen.

A similar observation was discussed for ITER first wall and divertor structures [19], where the high crack propagation rate of GlidCop® was decisive and was therefore rejected. Precipitation hardened C18150 was selected instead due to its more optimum combination of strength and ductility.

The crack propagation could become an important parameter for the CLIC accelerating structures if the formation of small fatigue micro-cracks could be accepted. This would be worth studying due to the fact that there is no known experimental evidence that the micro-cracks or the surface roughness actually do disturb the operation of normal conducting accelerating cavities. The surface currents induced by electromagnetic waves seem to flow through the micro-cracks and the developed roughness, even though it was expected to cause a malfunction already at the early

stage of fatigue. Since the heated layer and thus the layer affected by the compressive stress is thin, of the order of 20 μm, it is possible that the cracks become dormant after penetrating into the zero stress zone of the bulk. If they became dormant before the cavity operation was disturbed, for example that the crack dimensions are small enough that they act as short circuits which do not affect the surface resistance [48], it would revolutionize the material possibilities. For example, even annealed pure copper could be used at high gradients.

A clear disadvantage of the C15715 compared to pure copper and precipitation hardened alloys is its more difficult machinability. The hard ceramic materials are generally difficult to machine by themselves. In this case, the hard sub-micron aluminum oxide particles inside the softer copper matrix make the machining process difficult by acting as an abrasive, increasing the tool wear and disturbing the cutting processes. They also affect the achievable surface quality, which is a high requirement in the CLIC structures.

The presence of the dielectric particles also raises questions about an influence on RF breakdown characteristics because dielectric particles are known to initiate field emissions [72]. There are two contradictory experimental results for GlidCop®. Experiments conducted at CERN on a DC spark experimental setup [73] suggest a similar DC breakdown resistance for C10100, C15000 and C15715 [74]. Experiments conducted at SLAC (Stanford Linear Accelerator Center, USA) on an RF 11.424 GHz cavity suggest much lower resistance for C15725 GlidCop® Al-25 against RF breakdown than for C10100 [75]. C15725 is a similar alloy to C15715, but with a slightly higher aluminum oxide content (0.25 % compared to 0.15 %, respectively). This RF breakdown consideration could be dominant in rejecting C15715 from the list of the candidate alloys if the SLAC observations turn out to be the right ones. The SLAC samples were etched before the experiment, so the ceramic particles sticked out from the surface due to an uneven attack by the etchant. This could enhance the formation of breakdowns compared to smooth surfaces.

7.5 The effects of the preparation and the manufacturing techniques

7.5.1 Machining

From the fatigue point of view the manufacturing techniques, diamond turning and high speed CNC milling seem to have the same critical issues: the machinability of the material may be decisive in the selection process, especially for mass production considerations. Indeed, the final CLIC machine will require hundreds of thousands

of accelerating structures. Whether each of them consists of fifty discs or four quadrants, it does not change the basic fact that the precision machining of such a production series is a challenge and where the tool wear is one of the most critical issues. The three dimensional features of geometry currently limit the tool size to a maximum of the order of 4 mm in diameter.

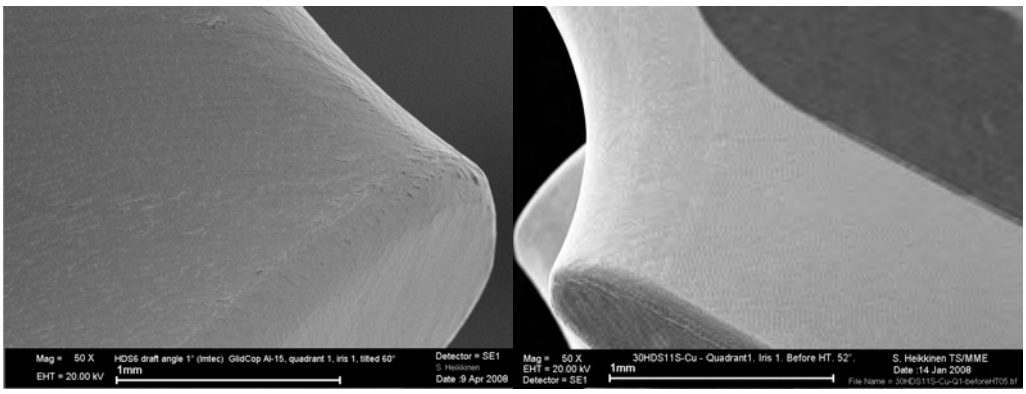

Figure 7.1: CNC milled CLIC prototype pieces in C15715 GlidCop® Al-15 (left) and in C10100 pure copper (right).

Pure copper C10100 and copper zirconium C15000 basically have the same machinability (20 out of 100, where 100 is for free cutting brass). The machinability figure for C15715 GlidCop® Al-15 is not tabulated, but the test millings conducted show that the machinability is slightly worse. The reasons for the machinability decrease are the hard alumina particles in the copper matrix (hardness of alumina is of an order of magnitude higher than for copper). Figure 7.1 shows two examples of high speed milled surfaces in C10100 and C15715, where C15715 resulted in a worse surface quality (C15715 Ra 0.4 μm, C10100 Ra 0.1 μm), but in a similar accuracy ($\pm$ 0.003 mm, Veeco optical profiler).

The zirconium precipitates do not seem to affect the machinability of copper and thus copper zirconium alloys seem to be as easy to machine as pure copper. This was shown by conducted machining tests which resulted in similar accuracies and surface qualities.

7.5.2 Joining techniques

The main joining technique used for accelerator components, vacuum brazing, leads to high temperature cycles, typically fro a few minutes at 800°C - 1000°C. The elevated temperature effects for our candidate alloys were discussed in Chapter 5.1.

In brief terms, this would basically mean that C15000 would lose some of its strength and electrical conductivity. Pure copper C10100 would also lose some of its strength. The strength of C15715 would be less affected.

The vacuum brazing of alumina dispersion strengthened GlidCop® is not straightforward, because the alumina particles easily segregate in the joint and limit its strength. However, it has been demonstrated [76] that by optimizing the parameters it is possible to make sound vacuum brazed joints: GlidCop® / GlidCop® and GlidCop® / stainless steel. The pull strength of the joint was measured to be about 415 MPa, where the strength of the base material was 450 MPa. From the fatigue point of view, the use of GlidCop® is preferred if the CLIC structures have to be brazed.

Other possible assembly methods could be electron beam welding and clamping. Basically, these two methods do not require elevated temperatures at any step of the process and thus do not limit the material selection and the fatigue performance of the accelerating structures. The weldability issues do not reject any alloy from the list of candidates.

The components of an accelerator machine which have ultra high vacuum volumes inside require a bake out treatment to remove water from the system, see Chapter 1.4. Typically this means a day or two at 150 - 300 $°C$. The upper end of this range may decrease the strength of C15000 and C10100. A test which demonstrates how bake out temperatures affect the fatigue strength of candidate alloys with full testing applied, should be made. The surface and thermal treatments done in order to enhance the RF breakdown resistance of the accelerating structures, described in [11], might also affect the fatigue performance of the candidate alloys.

7.6 Combination of the results obtained by the three experimental techniques

One major issue of the fatigue study is relating the results obtained by different experimental methods with each other. The ultimate goal is to make a quantitative prediction of performance and lifetime for CLIC. It was mentioned already in the beginning that a complete experimental run with CLIC parameters under real environment is not possible. The fatigue experiments with a radio frequency setup, where operating conditions were identical to the CLIC environment, except for the pulse length used, was the closest to the real case. A comparison between the different techniques is shown in Table 7.5. The required number of cycles, $2.33 \cdot 10^{10}$, is achievable only by the ultrasonic apparatus. The pulsed laser and the radio

frequency setups can reasonably reach about 10^7 cycles. The lower limit of the ultrasound is about 10^6, but for most of the cases here, the fatigue data starts at 10^7 cycles. How the three techniques overlap is shown by block diagrams in Figure 7.2. Unfortunately, the techniques overlap just where the fatigue curves seem to have a kink between low cycle and high cycle regimes and where the LCF and HCF mechanisms compete.

Table 7.5: Pros and cons of the experimental techniques.

Technique	Number of cycles	Energy deposit	Pulse length	high throughput
Ultrasound	++	-	-	++
Laser	-	+	++	+
RF	-	++	-	-

Figure 7.2 shows a selected set of Wöhler curves. The idea in the graph is to directly compare the collected fatigue data of the same materials but based on different experimental techniques. The data contains cold worked C10100 (pure copper) using all three methods; cold worked C15000 (copper zirconium) using ultrasound, laser and RF; hot extruded C15000 by laser and RF; C15715 (GlidCop® Al-15) by ultrasound and laser.

It can be seen that the ranking of the materials is the same for all three techniques. For C15000 and C15715 the failure for laser has occurred at stress amplitudes significantly lower than for the ultrasound. Although the laser data for C10100 contains only one point, if one assumes the same slope as for the other alloys, the difference in stress amplitudes is roughly the same. The offset of the two lines could be explained by the difference in the failure criteria. It was mentioned in Chapter 4.3 that the criteria for the laser experiments was set to surface roughness reaching a value of Ra 0.02 μm. The failure criteria for the ultrasonic experiments was explained in Chapter 4.1 and corresponds to when the specimen has a fatigue crack of about 2 mm deep perpendicular to the direction of the loading. It is clear that for a given stress amplitude the laser criteria will be exceeded earlier than the ultrasound criteria. The laser runs were not yet continued beyond the set failure criteria in order to see the crack initiation and the development, but the results are consistent, considering a fixed offset.

One of the objectives of the RF experiments was to establish the damage criterion. Essentially, the criteria should be the point when the surface damage starts to disturb the surface currents at the cavity walls by increasing the surface electrical resistance. This can be monitored online by electro-magnetic quality factor (Q) measurements. The quality factor is a measure of the losses per cycle of the cavity

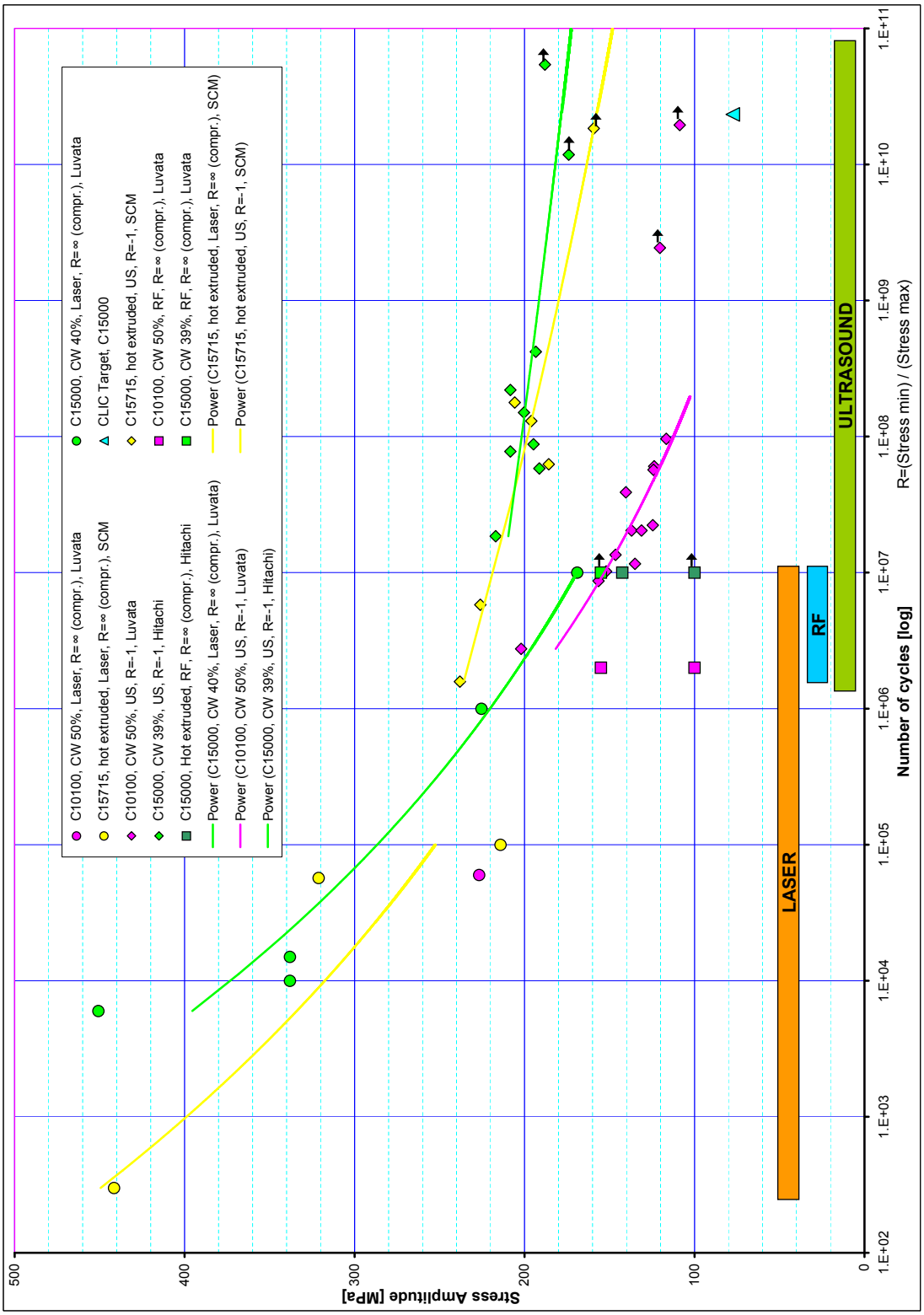

Figure 7.2: Wöhler curves of selected experimental results including the four data points from radio frequency fatigue experiments. Diamonds are ultrasonic, circles are laser and squares are RF fatigue experimental results. Different materials are marked in different colors. Solid lines are fitted curves of a data set with same color.

to external excitation [47]. The quality factor can be determined by measuring the free decay of the reflected electromagnetic oscillation after the RF pulse, see Figure 7.3. The surface resistance is proportional to the damping of this free decay and thus to the quality factor of the cavity [47]. The initial idea of the experiment was to define the threshold corresponding to when the initial value (Q = 44000) starts to degrade. During the five runs performed, no change was observed. This was a surprising result given the visual appearance of the damage. More complete characterization of the crack shape is needed in the future in order to proceed in defining the failure criterion and the influence of the damage on surface currents.

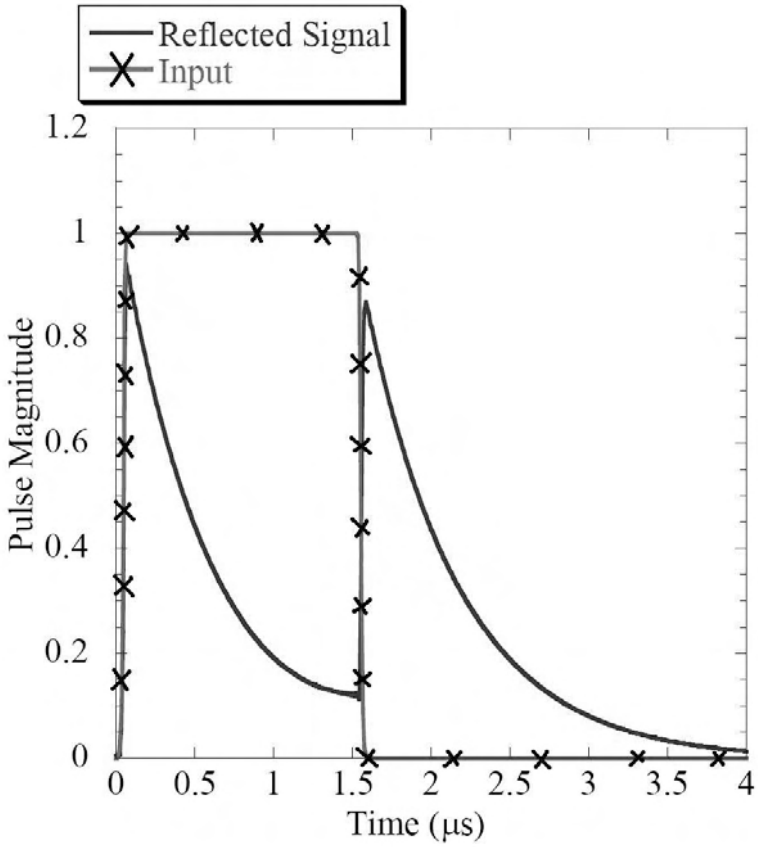

Figure 7.3: Measured forward and reflected signals of the RF fatigue setup. The electromagnetic quality factor can be defined from the free decay of the reflected signal. The absorbed energy which heats up the cavity wall is the forward signal subtracted by the reflected signal [60].

A second way that the fatigue damage can affect the performance of high gradient accelerating structures is an enhanced RF breakdown rate. This may provide another damage criterion. This was not observed experimentally yet because the electric and magnetic fields are separated in the special cavity used. However, in a

typical accelerating cavity these fields overlap. There is therefore a concern that because the extrusions of the fatigued surface enhance the peak surface electric fields, the damage would induce more RF breakdowns in the cavity. The RF breakdown probability increases with the increase of the accelerating gradient and, thus, the surface electric field [73] [74]. The current limit for the breakdown rate of CLIC accelerating structures is 10^{-7} [77], which means that every ten millionth RF pulse is allowed to induce a RF breakdown event.

The stress amplitude of the first radio frequency fatigue specimen in cold worked C10100 corresponds to a pulsed temperature rise of 110 $°C$ and a stress amplitude of 155 MPa. This is consistent with the curve from ultrasonic fatigue experiments of the same material, Figure 7.2. The fatigue damage on this specimen, Figures 6.17 and 6.18, consists of opened cracks along the grain boundaries and within the grains. From this respect, the damage is similar to the ultrasonic induced fatigue, where opened cracks were also detected to roughly have the same width. This is consistent with the fact that the measured average surface roughness of the damaged zone of the RF specimen was Ra 0.15 μm (initially Ra 0.004 μm), which is significantly higher than the average roughness Ra 0.02 μm of the damaged zone of the laser fatigue specimens conducted.

On the other hand, the second RF fatigue specimen with pulsed temperature rise of 70 $°C$ and a corresponding stress amplitude of 100 MPa has much less severe fatigue damage. Figures 6.19 and 6.20 barely show opened cracks. This is closer to the fatigue damage induced by the laser. The laser data of C10100 contains only one point. But if one uses a slope from the other materials tested by the laser and extrapolates from the one C10100 data point, Figure 7.2, we notice that this curve would also fit the second radio frequency data point.

The third and fourth RF fatigue data points (C15000, hot extruded, 70 $°C$, $1 \cdot 10^7$, run-out) (C15000, hot extruded, 100 $°C$, $1 \cdot 10^7$) show that C15000 in a hot extruded state is better than C10100. The same result was also obtained by laser.

The fifth RF fatigue specimen (C15000, cold worked, 110 $°C$, $1 \cdot 10^7$, run-out) resulted in the best performance among the RF tests. This concludes that a similar offset between cold worked C15000 and cold worked C10100 was obtained in all three experiments.

The loading frequency has an influence on the fatigue strength of copper, at least from low to high cycle range [78]. Although the nominal frequency of the three experiments is different, the strain rate is of the same order of magnitude, due to a similar effective frequency, see Chapter 3. However, one would expect a relatively small increase in fatigue strengths when extrapolating the effective frequency

from the 24 kHz to 160 kHz range, of the order of a few percent. The 160 kHz corresponds to continuous cycling with the stress cycle length of the accelerating structures (600 ns). Moreover it was said that the frequency does not affect the HCF and UHCF properties of copper alloys, see Chapter 2.1, [31] and [79]. Therefore, in a similar way, the frequency should not contribute to the differences between the results obtained by the different techniques.

Cyclic loading due to constant thermal pulses (induced by laser and rf) in a constrained region of a structure can be considered as strain controlled. Ultrasonic experiments were also strain controlled. Under strain controlled tests the stress amplitudes have a tendency to increase at small strain amplitudes and decrease at large strain amplitudes. This occurs due to cyclic hardening and softening, respectively. The overlap between the low cycle and high cycle experiments should be sufficient to connect the results without the effect of above mentioned differences. Due to limitations in the experimental techniques, the overlap achieved in this study cannot be extended by using the same experimental setups. The lower limit for ultrasound is approximately 10^6 and the upper limit for laser and RF is about 10^7.

CuCrZr with compressive mean stress showed no different results from fully reversed stress conditions by ultrasound, Chapter 6.1.1. The mean stresses in the thermal fatigue experiments were also fully compressive. This discovery enhances the suitability of the mechanical ultrasonic fatigue data in CLIC life prediction. The average temperature in the three tests was approximately the same, so different temperatures should not contribute to any inconsistency.

The ultrasound specimens experienced uniaxial stresses while in the laser and RF specimens the stress state was an equi-biaxial plane stress. Since the geometries of the specimens were a simple flat disc and straight cylinder and the stresses were uni- or biaxial, the stress state was not considered to contribute a large difference in the results. In the comparison analysis, the Von Mises criteria has been considered in the results for all the cases as an equivalent stress. Von Mises criteria is known to be suitable for ductile materials and used in order to compare multiaxial stress states.

It is the first time that such a comparison, as discussed above, about the quantitative relationship between the radio frequency, laser and ultrasound fatigue experiments performed, has been made. In addition, it shows an important consistency. Also, other researchers have agreed on thermal and mechanical fatigue experiments such as the comparison between bulk copper thermal and mechanical fatigue [42] [43] [44]. It is believed that the combination of these three experimental techniques can allow a quantitative guideline of lifetime limits for CLIC and other kinds of normal conducting accelerating structures.

The following tables (7.6, 7.7 and 7.8) show the order of the candidate alloys by ultrasound, laser and RF in terms of fatigue strength, pulsed temperature rise and normalized magnetic field.

Table 7.6: The ranking of the candidate alloys by ultrasound (at $N = 1 \cdot 10^9$)

UNS Name	Cold working ratio [%]	Normalized magnetic field (computed)	Fatigue strength $[MPa]$	ΔT $[°C]$ (computed)
C15000 CuZr	39	1.57	192	137
C15715 GlidCop® Al-15	0	1.52	180	127
C15000 CuZr	80	1.49	185	126
C15100 CuZr	80	1.45	176	120
C15100 CuZr	39	1.45	176	120
C15150 CuZr	39	1.4	157	109
C15150 CuZr	80	1.4	157	109
C18150 CuCrZr	20	1.4	190	128
C10100 Cu-OFE	50	1.2	110	80

Table 7.7: The ranking of the candidate alloys by laser (at $N = 2 \cdot 10^4$)

UNS Name	Thermal state	Normalized magnetic field (computed)	Fatigue strength $[MPa]$ (computed)	ΔT $[°C]$
C15000 CuZr	cw 40 %	2.05	340	240
C15000 CuZr	annealed	1.95	300	213
C15715 GlidCop® Al-15	hot extruded	1.95	290	217
C10100 Cu-OFE	cw 50 %	1.85	260	183

7.7 Comparison of the estimated experimental errors

The experimental errors of the ultrasonic fatigue experimental setup were discussed in Chapters 4.2 and 4.2.1. The amplitude of the AC signal from the oscilloscope could be read by a precision of ± 1 mV, therefore the displacement amplitude measurement was precise within ± 0.2 μm or ± 1-2 %. The error is not an absolute value. The maximum error for the stress level is thus ± 2 %.

Table 7.8: The ranking of the candidate alloys by RF (at $N = 1 \cdot 10^7$)

UNS Name	Thermal state	Normalized magnetic field (computed)	Fatigue strength $[MPa]$ (computed)	ΔT $[°C]$
C15000 CuZr	hot extruded	1.17	100	70
C10100 Cu-OFE	cw 50 %	1.16	100	70
C15000 CuZr	cw 39 %	1.4	159	110

The crack propagation time from zero to 2 mm was of the order of 1 - 5 s ($2.5 \cdot 10^4$ - $12.5 \cdot 10^4$ cycles at 24 kHz). The lifetime range of these experiments was from 10^7 to 10^{11}. The shortest ultrasonic run was about 10^7 cycles (600 s at 24 kHz), and the crack propagation time was less than 1 % of it. Therefore, for the ultrasonic experiments the crack propagation time was negligible and the number of cycles until failure for each specimen was defined with a precision of higher than 1 %.

A larger scatter in the results of ultrasonic experiments was observed between 10^7 and 10^8 cycles. This can be explained by the presence of a transition zone from LCF to HCF where different failure mechanisms compete. Similar observations have been made for example for aluminium [17] and copper [32].

For the laser fatigue experiments, several errors affected the number of cycles and the stress level of the data points. The shot to shot fluctuation of the laser beam intensity is of ± 10 %, resulting in a random error in the induced stress amplitude. In addition, the heated area is defined with ± 10 % accuracy, which causes a systematic error in the stress level.

The accuracy of the number of cycles of the laser data depends on how often one measures the surface roughness during a run. The roughness has to be measured during an intervention, because one cannot measure it continuously. In this study, the accuracy for N is about ± 20 %.

In summary, the ultrasonic fatigue experimental technique is precise to the ± 2 % level and most of the data collected can be used to make conclusions. It is clear that the laser fatigue data needs more statistics and upgrades to increase precision.

The radio frequency experimental results of this study are very recent and there are some uncertainties about the exact stress level, because of issues concerning the commissioning of the apparatus which were refined in the course of the study. The error margins are difficult to estimate at this stage.

8 Conclusions and outlook

The theoretical studies, simulations and experimental results which have been obtained in this study have led to the following conclusions:

Pure copper C10100

The experimental results show that the classical material for normal conducting accelerating cavities and structures, the oxygen-free electronic copper C10100, cannot meet the CLIC parameters set in June 2007 ($\Delta T = 56\ ^{\circ}C$, $N = 2.33 \cdot 10^{10}$). Indeed, the threshold in the 10^{10} range for cold worked C10100 estimated from the ultrasonic fatigue experiments ($\Delta T = 70\ ^{\circ}C$) is above the CLIC parameter value, but the failure of the radio frequency cavities is expected to occur at lower stress amplitudes. The RF experiments at SLAC showed damage on cold worked C10100 at $70\ ^{\circ}C$, $N = 2 \cdot 10^6$.

By taking the RF and laser experimental results at $2 \cdot 10^6$ cycles and using the slope obtained by ultrasonic tests for extrapolation, the limit values of a pulsed temperature rise for the CLIC accelerating structures at $N = 2.33 \cdot 10^{10}$ are $48\ ^{\circ}C$ (stress amplitude = $70\ MPa$) for cold worked C10100 and $34\ ^{\circ}C$ (stress amplitude = $53\ MPa$) for annealed C10100.

Performances of the candidate alloys

The fatigue strength of the candidate alloys is well defined by the ultrasonic experiments. Three of them were studied also by the laser setup and two by the RF setup. The same order and offsets were obtained with all three techniques, although all of the alloys were generally fatigued at lower stress amplitudes by laser and RF than by ultrasound, for the same number of cycles. This can be explained by the different failure criteria, which is met earlier by laser and RF than by ultrasound.

The same experimental fatigue data presented as magnetic field amplitude versus number of cycles - which directly gives us the relative obtainable accelerating gradient for different alloys - basically gives us the same ranking apart for the copper chromium zirconium C18150, which decreases by several steps due to its lower electrical and thermal conductivities.

Both ways of presenting the data (magnetic field versus N and stress amplitude versus N) put forward the same alloy as best candidate. Of all the alloys studied,

aged and cold worked copper zirconium C15000 has the best fatigue performance. The experimentally collected data is shown in Tables 7.6, 7.7 and 7.8.

The limiting values for CLIC accelerating structures at $N = 2.33 \cdot 10^{10}$ for these materials are derived from the experimental data of all three techniques. The damage thresholds are taken from RF and laser data and extrapolated with the slopes obtained by the ultrasonic experiments. The estimate for cold worked C15000 is a ΔT of 77 $°C$ (stress amplitude = 112 MPa), for hot extruded C15000 a ΔT of 58 $°C$ (stress amplitude = 84 MPa) and for hot extruded C15715 a ΔT of 74 $°C$ (stress amplitude = 109 MPa). The number of cycles for these values is the CLIC lifetime of $2.33 \cdot 10^{10}$.

Precipitation hardenable copper alloys

Precipitation hardenable copper zirconium alloys were more closely studied due to their high potential for the CLIC application. It was observed that the fatigue strength increases significantly with the zirconium content up to the solubility limit of 0.15-0.2 % wt. By increasing the zirconium content we notice that the electrical conductivity decreases, due to the added alloying elements with lower conductivity than copper. However, this effect is less significant and the increase in strength is dominant. The conclusion is that the grade having the highest zirconium content (C15000) is the most interesting for the accelerating structures. The effect of the cold working ratio of the CuZr alloys was also studied and a higher ratio of 80 % resulted in no improved fatigue strength at an ultra high cycle fatigue range, compared to a 39 % cold worked state. This suggests that cyclic hardening occurs for the lower cold working ratio. Hot extruded and cold worked C15000s were studied by RF fatigue experiments and both of them resulted in better performances than cold worked C10100. The use of C15000 is thus advantageous compared to C10100 in both material states, which represent two extremities in terms of strength and conductivities. Lower zirconium content grades could be interesting for lower gradient options of CLIC and a few % gain in overall efficiency compared to C15000 of the CLIC machine could be achieved thanks to higher electrical conductivities.

Surface roughening at ultra high cycle regime

During cyclic loading, some surface modifications before crack nucleation were observed on ultrasonic fatigue specimens at ultra high cycle fatigue regimes, generally above 10^8. It was shown for cold worked C18150 that a 10 % lower stress amplitude than the fatigue strength threshold value led to no surface modifications at the same number of cycles, suggesting thus a threshold for the surface roughness development. It was also shown that surface properties resulting from different fabrication techniques have a strong influence on the appearance of the phenomena.

Specimens fabricated by two different techniques, having otherwise identical parameters, resulted in the same final fracture fatigue strength. However, whereas one had surface modifications, the other did not. The bulk fatigue behavior seems to be independent of the appearance of roughening and the appeared surface roughness is not always and not the only origin of the fatigue crack.

Current experimental evidence does not show that the small micro-cracks or appeared surface roughness do cause a malfunction of the accelerating cavities. If the micro cracks became dormant before the cavity operation was disturbed, it would revolutionize the material possibilities and even annealed pure copper could be used at high gradients.

Crack growth

The ultrasonic experiments revealed different crack growth behaviors of the candidate alloys. Pure copper and all the precipitation hardenable alloys had similar crack growth. The dispersion hardened grade C15715 behaved differently, having a much faster crack growth. The crack growth is not yet known to be a critical parameter for accelerating cavities operating up to UHCF regime, but if the formation of small fatigue micro-cracks could be accepted, the influence of it should be studied in detail.

Damage anisotropy

The RF fatigue experiments on pure copper showed anisotropies in the fatigue damage between adjacent grains inside the maximum stress region. Sometimes, a grain showed no visible damage while its neighbour was heavily affected. This anisotropy is most likely due to different grain orientations having different fatigue resistances and different thermal stress responses. Crack formation seemed to prefer grain boundaries between grains having a highest differences between the levels of fatigue damage.

The effects of the manufacturing process

Selecting a material from the candidate alloys proposed in this study is also dependent on the whole manufacturing process of the accelerating structures, including the preparations before the startup of the machine. The machinability, joinability and, especially, how the strength properties sustain elevated temperatures are key parameters which will define which final material will be selected. Precipitation hardenable C15000 is favoured for its machinability and the dispersion strengthened C15715 is favoured for its elevated temperatures resistance. C15000 is a bit easier

to join to other metals, but some techniques expose it to elevated temperatures and would make it less advantageous. On the other hand, the strength properties of C15715 vary less due to thermal treatments.

RF breakdown resistance of candidate alloys

The RF and DC breakdown resistance of the candidate alloys are under active investigations. The results obtained with various experiments done in different contexts are somewhat contradictory. CERN DC spark experiments [74] suggest no significant difference between pure copper, CuZr and GlidCop®, while the SLAC RF experiments [75] suggest GlidCop® to be much worse than pure copper or even totally unacceptable. The use of GlidCop® might nevertheless be limited by the RF characteristics.

Failure criteria of the accelerating cavities

It was not possible to define the fatigue failure criteria of the CLIC RF structures in this study. The clearly visible damage occurring in the radio frequency fatigue experiments, astonishingly, did not affect the performance of the cavity (drop in quality factor), suggesting that the cracks obtained were not big enough to disturb the flow of the eddy currents. Based on a theory of surface qualities [48] small crack could act as a short circuit and not increase the surface electric resistance.

Future experiments should be pushed further in order to find the threshold and to see if there are any other consequences of the cracks such as increased breakdown probability. The SEM observations have raised various questions. First of all, on whether the extrusions of the fatigue damage would enhance the radio frequency breakdown probability up to unacceptable levels and secondly, on whether that would occur earlier than the disturbance of the surface currents by the microscale fatigue cracks (drop in quality factor). A possible scenario also is that the cracks arrest and become dormant before the performance of the RF cavity is affected.

Combination of the results by the three techniques

A quantitative relationship between the experimental fatigue results obtained by the three different techniques presented in this manuscript has been found. The three methods give the same ranking of the materials and similar relative performance between the materials. The overall goal was to predict the lifetime of the CLIC accelerating structures by making ultrasonic, laser and radio frequency fatigue experiments, each of them representing one subset of the CLIC's case. In this manuscript, the data collected by all three methods has been put together for the

first time and results show that the fatigue phenomenon is similar for the different methods. This observation is encouraging and shows that the study is going in the right direction. Finally, it could ultimately lead to a more precise prediction.

Data Scatter

The results carried out by the ultrasonic setup relatively show little scatter. However, this is for a fracture criterion and the RF failure threshold related data could have a different scatter. The data obtained by laser has a higher scatter, which might indicate that the early stages of fatigue have a higher spread.

Ultrasound experimental data at 10^6 - 10^7 cycles show larger scatter than at higher cycles, indicating a possible competition between the LCF and HCF fatigue mechanisms.

Compressive mean stress

The ultrasonic experiments had, in the default configuration, a reversed stress condition (tension - compression). Experiments with pre-stressed specimens having a fully compressive stress condition did not result in any differences in the fatigue strength amplitudes obtained. This indicates a higher usability of the ultrasonic fatigue data in estimating the lifetime limits of the CLIC accelerating structures, where the cyclic stress is fully compressive.

Crack path deflection

The ultrasonic experiments on CuZr alloys showed a change in the crack path morphology when the number of cycles increased. Below 10^8 cycles the crack followed a straight path but above 10^8 cycles it was strongly deflected to have a crystallographic path. This indicates that the crack mode changes from transgranular to intergranular.

Suggestions for future work

The fatigue study at CERN will continue, mainly with the same experimental setups, but focusing in the areas which are thought to be the most relevant for normal conducting accelerating cavities. Here are some suggestions listed by the author:

To confirm the theory which poses that the failure threshold of the RF cavities caused by thermal fatigue occurs earlier than the fracturing caused by mechanical

fatigue, more fatigue experiments by radio frequency and ultrasonic fatigue setups are required.

The demonstrated RF experiments should be pushed further than the first visible damage, as it was observed that this was not yet affecting the functionality of the RF cavity. This is important work for establishing the damage criteria of the CLIC structures.

The RF induced thermal fatigue crack propagation should be studied in order to understand if the cracks would arrest and become dormant after penetrating in to the zero-stress zone. This would also require studies of how RF induced surface currents flow in existence of surface roughness and micro-cracks.

The grain orientations in the fatigued zones should be measured for instance by EBSD technique (Electron Backscatter Diffraction) in order to study the fatigue resistance of copper alloys as a function of grain orientation.

The scope of ultrasonic experiments should be refocused so that more attention is paid to the surface modifications during the cyclic loading before the actual fracture. The ultrasound is still the only method that can reasonably reach the UHCF regime and from this respect it therefore remains an important tool for the study.

The laser setup is also an important tool to make the connection between RF and ultrasound. It allows higher throughput than the RF setup and has conditions closer to the real case than the ultrasonic setup. It has the right pulse length, which means that it could clearly produce lots of interesting data to make a stronger connection between the ultrasonic mechanical fatigue and the radio frequency induced thermal fatigue data. The laser fatigue data is quite scattered due to fluctuations during the experimental run. Some upgrades of the system and more statistics would be required to improve the accuracy.

As the mechanical fatigue data obtained by ultrasound cannot have less than 10^6 - 10^7 cycles and the RF and laser cannot reasonably make more than 10^7 cycles, mechanical fatigue experiments with low frequency tensile test machine are proposed in order to extend the ultrasonic data towards the low cycle end and thus increase the overlap of the data.

The machinability of the dispersion strengthened alloy C15715 should be studied as it is an important issue for the material selection due to the high accuracy and mass production considerations.

Radio frequency breakdown resistance of the candidate alloys should be cross checked due to the possibly inconsistent results between CERN DC spark and SLAC RF experiments.

The resistance against elevated temperatures of C15000 should be studied, especially how it would sustain the typical bake out treatments of the ultra high vacuum components.

The radio frequency fatigue experimental setup had no electric field at areas of the fatigue damage. Therefore, it does not show whether the breakdown resistance is affected by the surface fatigue damage. A similar setup, but with high electric field at fatigued areas, would give important and crucial experimental data for the final conclusion of the fatigue study.

Closer to the moment when final design decisions must be made and when the selection of the candidate alloy(s) is more mature, a statistical study should be carried out in order to define the required safety margin.

References

[1] J. Ellis, I. Wilson, New physics with the compact linear collider, 11 pages, CLIC Note 466, CERN (2000).

[2] ILC GDE (Global Design Effort), The web pages of the international linear collider ILC, June 2010.
URL http://www.linearcollider.org/cms/

[3] W. Schnell, A two-stage RF linear collider using a superconducting drive linac, 13 pages, CLIC Note 13, CERN (1986).

[4] CLIC study team, CLIC notes at CERN document server (June 2010).
URL http://cdsweb.cern.ch/collection/CLIC%20Notes

[5] CLIC study team, the web pages of the compact linear collider CLIC study (June 2010).
URL http://clic-study.web.cern.ch/CLIC-Study/

[6] A. Grudiev, W. Wünsch, A newly designed and optimized CLIC main linac accelerating structure, 4 pages, CLIC Note 601, CERN (2004).

[7] A. Grudiev, D. Schulte, W. Wünsch, Optimum frequency and gradient for the CLIC main linac accelerating structure, 4 pages, CLIC Note 677, CERN (2006).

[8] J. Delahaye, CLIC parameters update, Minutes of CLIC meeting (January 2007).
URL http://clic-meeting.web.cern.ch/clic-meeting/2007/

[9] W. Wünsch, Progress in understanding the high-gradient limitations of accelerating structures, 6 pages, CLIC Note 706, CERN (2007).

[10] S. Heikkinen, S. Calatroni, G. Arnau-Izquierdo, W. Wünsch, N. Neupert, High power RF induced thermal fatigue in the high gradient CLIC accelerating structures, 13 pages, Fatigue 2007 conference, cambridge, uk, Engineering Integrity Society (2007).

[11] A. Descoeudres, DC spark results, proceedings of the CLIC workshop, October 2007.
URL http://project-clic07-workshop.web.cern.ch/project-CLIC07-workshop/

[12] A. Wöhler, Über die festigkeitsversuche mit eisen and stahl, Zeitschrift für Bauwesen, vol. 20, pages 73-106 (1870).

[13] A. Vinogradov, V. Patlan, Y. Suzuki, K. Kitagawa, V. Kopylov, Structure and properties fo ultra-fine grain CuCrZr alloy produced by equal-channel angular pressing, Acta materialia, vol. 50, number 7, pp. 1639-1651, Elsevier Ltd (2002).

[14] H. Mughrabi, On life-controlling microstructural fatigue mechanisms in ductile metals and alloys in gigacycle regime, Fatigue and fracture of engineering materials and structures, vol. 22, number 7, pp. 633-641, Wiley (1999).

[15] H. Mughrabi, Specific features and mechanisms of fatigue in the ultra high cycle regime, International journal of fatigue, vol. 28, issue 11, pp. 1501-1508, Elsevier Ltd (2006).

[16] Z. Yang, S. Li, J. Zhang, J. Zhang, Z. Li, G. Li, The fatigue behaviors of zero-inclusion and commercial 42CrMo steels in the super-long fatigue fatigue life regime, Acta materialia, vol. 52, number 18, pp. 5235-5241, Elsevier Ltd (2004).

[17] I. Marines, X. Bin, C. Bathias, An understanding of very high cycle of metals, International journal of fatigue, vol. 25, number 9-11, pp. 1101-1107, Elsevier Ltd (2003).

[18] S. Fabritsiev, A. Pokrovsky, Effect of neutron irradiation on low-cycle fatigue of GlidCop AL-25-IG alloy for ITER applications, Fusion engineering and design, vol. 65, issue 1, pp. 47-56, Elsevier Ltd (2003).

[19] S. Tähtinen, B. Singh, Final report on characterization of physical and mechanical properties of copper and copper alloys before and after irradiation (ITER R&D task number T213), 22 pages, Risø R (EN), number 1276, Risø National Laboratory, Roskilde (2001).

[20] J. Strizak, J. DiStefano, Fatigue properties of type 316LN stainless steel as a function of frequency and waveform, ORNL TM-2000, number 270, Oak Ridge National Laboratory (2000).

[21] S. Kwofie, Cyclic creep of copper due to axial cyclic and tensile mean stresses, Materials science and engineering A, vol. 427, pp. 263-267, Elsevier Ltd (2006).

[22] H.-J. Christ, G. Hoffmann, O. Öttinger, History effects in metals during constant and variable amplitude testing I: Wavy dislocation glide behaviour, Materials science and engineering, vol. 201, number 1-2, pp. 1-12, Elsevier Ltd (1995).

[23] T. Goswami, H. Hänninen, Dwell effects on high temperature fatigue behavior part I, Materials and design, vol. 22, issue 3, pp. 199-215, Elsevier Ltd (2001).

[24] T. Goswami, H. Hänninen, Dwell effects on high temperature fatigue damage mechanisms part II, Materials and design, vol. 22, issue 3, pp. 217-236, Elsevier Ltd (2001).

[25] J. Stubbins, M. Li, B. Singh, Room temperature creep-fatigue response of selected copper for high heat flux applications, Journal of nuclear materials, volumes 329-333, part 1, pp. 865-869, Elsevier Ltd (2004).

[26] S. Suresh, Fatigue of materials, second ed., Cambridge Univ. Press, 679 pages, 1998.

[27] V. F. Terentšev, On the problem of the fatigue limit of metallic materials, Metallovedenie i termicheskaya obrabotka metallov, vol. 46, number 5-6, pp. 244-249, Springer Science and Business Media, Inc. (2004).

[28] S. Stanzl-Tschegg, H. Mughrabi, B. Schönbauer, Life time and cyclic slip of copper in the VHCF regime, International journal of fatigue, vol. 29, number 9-11, pp. 2050-2059, Elsevier Ltd (2007).

[29] H. Mughrabi, B. Schönbauer, F. Pyczak, D. Amberger, A. Weidner, S. Stanzl-Tschegg, Fatigue damage in copper polycrystals subjected to ultrahigh-cycle fatigue below PSB threshold, International journal of fatigue, vol. 32, number 6, pp. 872-878, Elsevier Ltd (2010).

[30] S. Stanzl-Tschegg, B. Schönbauer, Mechanisms of strain localization, crack initiation and fracture of polycrystalline copper in VHCF regime, International journal of fatigue, vol. 32, number 6, pp. 886-893, Elsevier Ltd (2009).

[31] L. Kunz, P. Lukas, M. Svoboda, Fatigue strength, microstructural stability and strain localization in ultra fine grained copper, Materials science and engineering a, vol. 424, number 1-2, pp. 97-104, Elsevier Ltd (2006).

[32] G. Khatibi, J. Horky, B. Weiss, M. Zehetbauer, High cycle fatigue behavior of copper deformed by high pressure torsion, International journal of fatigue, vol. 32, issue 2, pp. 269-278, Elsevier Ltd (2009).

[33] M. Goto, S. Han, T. Yakushiji, C. Lim, S. Kim, Formation process of shear bands and protrusions in ultra fine grained copper under cyclic stresses, Scripta materialia, vol. 54, number 12, pp. 2101-2106, Elsevier Ltd (2006).

[34] L. Cretegny, A. Saxena, AFM characterization of the evolution of surface deformation using fatigue in polycrystalline copper, Acta materialia, vol. 49, number 18, pp. 3755-3765, Pergamon (2001).

[35] M. Merola, Normative issues in thermal fatigue design of nuclear components, Nuclear engineering and design, vol. 158, number 2-3, pp. 351-361, Elsevier Ltd (1995).

[36] C. Gourdin, S. Marie, S. Chapuliot, An analytical thermal fatigue crack growth approach, 20th International conference on structural mechanics in reactor technology, SMiRT 20-Division 2, paper 1796, Espoo, Finland, August (2009).

[37] P. Panda, T. Kannan, J. Dubois, C. Olagon, G. Fantozzi, Thermal shock and thermal fatigue study of ceramic on a newly developed thermal shock test equipment, Science and technology of advanced materials, vol. 3, pp. 327-334, Elsevier Ltd (2002).

[38] J. Bystriansky, J. Siegl, P. Hausid, B. Strnadel, Thermal fatigue of stainless steels, Acta Metallurgica Slovaca, number 3, pp. 311-322, AAA DOMY, s.r.o., Kosice (2005).

[39] R. J. Roark, W. C. Young, Formulas for stress and strain, 640 pages, McGraw-Hill, New York, 1975.

[40] A. Weronski, T. Hejwowski, Thermal Fatigue of Metals, 366 pages, Marcel Dekker, Inc. New York, 1991.

[41] G. R. Halford, Thermal Stresses II Vol. 2, Chapter 6: Low-Cycle Thermal Fatigue, pp. 329-428, Elsevier Science Publishers B.V., 1987.

[42] R. Mönig, Y.-B. Park, C. A. Volkert, Thermal fatigue in copper interconnects, 8^{th} International workshop on stress-induced phenomena in metallization, AIP conference proceedings, vol. 817, pp. 147-156, American Institute of Physics (2006).

[43] P. Lukas, L. Kunz, Effect of grain size on the high cycle fatigue behaviour of polycrystalline copper, Materials science and engineering a, vol. 85, pp. 67-75, Elsevier Ltd (1987).

[44] O. Kraft, P. Wellner, M. Hommel, R. Schwaiger, E. Artz, Fatigue behavior of polycrystalline thin copper films, Metallkd., vol. 93, number 5, pp. 392-400 (2002).

[45] D. P. Pritzkau, RF pulsed heating, Ph.d. thesis, 290 pages, Stanford Linear Accelerator Center, Stanford, CA (2001).

[46] D. L. Ellis, GRCop-84: A high-temperature copper alloy for high-heat-flux applications, 30 pages, NASA TM 2005-213566, Glenn Research Center, Cleveland, Ohio (2005).

[47] J. D. Jackson, Classical electrodynamics, 848 pages, Wiley, New York, 1975.

[48] S. J. Morgan, Effect of surface roughness on eddy current losses at microwave frequencies, Journal of applied physics, vol. 20, issue 4, pp. 352-362, Bell Telephone Laboratories, NJ (1949).

[49] I. Wilson, Surface heating of the CLIC main linac structure, CLIC Note 52, 9 pages, CERN (1987).

[50] CLIC study team, The CLIC parameters list, December 2007.
URL `http://clic-meeting.web.cern.ch/clic-meeting/clictable2007.html`

[51] R. Nousiainen, Main requirement for module cooling, CLIC Workshop proceedings, October 2007.
URL http://project-clic07-workshop.web.cern.ch/project-CLIC07-workshop/

[52] H. H. Braun, R. Corsini, A. de Roeck, A. Grudiev, S. T. Heikkinen, E. Jensen, M. S. Korostelev, D. Schulte, I. V. Syratchev, F. A. Tecker, W. Wünsch, F. Zimmermann, Updated CLIC parameters 2005, 36 pages, CLIC Note 627, CERN (2006).

[53] W. P. Mason, Piezoelectric Crystals and their Applications in Ultrasonics, 508 pages, D. Van Nostrand and Company, New York, 1950.

[54] W. Wünsch, Private communications (2007).

[55] M. A. Meyers, K. K. Chawla, Mechanical behaviour of materials, 680 pages, Englewood Cliffs, NJ, 1999.

[56] S. Kocanda, Fatigue failure of metals, 367 pages, Alphen-aan-den-Rijn, Sijthoff and Noordhoff, 1978.

[57] American Society for Testing and Materials, Standard specification for titanium and titanium alloy bars and billets, ASTM B348-06a, Standard, ASTM International (2006).

[58] S. Calatroni, H. Neupert, M. Taborelli, Fatigue testing of materials by UV pulsed laser irradiation, 5 pages, CLIC Note 615, CERN (2004).

[59] G. Bentini, M. Bianconi, C. Summonte, Surface doping of semiconductors by pulsed-laser irradiation in reactive atmosphere, Applied physics A, vol. 45, number 4, pp. 317-324,, CNR - Istituto LAMEL (1988).

[60] S. Tantawi, Materials testing with a high-Q RF cavity, Proceedings of the high gradient workshop, September 2006.
URL http://hg2006.web.cern.ch/HG2006/

[61] American Society for Testing and Materials, Standard specification for hot-rolled and cold-finished age-hardening stainless steel bars and shapes, ASTM A564/A564M-04, Standard, ASTM International (2004).

[62] D. Coyne, LIGO vacuum compatible materials list, Internal working note of the LIGO project, LIGO-E960050-B-E, 15 pages, LIGO Laboratory (2004).

[63] G. Li, B. Thomas, J. Stubbins, Modeling creep and fatigue of copper alloys, Metallurgical and materials transactions A, vol. 31, number 10, pp. 2491-2502 (2000).

[64] American Society for Testing and Materials, Standard test method for determining electrical conductivity using the electromagnetic (eddy-current) method, ASTM E1004-9, Standard, ASTM International (2009).

[65] American Society for Testing and Materials, Standard test method for tension testing of metallic materials, ASTM E8 8M-09, Standard, ASTM International (2009).

[66] American Society for Testing and Materials, Standard test method for Vicker's hardness test method of metallic materials, ASTM E92(2003)e2, Standard, ASTM International (2003).

[67] American Society of Mechanical Engineers, Surface texture, surface roughness, waviness and lay, ASME B46.1 - 2002, Standard, ASME (2002).

[68] D. G. Brandon, W. D. Kaplan, Microstructural characterization of materials, 409 pages, Wiley, New York, NY, 1999.

[69] V. K. Sarin, N. J. Grant, Cu-Zr and Cu-Zr-Cr alloys produced from rapidly quenched powders, Metallurgical and materials transactions b, vol. 3, number 4, 875-878, Springer Boston (1971).

[70] N. J. Simon, E. S. Drexler, R. P. Reed, Properties of copper and copper alloys at cryogenic temperatures, 855 pages, NIST Monograph, number 177, National Institute of Standards and Technology (1992).

[71] Deutsches Kupfersinstitut, CuCr1Zr, Technical data sheet.
URL `http://www.kupfer-institut.de/front_frame/pdf/CuCr1Zr.pdf`

[72] E. L. Garwin, M. Rabinowitz, Thin dielectric films in superconducting cavities, Lettere al nuovo cimento (1971), vol. 2, number 9, pp. 450-452.

[73] S. Calatroni, T. Ramsvik, A. Reginelli, M. Taborelli, Investigations of DC breakdown fields, 4 pages, CLIC Note 703, CERN (2007).

[74] G. Arnau-Izquierdo, S. Calatroni, S. Heikkinen, T. Ramsvik, S. Sgobba, M. Taborelli, W. Wünsch, Material selection and characterization for high gradient RF applications, 4 pages, CLIC Note 725, CERN (2007).

[75] L. Laurent, High gradient RF breakdown studies, 204 pages, PhD thesis, University of California (2002).

[76] A. B. Chin, T. Bao, S. Chen, Braze joints of dispersion strengthened copper, Journal of nuclear materials, vol. 233, pp. 902-905, Elsevier (1996).

[77] W. Wünsch, Progress in understanding the high-gradient limitations of accelerating structures, 6 pages, CLIC Note 706, CERN (2007).

[78] M. Kikukawa, K. Ohji, K. Ogura, Y. Kajio, Relationship between frequency and temperature effects on fatigue, 10 pages, JSMA 1967 semi-international symposium, Osaka University (1967).

[79] L. Roth, L. Willertz, On the fatigue of copper up to ultrasonic frequencies, 17 pages, Ultrasonic fatigue conference, AIME (1982).

HELSINKI UNIVERSITY OF TECHNOLOGY DOCTORAL THESES IN MATERIALS AND EARTH SCIENCES

TKK-ME-DT-1 Ranki-Kilpinen, T.,
Sulphation of Cuprous and Cupric Oxide Dusts and Heterogeneous Copper Matte Particles in Simulated Flash Smelting Heat Recovery Boiler Conditions. 2004

TKK-ME-DT-2 Söderberg, O.,
Novel Ni-Mn-Ga Alloys and their Magnetic Shape Memory Behaviour. 2004

TKK-ME-DT-3 Kaskiala, T.,
Studies on Gas-Liquid Mass Transfer in Atmosperic Leaching of Sulphidic Zinc Concentrates. 2005

TKK-ME-DT-4 Grau, R.A.,
An Investigation of the Effect of Physical and Chemical Variables on Bubble Generation and Coalescence in Laboratory Scale Flotation Cells. 2006

TKK-ME-DT-5 Kivikytö-Reponen, P.,
Correlation of Material Characteristics and Wear of Powder Metallurgical Metal Matrix Composites. 2006

TKK-ME-DIS-6 Ge, Y.,
The Crystal and Magnetic Microstructure of NI-Mn-Ga Alloys. 2007

TKK-ME-DIS-7 Kankaanpää, T.,
CFD Procedure for Studying Dispersion Flows and Design Optimization of the Solvent Extraction Settler. 2007

TKK-ME-DIS-8 Miettinen, E.,
Thermal Conductivity and Characteristics of Copper Flash Smelting Flue Dust Accretions. 2008

TKK-ME-DIS-9 Lundström, M.,
Chalcopyrite Dissolution in Cupric Chloride Solutions. 2009

ISBN 978-952-60-3345-7
ISBN 978-952-60-3346-4 (electronic)
ISSN 1795-0074